Field Performance of Fiber-Reinforced Concrete Overlays

Final Report
April 2025

National Concrete Pavement Technology Center

Tech Center

IOWA STATE UNIVERSITY
Institute for Transportation

Sponsored by
Iowa Highway Research Board
(IHRB Project TR-816)
Iowa Department of Transportation
(InTrans Project 22-829)

IHRB celebrating 75 years

About the CP Tech Center

The mission of the National Concrete Pavement Technology Center (CP Tech Center) at Iowa State University is to unite key transportation stakeholders around the central goal of developing and implementing innovative technology and best practices for sustainable concrete pavement construction and maintenance.

About the Institute for Transportation

The mission of the Institute for Transportation (InTrans) at Iowa State University is to save lives and improve economic vitality through discovery, research innovation, outreach, and the implementation of bold ideas.

Iowa State University Nondiscrimination Statement

Iowa State University does not discriminate on the basis of race, color, age, ethnicity, religion, national origin, pregnancy, sexual orientation, gender identity, genetic information, sex, marital status, disability, or status as a U.S. Veteran. Inquiries regarding non-discrimination policies may be directed to Office of Equal Opportunity, 2680 Beardshear Hall, 515 Morrill Road, Ames, Iowa 50011, telephone: 515-294-7612, email: eooffice@iastate.edu.

Disclaimer Notice

The contents of this report reflect the views of the authors, who are responsible for the facts and the accuracy of the information presented herein. The opinions, findings and conclusions expressed in this publication are those of the authors and not necessarily those of the sponsors.

The sponsors assume no liability for the contents or use of the information contained in this document. This report does not constitute a standard, specification, or regulation.

The sponsors do not endorse products or manufacturers. Trademarks or manufacturers' names appear in this report only because they are considered essential to the objective of the document.

Iowa DOT Statements

Iowa DOT ensures non-discrimination in all programs and activities in accordance with Title VI of the Civil Rights Act of 1964. Any person who believes that they are being denied participation in a project, being denied benefits of a program, or otherwise being discriminated against because of race, color, national origin, gender, age, or disability, low income and limited English proficiency, or if needs more information or special assistance for persons with disabilities or limited English proficiency, please contact Iowa DOT Civil Rights at 515-239-7970 or by email at civil.rights@iowadot.us.

The preparation of this report was financed in part through funds provided by the Iowa Department of Transportation through its "Second Revised Agreement for the Management of Research Conducted by Iowa State University for the Iowa Department of Transportation" and its amendments.

The opinions, findings, and conclusions expressed in this publication are those of the authors and not necessarily those of the Iowa Department of Transportation.

Front Cover Image Credits

Left: CP Tech Center; Right: ACPA, used with permission

Technical Report Documentation Page

1. Report No.	2. Government Accession No.	3. Recipient's Catalog No.
IHRB Project TR-816		

4. Title and Subtitle	5. Report Date
Field Performance of Fiber-Reinforced Concrete Overlays	April 2025
	6. Performing Organization Code

7. Author(s)	8. Performing Organization Report No.
Dan King (orcid.org/0000-0001-8824-1818), Bo Yang (orcid.org/0000-0002-7774-5233), Peter Taylor (orcid.org/0000-0002-4030-1727), and Halil Ceylan (orcid.org/0000-0003-1133-0366)	InTrans Project 22-829

9. Performing Organization Name and Address	10. Work Unit No. (TRAIS)
Institute for Transportation Iowa State University 2711 South Loop Drive, Suite 4700 Ames, IA 50010-8664	11. Contract or Grant No.

12. Sponsoring Organization Name and Address	13. Type of Report and Period Covered
Iowa Highway Research Board Iowa Department of Transportation 800 Lincoln Way Ames, IA 50010	Final Report
	14. Sponsoring Agency Code

15. Supplementary Notes

Visit https://cptechcenter.org for color pdfs of this and other research reports.

16. Abstract

An increasing number of concrete overlay projects in Iowa and around the United States have used fiber-reinforced concrete (FRC) mixtures. Fibers provide residual strength to concrete mixtures, and concrete overlay design procedures currently assume that fiber reinforcement enhances fatigue life. A number of studies have suggested that fibers may offer a number of additional performance benefits to concrete overlays. This study conducted a field investigation of six different concrete overlay sites in Iowa. Three of these sites contained test sections with varying thickness and joint spacing designs, and with and without fiber reinforcement. The field investigation performed a variety of tests to measure properties such as joint activation behavior, load transfer, structural response, pavement smoothness, and curling and warping behavior. This test regime allowed for a broad characterization of many aspects of the behavior and performance of concrete overlays, both with and without fiber reinforcement. The results indicated that, to date, fiber reinforcement did not appear to have a significant impact on load transfer, smoothness, or curling and warping at these concrete overlay sties. However, the comprehensive testing regime provided a number of insights into other aspects of concrete overlay design and performance, both with and without fiber reinforcement. The bond between concrete and asphalt was particularly important, even when the overlays were not intentionally designed to bond to the underlying asphalt layer. Finally, this report also contains an appendix detailing a separate investigation of the behavior of FRC pavements placed without transverse joints.

17. Key Words	18. Distribution Statement
concrete overlay—fiber-reinforced concrete—FRC overlays—transverse joints	No restrictions.

19. Security Classification (of this report)	20. Security Classification (of this page)	21. No. of Pages	22. Price
Unclassified.	Unclassified.	159	NA

Form DOT F 1700.7 (8-72) **Reproduction of completed page authorized**

FIELD PERFORMANCE OF FIBER-REINFORCED CONCRETE OVERLAYS

Final Report
April 2025

Principal Investigator
Peter Taylor, Director
National Concrete Pavement Technology Center, Iowa State University

Co-Principal Investigators
Dan King, Research Engineer
National Concrete Pavement Technology Center, Iowa State University

Halil Ceylan, Director
Program for Sustainable Pavement Engineering and Research
Institute for Transportation, Iowa State University

Authors
Dan King, Bo Yang, Peter Taylor, and Halil Ceylan

Sponsored by
Iowa Highway Research Board and
Iowa Department of Transportation
(IHRB Project TR-816)

Preparation of this report was financed in part
through funds provided by the Iowa Department of Transportation
through its Research Management Agreement with the
Institute for Transportation
(InTrans Project 22-829)

A report from
National Concrete Pavement Technology Center
Iowa State University
2711 South Loop Drive, Suite 4700
Ames, IA 50010-8664
Phone: 515-294-8103 / Fax: 515-294-0467
https://cptechcenter.org

TABLE OF CONTENTS

LIST OF FIGURES

LIST OF TABLES

ACKNOWLEDGMENTS

The research team would like to thank the Iowa Department of Transportation (DOT) and Iowa Highway Research Board (IHRB) for sponsoring this research.

The research team also thanks Rich Brumm with Mitchell and Worth Counties, Brian Keierleber with Buchanan County, and Todd Hanson with the Iowa DOT for collaborating to design the test sections. Additional thanks are due to Cedar Valley Corp.; Croell, Inc.; Flynn Co., Inc.; Horsfield Construction, Inc.; and the Iowa Concrete Paving Association for supporting the test program and constructing the test sections and to Forta Corporation and Heidelberg Cement for donating materials. The research team also thanks Chris Brakke and Brent Terry with the Iowa DOT for their assistance with data collection.

EXECUTIVE SUMMARY

An increasing number of concrete overlay projects in Iowa and around the United States have used fiber-reinforced concrete (FRC) mixtures. Fibers provide residual strength to concrete mixtures, and concrete overlay design procedures currently assume that fiber reinforcement enhances fatigue life. A number of studies have suggested that fibers may offer a number of additional performance benefits to concrete overlays. This study conducted a field investigation of six different concrete overlay sites in Iowa. Three of these sites contained test sections with varying thickness and joint spacing designs, and with and without fiber reinforcement. The field investigation performed a variety of tests to measure properties such as joint activation behavior, load transfer, structural response, pavement smoothness, and curling and warping behavior. This test regime allowed for a broad characterization of many aspects of the behavior and performance of concrete overlays, both with and without fiber reinforcement. The results indicated that, to date, fiber reinforcement did not appear to have a significant impact on load transfer, smoothness, or curling and warping at these concrete overlay sties. However, the comprehensive testing regime provided a number of insights into other aspects of concrete overlay design and performance, both with and without fiber reinforcement. The bond between concrete and asphalt was particularly important, even when the overlays were not intentionally designed to bond to the underlying asphalt layer. Finally, this report also contains an appendix detailing a separate investigation of the behavior of FRC pavements placed without transverse joints.

1. INTRODUCTION

1.1 Fiber-Reinforced Concrete

Fiber-reinforced concrete (FRC) consists of a concrete mixture reinforced with discrete, distributed fibers that are added to fresh concrete during mixing. After placement and setting, the fibers are embedded throughout the entirety of the concrete mass. Fibers come in a variety of shapes, sizes, and textures and can be made from a variety of materials. Fibers are classified either as microfibers or macrofibers based on their equivalent diameter (ACI 2008).

Macrofibers are the primary type of fiber used in concrete overlays and other concrete pavement applications. These fibers are usually 1 to 2 in. in length, 0.02 to 0.04 in. in diameter, and dosed at rates of 0.2% to 1.0% by volume or greater, depending on the application (Roesler et al. 2019). While macrofibers can be made from materials such as steel, glass, and carbon (ACI 2008), synthetic macrofibers made from polypropylene or polyethylene have become established as the predominant type of fiber used in concrete overlays.

Macrofibers begin to engage when cracks form within the concrete matrix. Fibers present in these areas work to bridge the developing cracks, carrying tensile stresses and absorbing energy to slow crack propagation (ACI 2018). While they can only resist the opening of cracks to a point, the action of the fibers allows FRC to carry additional stresses and absorb a greater amount of energy until failure relative to plain concrete. This improvement in post-crack load-carrying capacity contributes primarily to bending/flexure and is known as residual strength (ACI 2018).

Macrofibers have also been shown to enhance the fracture properties of concrete (Kim and Bordelon 2017a). Figure 1 shows the ability of fibers to assist in resisting the opening of a crack during the three-point loading of an FRC single-edge notched beam. Fibers also reduce the widths of early-age cracks, including shrinkage cracks (Shah and Weiss 2006) and cracks that develop beneath sawcut contraction joints (Kim and Bordelon 2017b). In floor slab applications, FRC is also sometimes used to extend joint spacing beyond typical design limits (ACI 2018).

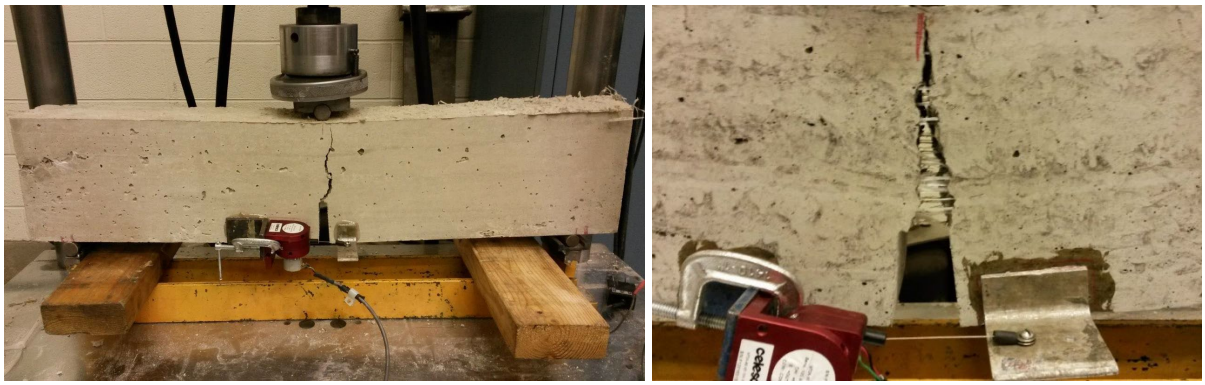

Figure 1. Microfibers resisting crack opening in a single-edge notched beam

1.2. FRC Overlay Design and Behavior

There has been significant growth in the past 25 years in the use of FRC for pavement applications, particularly for thin concrete overlays. Since gaining traction in the 1990s, approximately 100 FRC overlay projects have been built in the United States (Roesler et al. 2019). Iowa is home to more concrete overlay projects than any other US state (Gross et al. 2017), and approximately 12 FRC overlay projects have been constructed in Iowa since 2017 on city, county, and state roadways.

The primary goals of incorporating fibers into concrete overlays are to enhance the fatigue performance of the pavement through added residual strength and to improve long-term durability and performance by keeping cracks and joints tight. These design goals are illustrated in Figure 2.

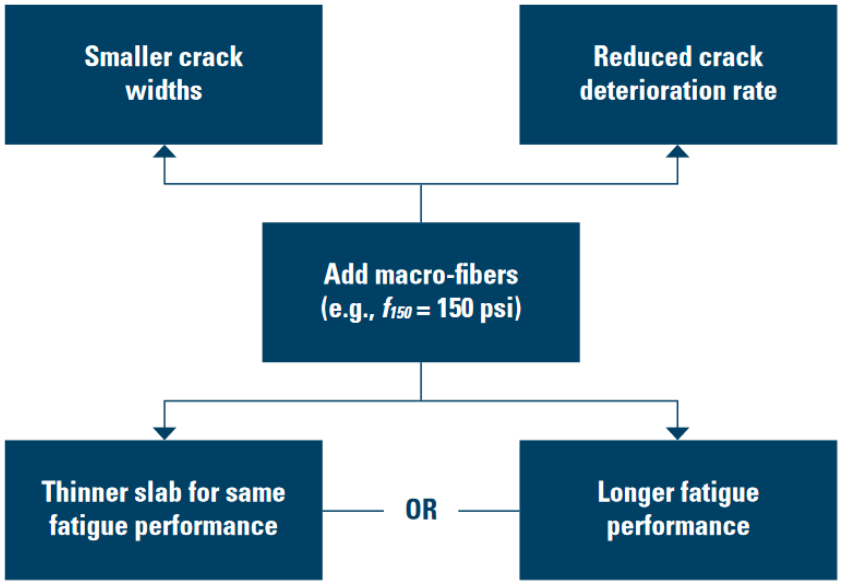

Roesler et al. 2019

Figure 2. Design benefits of using FRC

Many modern design procedures for concrete overlays allow the designer to specify FRC (Ferrebee et al. 2018, Li et al. 2019). These procedures usually account for the benefits of fibers by adding the residual strength to the normal design flexural strength of concrete to produce an effective design flexural strength value (Roesler et al. 2019). (Designers can also use this process to account for the residual strength benefits of fibers, even when a design procedure does not allow the user to directly specify FRC.) Flexural fatigue performance is a critical factor in concrete pavement design, so adding fibers to increase the effective flexural strength of the concrete allows the designer to either extend the design life of an overlay at a given thickness or reduce the overlay design thickness while achieving an equivalent design life.

1.3. Additional Potential Performance Benefits of FRC Overlays

While the impact of residual strength is well understood and accounted for in design, many of the other potential performance benefits of using fibers in concrete overlays are not as well quantified. When durability- or materials-related distresses develop in concrete pavements, they usually occur at joints and cracks (Weiss et al. 2016). The ability of fibers to hold cracks tight, including cracks beneath contraction joints, can enhance the long-term durability and service life of concrete overlays by aiding in cracking resistance and slowing the infiltration of water and incompressible materials.

Fibers may also benefit overlay performance by enhancing aggregate interlock across joints. Many concrete overlays are too thin to allow the placement of dowel bars at transverse joints and/or tie bars at longitudinal joints (Fick et al. 2021). The absence of joint reinforcement often accelerates the loss of aggregate interlock over time. In plain concrete overlays, the loss of aggregate interlock has been tied to reduced load transfer efficiency (LTE), increased pavement roughness, faulting, and joint misalignment/panel movement (King and Roesler 2014a, Barman et al. 2021, Fick et al. 2021).

Laboratory testing (Barman and Hansen 2018), finite element modeling (Kim and Bordelon 2017b), and measurements of load transfer and pavement smoothness on FRC overlays in the field (King and Roesler 2014a, Barman et al. 2021) have suggested that the ability of fibers to enhance aggregate interlock relative to plain concrete improves LTE and reduces the potential for faulting in FRC overlays. While fibers are not a direct substitute for dowel bars or tie bars, these promising results to date indicate that fibers can improve joint performance in thin overlays.

Enhancements to aggregate interlock may also improve pavement performance by reducing curling and warping stresses that develop from moisture and temperature gradients (Kim and Bordelon 2017b). Reductions in curling and warping may improve overlay smoothness as well as fatigue life. Additionally, field observations have shown that FRC overlays appear less prone to joint misalignment than plain overlays, which could prevent early distresses (King and Roesler 2014a).

Related to joint performance, researchers have also investigated whether it might be feasible to use FRC to extend typical joint spacing designs for concrete overlays. Generally, pavement design tools predict improved performance in overlays with shorter transverse joint spacing designs. With longer joint spacings, stresses due to traffic loads increase, and load transfer may be lost as joints open up wider, reducing the amount of aggregate interlock. Early-age mid-slab cracking can also occur when transverse joint spacing extends too far beyond design limits. For these reasons, many thin concrete overlays (6 in. thick or less) in particular are constructed with shorter joint spacings (e.g., 6 ft x 6 ft) than conventional pavements (12 ft x 12 ft or greater) (Gross et al. 2019).

That said, there are also potential downsides to placing more joints in concrete pavements. As previously mentioned, joints are often focal points for durability-related distresses in concrete

pavements. Additionally, field observations have found that not all joints in thinner concrete overlays activate, i.e., cracks do not form beneath all sawcut control joints (Gross et al. 2019). Overlays with unactivated joints may develop dominant joint behavior, where certain joints open up to a much wider extent than others. Dominant joint behavior can lead to poor performance outcomes, such as a loss of load transfer at the dominant joints and significant variation in LTE between adjacent activated and unactivated joints (King and Roesler 2014a).

Therefore, it might be advantageous to evaluate whether the addition of fibers may allow for concrete overlay designs with extended joint spacing. The use of fibers could potentially balance the benefits of using shorter slabs while considering that not all joints may activate as intended. Fibers have been used successfully to extend typical joint spacing design limits in floor slabs while avoiding mid-slab cracking and other performance issues (ACI 2018), indicating the potential to extend joint spacing in a similar way in FRC overlays.

Finally, testing and finite element modeling has shown that fibers may improve the long-term bond between a concrete overlay and underlying pavement, which is an important factor in thickness design and fatigue life (Kim and Bordelon 2017b). This effect likely results from narrower crack widths below sawcut joints, as debonding often begins to develop at the joints.

1.4. Typical FRC Overlay Applications

Many FRC overlays have been constructed successfully on roadway, parking lot, and industrial pavements since the development of modern synthetic macrofibers. Most FRC overlays in the United States contain synthetic macrofibers at a dosage rate of 0.2% to 0.5% by volume, which generally targets a residual strength of about 20% to 30% of the design flexural strength (Bordelon and Roesler 2012). At this dosage rate, the addition of synthetic macrofibers does not affect mixing time at the batch plant or the workability of the fresh concrete. Two common standard test methods for determining the residual strength of any combination of macrofiber and dosage rate are ASTM C1609 and ASTM C1550 (ACI 2018). In practice, it is common for agencies to maintain a list of approved fibers with prescribed dosage rates to achieve a minimum residual strength performance (Roesler et al. 2019).

Fiber reinforcement is usually used in relatively thin overlays that are between 4 and 6 in. thick; these overlays are most often concrete on asphalt–bonded (COA–B) or concrete on asphalt–unbonded (COA–U) overlays but sometimes also concrete on concrete–unbonded (COC–U) overlays (King and Roesler 2014a, Gross et al. 2019, Barman et al. 2021, Fick et al. 2021). These thinner overlays have generally provided the best value proposition for using fibers for several reasons.

First, in many cases, thinner overlays are constructed when there are geometric constraints that make it challenging to significantly raise the grade. In these types of situations, FRC can be used to meet or increase the desired design life without increasing overlay thickness. Additionally, the utility of fibers may be maximized in overlays that are too thin to accommodate dowel bars and/or tie bars. Finally, because fibers are dosed as a function of volume, it becomes relatively more expensive to incorporate fibers as overlay thickness increases. In thicker overlays, the

marginal performance benefits of adding fibers may not be worth the cost or may not compare favorably to the marginal cost of continuing to increase overlay thickness.

1.5. Research Objectives

The known properties of FRC and the experience of using fibers in concrete overlays offer promising evidence of good performance and improved pavement properties. However, a number of the additional potential benefits of using FRC in concrete overlays discussed in Section 1.3 have yet to be fully investigated in practice, including the impact of fibers on pavement smoothness, LTE, curling/warping, and the ability to extend joint spacing. Notably, there are no existing design tools or methods for concrete overlays that account for the impact of fibers on any of those aforementioned properties.

The primary objective of this study was to more fully characterize the behavior and performance of FRC overlays in the field. Six FRC overlay project sites in Iowa were identified for study. These sites included five COA overlays, including overlays categorized both as COA–B and COA–U overlays, and one COC–U overlay. Three of these sites included test sections with varying thickness and joint spacing designs, which allowed for a wide investigation of how each of these design parameters impacted the behavior of a variety of different concrete overlay designs.

A variety of test methods were used at each project site to characterize pavement behavior and performance, including tests to evaluate joint activation, LTE, the structural properties of pavement layers, roadway smoothness, and curling and warping behavior. The testing performed in this study allowed for a thorough analysis of the behavior of different types of concrete overlays, both with and without fiber reinforcement.

2. METHODOLOGY

2.1. Concrete Overlay Sites

As previously mentioned, approximately 12 FRC overlay projects with synthetic macrofiber reinforcement have been constructed in Iowa in recent years. Three of these projects included test sections with varying thickness and joint spacing designs, as well as control sections without fibers. These test sections offer a great opportunity to evaluate the impact of different design parameters on the behavior and performance of overlays. This study chose six different FRC overlay projects constructed between 2017 and 2021 for investigation, including the three projects that featured test sections.

Table 1 lists project details and design parameters for the typical section at each site. The sites included five COA overlays and one COC–U overlay. A 6 in. COA overlay can be considered either a COA–B or COA–U overlay depending on the design intent, but all of the COA overlays in this study were designed and categorized as COA–U overlays. The fiber dosage rate at each project, 4 lb/yd^3, corresponded to about 0.3% by volume. This dosage rate was selected consistent with guidance from Roesler et al. (2019) to achieve a residual strength of 150 psi. The truck traffic data for Sites 1 through 6 as a percentage of average annual daily traffic (AADT) are estimates, as truck traffic counts are not available for county highways in Iowa.

Table 1. Typical design details for concrete overlay test sites

Design Parameters	Site 1	Site 2	Site 4	Site 5	Site 6	Site 7
Location	Worth County	Worth County	Mitchell County	Mitchell County	Buchanan County	Woodbury County
Route	County Highway 105	County Highway 105	County Highway 105	County Highway T26	County Highway V62	Iowa Highway 31
Overlay Type	COA–U	COA–U	COA–U	COA–U	COC–U	COA–U
Underlying Pavement	3 in. HMA over 7 in. PCC	3 in. HMA over 7 in. PCC	3 in. HMA over 7 in. PCC	6 in. HMA	7 in. PCC	7 in. milled HMA
Construction Date	October 2021	October 2019	August 2017	May 2019	August 2018	August 2020
Overlay Thickness (in.)	6	6	6	6	6	6
Joint Spacing (ft) (Transverse x Longitudinal)	12 x 12	12 x 12	12 x 12	12 x 12	11 x 11	12 x 12
Traffic (AADT)	960	1680	760	1040	1390	1240
Truck Traffic (%)	20	20	20	20	20	19
Separation Layer	n/a	Geotextile	n/a	n/a	Geotextile	n/a
Fiber Reinforcement (lb/yd^3)	4	4	4	4	4	4
Fiber Product	GRT Advantage	Forta-Ferro	Forta-Ferro	Forta-Ferro	Forta-Ferro	Forta-Ferro

One unique feature of Site 2 was that even though it was a COA–U overlay, it was constructed with a geotextile separation layer between the concrete overlay and the underlying asphalt, preventing any possible bond between the concrete and asphalt layers. Normally, separation layers are only used on COC–U overlays. Note that Site 3 is not missing from the table but was a special test site that is evaluated separately in Appendix D.

From the typical sections at Site 4, Site 6, and Site 7, test sections were constructed with varying thicknesses, joint spacings, and both with and without fibers. Tables 2 through 4 list the design details of each of the test sections. At each site, the test sections were labeled individually as their own site, e.g., Site 4A, Site 4B, and so on. Each test section at Site 4 was 500 ft in length, each test section at Site 6 was 300 ft in length, and each test section at Site 7 was 1,000 ft long. Note that since thicknesses were reduced to 4 in. at Sites 4A through 4H, these sites were classified as COA–B overlays. These sites were distinct from the typical sections and the other test sections at Site 4, which were classified as COA–U overlays.

Table 2. Site 4 test section design details

Site	Overlay Type	Thickness (in.)	Joint Spacing (ft) (Transverse x Longitudinal)	Fiber Reinforcement (lb/yd^3)
4A	COA–B	4	6 x 6	0
4B	COA–B	4	12 x 12	0
4C	COA–B	4	15 x 12	0
4D	COA–B	4	20 x 12	0
4E	COA–B	4	20 x 12	4
4F	COA–B	4	15 x 12	4
4G	COA–B	4	12 x 12	4
4H	COA–B	4	6 x 6	4
4I	COA–U	6	6 x 6	4
4J	COA–U	6	12 x 12	4
4K	COA–U	6	15 x 12	4
4L	COA–U	6	20 x 12	4
4M	COA–U	6	20 x 12	0
4N	COA–U	6	15 x 12	0
4O	COA–U	6	12 x 12	0
4P	COA–U	6	6 x 6	0

Table 3. Site 6 test section design details

Site	Overlay Type	Thickness (in.)	Joint Spacing (ft) (Transverse x Longitudinal)	Fiber Reinforcement (lb/yd^3)
6A	COC–U	6	11 x 11	0
6B	COC–U	6	5.5 x 5.5	4
6C	COC–U	6	11 x 11	4
6D	COC–U	6	15 x 11	4
6E	COC–U	6	20 x 11	4
6F	COC–U	6	30 x 11	4
6G	COC–U	6	40 x 11	4
6H	COC–U	6	40 x 11	0
6I	COC–U	6	30 x 11	0
6J	COC–U	6	20 x 11	0
6K	COC–U	6	15 x 11	0
6L	COC–U	6	5.5 x 5.5	0

Table 4. Site 7 test section design details

Site	Overlay Type	Thickness (in.)	Joint Spacing (ft) (Transverse x Longitudinal)	Fiber Reinforcement (lb/yd^3)
7A	COA–U	6	6 x 6	0
7B	COA–U	6	15 x 12	4
7C	COA–U	6	12 x 12	4
7D	COA–U	6	9 x 12	4
7E	COA–U	6	9 x 6	4
7F	COA–U	6	6 x 6	4

2.2. Performance Prediction

To complement the field testing program, this study used a variety of concrete overlay design tools to predict the long-term performance of each test site. These performance predictions established baseline performance expectations for the overlays at each site and for performance trends related to different design parameters, such as thickness, joint spacing, and fiber reinforcement. The performance predictions also served as a useful point of comparison for the results of the field testing.

Currently, there are multiple viable software tools for designing each type of concrete overlay, and no one design method is capable of considering all possible combinations of design parameters for all overlay types (Fick et al. 2021). Each of these tools may employ different methodologies; restrict users from considering certain design inputs, such as allowable combinations of thickness and joint spacing; and allow users to consider different types of performance indicators, such as cracking, faulting, and pavement smoothness in terms of International Roughness Index (IRI). For this study, multiple design tools were selected for each test site (when possible) to capture a broad assessment of predicted performance.

Three software tools were used for performance prediction. The first design tool was Pavement ME Design (PMED) (AASHTO 2008), which included the following three modules that were applied to the overlay sites in this study:

- The jointed plain concrete pavement (JPCP) over asphalt concrete (AC) module was used to evaluate COA–U designs with a transverse joint spacing of 12 ft or greater. Two separate design runs were performed at each site using the JPCP over AC module, one assuming no bond between the concrete and underlying asphalt and another assuming that the layers started out as bonded.
- The short jointed plain concrete pavement (SJPCP) over AC module (ARA 2016) was used to evaluate COA–U and COA–B designs with a transverse joint spacing of 9 ft or less. This module always assumes a bond between the two layers.
- The JPCP over JPCP (Unbonded) module was used to evaluate COC–U designs with a transverse joint spacing of 12 ft or greater. This module was also used to evaluate the COA–

U design at Site 2, given its resemblance to a COC–U overlay due to the separation layer between the overlay and underlying asphalt.

The second design tool was BCOA-ME (Li et al. 2019), which was used to evaluate all COA designs with a transverse joint spacing of 15 ft or less, except for Site 2. (Note that BCOA-ME is not able to consider joint spacings greater than 15 ft.)

The third design tool was UNOL Design for COC–U overlays (Khazanovich et al. 2020), which was also used to evaluate COC–U designs with a transverse joint spacing of 15 ft or less, including Site 2. Like BCOA-ME, UNOL Design cannot consider joint spacings greater than 15 ft.

Given the importance of joint spacing to this study, it was critical to select design tools that accounted for joint spacing in design and performance prediction. Therefore, PavementDesigner.org (Ferrebee et al. 2018) was not considered in this analysis.

Table 5 contains a full rundown of each of the design methods and modules used for each project and their corresponding performance indicators. It was not possible to evaluate each test site using multiple methods due to restrictions on design inputs in the various software tools. No performance predictions were possible for Sites 4D and 4E, as no existing methods are able to run a design case for a 4 in. overlay with 20 ft transverse joint spacing. All design runs were carried out to a design life of 40 years.

Table 5. Design tools, modules, and predicted performance indicators for each test site

Design Tool and Module	Test Sites	Performance Indicators
PMED, JPCP over AC (No Bond)	1, 2, 4J, 4K, 4L, 4M, 4N, 4O, 5, 7B, 7C, 7D	Cracked slabs, mean joint faulting, IRI
PMED, JPCP over AC (Bond)	1, 4J, 4K, 4L, 4M, 4N, 4O, 5, 7B, 7C, 7D	Cracked slabs, mean joint faulting, IRI
PMED, SJPCP over AC	4A, 4H, 4I, 4P, 7A, 7E, 7F	Cracked slabs
PMED, JPCP over JPCP (Unbonded)	2, 6A, 6C, 6D, 6E, 6F, 6G, 6H, 6I, 6J, 6K	Cracked slabs, mean joint faulting, IRI
BCOA-ME	1, 4A, 4B, 4C, 4F, 4G, 4H, 4I, 4J, 4K, 4N, 4O, 4P, 5, 7A, 7B, 7C, 7D, 7F	Cracked slabs, mean joint faulting
UNOL	6A, 6B, 6C, 6D, 6L	Cracked slabs, mean joint faulting

2.3. Visual Distress Surveys

Visual distress surveys were performed to assess cracking and any other distresses or notable features observed at each overlay site. At Site 1, Site 2, and Site 5, a portion of roadway approximately 1,000 ft long was selected as the area of investigation for the distress surveys (as well as for all subsequent testing). Meanwhile, surveys were conducted over the entire length of

each of the test sections at Site 4, Site 6, and Site 7. The results of the surveys were reported in terms of percentage of slabs affected by the distress, e.g., percent of slabs cracked.

2.4. Ultrasonic Tomography for Joint Activation

2.4.1. Method Background

The MIRA ultrasonic shear wave tomography device, pictured in Figure 3, consists of a 4 x 12 array of point transducers and is used for a variety of applications in concrete elements and structures, including the detection of voids, reinforcing steel, and delamination, as well as thickness and cover depth. For concrete pavements, Tran and Roesler (2020) developed a method to assess whether a crack has developed beneath a sawcut by taking a measurement at the surface directly over the joint.

Tran and Roesler 2020

Figure 3. MIRA ultrasonic shear wave device and laptop

The MIRA operates using a pitch-catch method, where one transducer emits an ultrasonic pulse while the rest receive the pulse. When the device is placed over a joint, as in Figure 4, it is possible to infer whether a crack has developed beneath the sawcut by comparing the amount of energy received from the pulse by transducers on either side of the joint. If a crack has propagated to the bottom of a concrete slab, the crack will reflect a significant portion of the wave energy, and transducers on the opposite side of the joint from the pulse will receive less energy than the transducers on the same side of the pulse.

Figure 4. MIRA testing on a concrete pavement for joint activation

Tran and Roesler (2020) established a normalized energy threshold to determine whether or not a joint has activated and developed an algorithm to interpret the results. During the development of this method, Tran and Roesler (2020) found that the MIRA method assessed joint activation with an accuracy of 96% in laboratory testing. Gross et al. (2019) performed the first major field study using this method to assess joint activation in concrete overlays and found an accuracy of 86% compared to visual observations. Erroneous measurements may be more likely to occur in warmer weather. At higher temperatures, cracks in concrete close tighter, and the MIRA method may fail to resolve narrow, hairline cracks (Gross et al. 2019).

2.4.2. MIRA Testing for Joint Activation

This study used the MIRA ultrasonic shear wave tomography device to determine the joint activation rate at each concrete overlay site, i.e., at what percentage cracks developed beneath sawcuts as intended. Testing was conducted at 10 consecutive transverse joints within the area of investigation at each site to assess the rate of joint activation. (At Sites 4F through 4I, where joint spacing was 30 ft or greater, fewer joints were tested because there were fewer than 10 slabs within those test sections.) A total of 10 measurements were taken at each joint, and the algorithm developed by Tran and Roesler (2020) was used to determine whether or not a crack had developed based on these measurements. The percentage of joints at which the crack developed beneath the sawcut was reported as the activation rate, e.g., 70%.

2.5. Falling Weight Deflectometer for Load Transfer Efficiency

2.5.1. Method Background

Falling weight deflectometer (FWD) testing is a method that measures deflection at the pavement surface to evaluate pavement properties and behavior. In FWD testing, a weight is dropped at a given location to apply a load pulse to the pavement while transducers measure the deflection at varying distances from the load plate (Khazanovich and Gotlif 2003). Figure 5 illustrates an example of a typical FWD test setup. FWD testing equipment is commonly mounted on trailers or trucks. Depending on the configuration of the load plate, the sensors, and the configuration of the test, FWD testing can be used to measure a number of pavement properties.

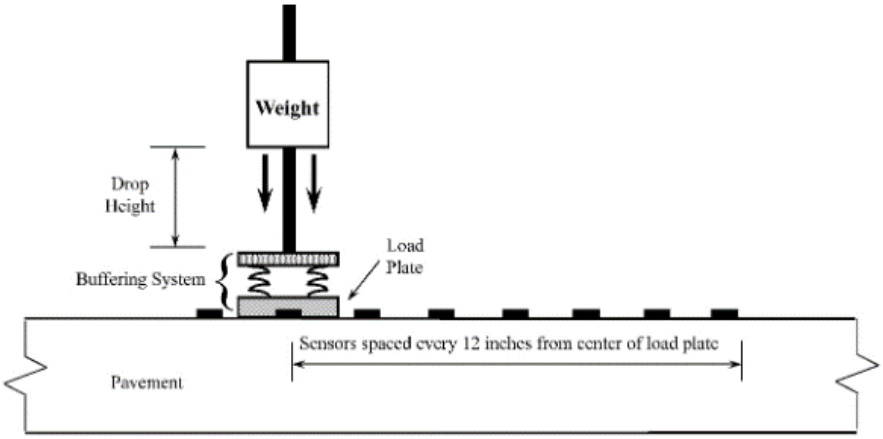

Smith et al. 2017

Figure 5. Illustration of a typical FWD test setup

FWD testing conducted at transverse joints can assess the joint LTE, a measure of how evenly adjacent slabs deflect as a load applied to one slab is transferred to the other slab. Load transfer is provided by the aggregate interlock (contact between aggregate particles beneath the sawcut joint), by the reinforcement provided by dowel bars (when they are present), and through underlying pavement layers. Load transfer is particularly important for transverse joints, as they are traversed by vehicle loads. Poor load transfer can increase slab deflections and stresses and in the long-term may lead to faulting and increased pavement roughness (Khazanovich and Gotlif 2003). Figure 6 illustrates examples of poor and good load transfer.

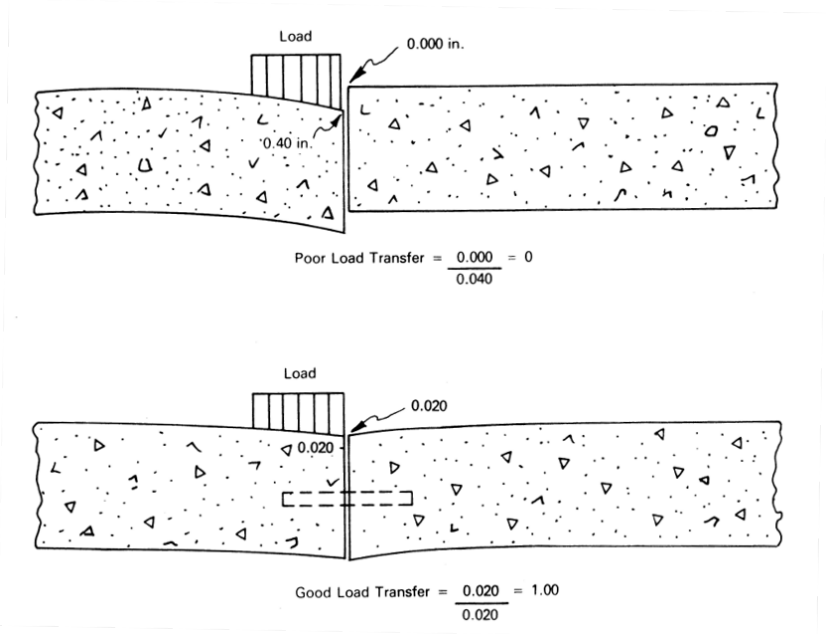

AASHTO 1993

Figure 6. Illustration of poor (top) and good (bottom) load transfer

During an FWD test to measure joint LTE, the load plate is stationed at the edge of one slab, directly adjacent to the joint, as pictured in Figure 7. A load anywhere from 3,000 to 50,000 lbf is applied to the load plate, and deflections are measured directly under the load plate and across the joint at a distance equal to the radius of the load plate (Smith et al. 2017). LTE is then calculated according to equation (1), where d_u is the deflection measured in the unloaded slab and d_l is the deflection measured under the load plate in the loaded slab. LTE values may range from 0% to 100%. Table 6 presents a commonly used categorization of load transfer quality based on LTE values.

Figure 7. FWD test at a transverse joint

$$LTE = \frac{d_u}{d_l} \times 100\% \quad (1)$$

Table 6. Joint LTE quality

Categorization	LTE Values
Excellent	90% to 100%
Good	75% to 89%
Fair	50% to 74%
Poor	25% to 49%
Very Poor	0% to 24%

Smith et al. 2017

2.5.2. FWD Testing to Evaluate Joint LTE

This study conducted FWD testing at transverse joints to measure LTE at each concrete overlay test site. Testing was performed at a total of 10 transverse joints within the area of investigation at each test site. Three successively increasing loads (9,000 lbf, 12,000 lbf, and 15,000 lbf) were applied to the load plate on both the approach and leave side of each joint, resulting in six total tests at each transverse joint. Deflections were measured directly underneath the load plate (which had a radius of 6 in.) and 12 in. from the center of the load plate on the unloaded slab. These six measurements were averaged to determine the LTE at each transverse joint. The

results at all 10 joints were also averaged together to calculate the average transverse joint LTE at each test site.

2.6. Falling Weight Deflectometer for Structural Backcalculation

2.6.1. Method Background

In addition to evaluating load transfer, researchers have developed a number of methodologies over the years to use FWD testing to backcalculate layer properties and thicknesses for both concrete and asphalt pavements (Pierce et al. 2017). FWD backcalculation works by measuring deflections at various distances from the load plate and using them to characterize a deflection basin, which is illustrated in Figure 8.

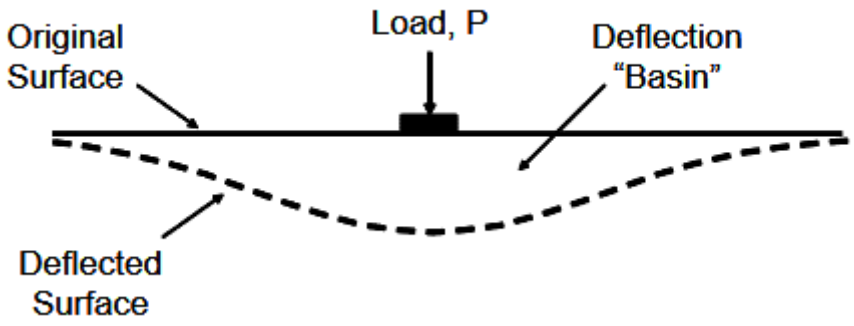

Figure 8. Schematic of the deflection basin under an FWD load plate

Pavement deflection under loading is influenced by the response of all pavement layers, including the surface layer, base and subbase layers, and the subgrade. Backcalculation procedures analyze the deflection basin obtained by FWD testing and relate it to the engineering properties of pavement layers according to fundamental models of pavement behavior under loading. These models are generally based on layered elastic theory for flexible pavements and plate theory for rigid pavements (Smith et al. 2017).

One of the most common approaches used for concrete pavement backcalculation is a closed-form procedure initially developed by Barenberg and Ioannides (1989). This procedure first characterizes the deflection basin in terms of a parameter known as $AREA_{36}$, which is calculated from deflections d_0, d_{12}, d_{24}, and d_{36} at distances of 0, 12, 24, and 36 in. from the FWD load plate, respectively, and their distance from the load plate. Note that the *AREA* deflection basin can be characterized using any combination of sensor spacings and distances from the load plate for backcalculation (Hall et al. 1997). For simplicity, only the procedure for $AREA_{36}$ is detailed here.

Ioannides (1990) showed that there is a unique relationship between $AREA_{36}$ and the radius of relative stiffness, ℓ, of the loaded area, a. Based on this relationship, the deflection basin can be used to backcalculate Westergaard's (1926) maximum interior deflection of an infinite slab, W_{int}.

From there, it is possible to backcalculate the modulus of subgrade reaction, *k*, which characterizes the combined stiffness of the subgrade and subbase layers. Finally, either the elastic modulus, *E*, or the thickness, *h*, of the concrete slab can be backcalculated as long as a value is known or assumed for either *E* or *h*. Equations (2) through (6) show the primary calculations behind this backcalculation procedure, where *P* is the FWD load and *v* is Poisson's ratio for concrete.

$$AREA_{36} = 6\left(1 + 2\frac{d_{12}}{d_0} + 2\frac{d_{24}}{d_0} + \frac{d_{36}}{d_0}\right) \quad (2)$$

$$\ell = \left[\frac{ln\left(\frac{36 - AREA_{36}}{1812.279133}\right)}{-2.559340}\right]^{4.387009} \quad (3)$$

$$W_{int} = \frac{1}{8}\left[1 + \left(\frac{1}{2\pi}\right)\left(ln\left(\frac{1.7810725a}{2\ell}\right) - \frac{5}{4}\right)\left(\frac{a}{\ell}\right)^2\right] \quad (4)$$

$$W_{int} = \frac{kd_0\ell^2}{P} \quad (5)$$

$$\ell = \left[\frac{Eh^3}{12(1-\nu^2)k}\right]^{0.25} \quad (6)$$

2.6.2. Applying Backcalculation to Concrete Overlays

To apply this backcalculation procedure to concrete overlays, there are two additional factors to consider. First, it is necessary to correct for slab size. The procedure outlined in equations (2) through (6) was developed assuming a slab with infinite dimensions. However, Crovetti (1994) showed that finite slab sizes can affect the deflection basin and developed correction factors to account for joint spacing and load transfer between slabs. King and Roesler (2014b) further iterated on this procedure to account for the fact that a different *AREA* term from $AREA_{36}$ was needed to analyze the deflection basin for overlays with a shorter joint spacing design. King and Roesler (2014b) developed an $AREA_{24}$ term that considered deflections up to a maximum of 24 in. away from the load plate and derived the relationship between $AREA_{24}$ and the radius of relative stiffness for concrete overlays with a joint spacing of 6 ft or less.

Second, it is necessary to make simplifying assumptions to account for the complexity of a concrete overlay system, which can have multiple types of pavement layers and several possible bond and friction conditions at the various layer interfaces. For COA overlays, King and Roesler (2014b) proposed assuming that the concrete overlay and the underlying bonded asphalt layer act together monolithically during backcalculation. From there, it is possible to assume a single modulus value for the bonded portland cement concrete (PCC) and hot mix asphalt (HMA) layers and backcalculate the effective thickness, h_{eff}, of the combined layer. This simplification, illustrated in Figure 9, is also made by the SJPCP over AC design module in PMED for the design of COA–B overlays (ARA 2016).

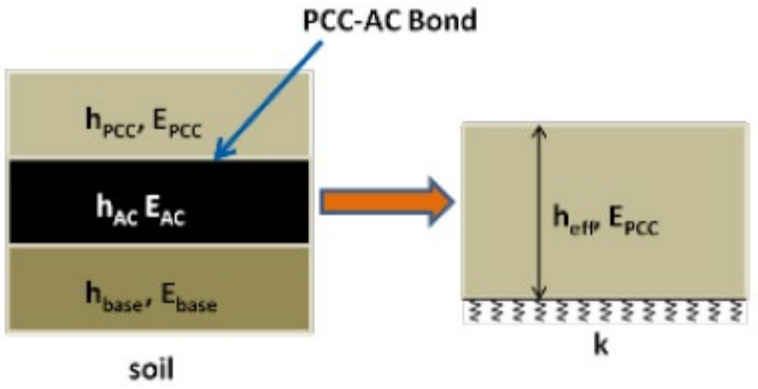

King and Roesler 2014b

Figure 9. Single layer assumption for COA overlays

If the concrete and asphalt layers are well bonded and act together monolithically under load, the backcalculated h_{eff} value should be close to the combination of the design thickness of the PCC layer and the remaining thickness of the existing asphalt layer. (The value will likely be somewhere in between the combined thickness of these layers, as asphalt has a lower elastic modulus than concrete.) If the concrete and asphalt are not bonded, the backcalculated h_{eff} value should match the concrete overlay design thickness, and the structural response of the asphalt layer should be captured in the k value. Therefore, this backcalculation process can be used to infer whether or not the concrete and asphalt layers are bonded in a COA overlay. The ability to assess the bond condition is of particular interest for analyzing the performance of COA–U overlays, because even though they are not necessarily designed to bond to the underlying asphalt, they have frequently been observed to bond in practice (Fick et al. 2021).

Meanwhile, backcalculation of COC–U overlays can be performed in the same fashion as conventional concrete pavements, correcting for slab size. For COC–U overlays, the structural response of the separation layer and the underlying concrete pavement is captured in the k value.

2.6.3. FWD Testing for Structural Backcalculation

This study performed center slab FWD testing at each test site to backcalculate the structural properties of the concrete overlay sections. Testing was performed at the same 10 slabs that were tested for joint LTE at each site but with the load plate oriented at the center of the slab. Like the testing at transverse joints, three successively increasing loads (9,000 lbf, 12,000 lbf, and 15,000 lbf) were applied to the load plate when testing each slab.

The deflection under the load plate, D_0, was recorded for each test, and then $AREA_{24}$ or $AREA_{36}$ terms (depending on the joint spacing) were calculated and used to backcalculate the radius of relative stiffness, ℓ, the modulus of subgrade reaction, k, and effective thickness, h_{eff}. A concrete modulus value, E_{PCC}, of 4,000,000 psi and Poisson's ratio, v, of 0.15 were assumed to perform the backcalculation. The average values obtained from the three FWD drops at all 10 slabs were then averaged together to produce averages for each test site.

2.7. High-Speed Surface Profiling

2.7.1. Method Background

A high-speed inertial profiler system is a common piece of equipment used to assess smoothness and other surface characteristics of both concrete and asphalt pavements. These profiler systems consist of laser sensors, accelerometers, and distance measuring instruments that are mounted to a vehicle and designed to collect data at traffic speed (Karamihas et al. 1999). As the vehicle travels down a roadway, the profiler measures the elevation of the pavement surface as a function of longitudinal distance, correcting the elevation for the vertical displacement of the vehicle itself. These systems also commonly contain other items, such as a control box, Global Positioning System (GPS) unit, and/or a camera, and are generally connected to a computer inside the vehicle to control their operation. Figure 10 shows an example of a truck-mounted profiler system.

Tian et al. 2023

Figure 10. Truck-mounted high-speed profiler system

2.7.1.1. Profiling to Measure Pavement Smoothness

The most common use of high-speed profilers is to measure pavement smoothness. Thanks to their ability to collect data at traffic speed, pavement surface profilers are capable of collecting significant quantities of data at both the project and network level. The most widely used method to relate profile measurements to pavement smoothness is to calculate the IRI (ASTM 2021).

IRI was first developed by the World Bank in the 1980s to establish a global standard for pavement smoothness measurements (Sayers et al. 1986). IRI is calculated by processing pavement profile data through an algorithm known as the quarter-car model, which simulates the deflection of the suspension of a passenger car as it traverses the longitudinal pavement profile

(Karamihas et al. 1999). IRI is measured in units of inches per mile, with the scale beginning at zero and increasing as pavement roughness increases (ASTM 2021).

Pavement smoothness is important to the traveling public, and the Federal Highway Administration (FHWA) requires state highway agencies to regularly assess and measure the IRI of pavements in their networks. These requirements have led IRI to become an important component of many state and local agencies' pavement condition assessment and asset management programs, and IRI is also commonly used in specifications for measuring acceptable pavement roughness in new construction (Smith and Ram 2016). Table 7 shows the IRI rating system established in 23 C.F.R. § 490.313 (2017).

Table 7. US federal IRI rating criteria

Condition	IRI (in./mi)
Good	< 95
Fair	95 to 170
Poor	> 170

2.7.1.2. Profiling to Measure Curling and Warping

Beyond pavement smoothness, it is also possible to characterize the degree of curling and warping in concrete pavements from the surface profile. Concrete slabs experience deformation due to the presence of temperature and moisture gradients between the top and bottom of the slab. When caused by temperature gradients, this phenomenon is commonly referred to as curling, and when caused by moisture gradients, this phenomenon is known as warping (Ceylan et al. 2016). Figure 11 contains an illustration of curling and warping behavior in concrete slabs.

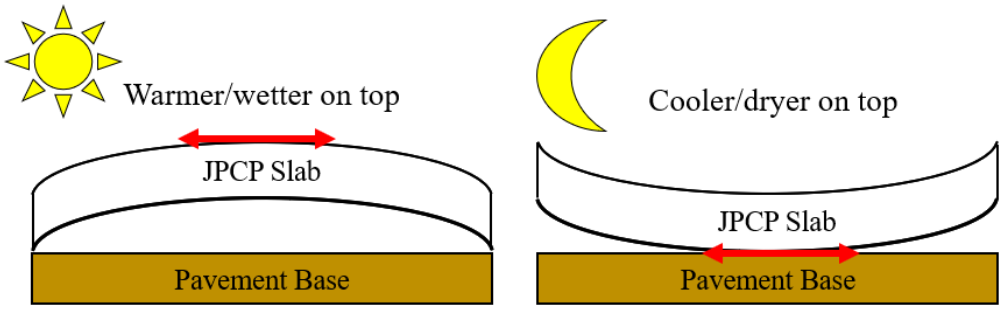

Yang et al. 2023

Figure 11. Curling and warping behavior of concrete pavement slabs

Temperature and moisture gradients develop and change over the course of a given day (diurnally) as well as at different times of year (seasonally) (Chang et al. 2008). For example, in the afternoon, the top of the slab tends to be warmer than the bottom of the slab. This positive temperature gradient leads the top of the slab to expand relative to the bottom of the slab, causing its shape to "curl" downward.

In addition to changes in ambient conditions, concrete slabs have a certain amount of built-in curling and warping due to the temperature and moisture gradients that are present in the concrete slab when it initially sets, as well as shrinkage and moisture loss due to hydration (Nassiri 2011). Built-in curling and warping tend to cause concrete slabs to curl upward, and diurnal and seasonal temperature gradients tend to either accentuate or relax the built-in curled-up shape. That said, studies have also observed concrete slabs that consistently exhibited a curled-down shape, indicating built-in downward curling (Tian et al. 2023).

Curling and warping can be problematic in concrete pavements for two main reasons. First, temperature and moisture gradients cause stresses in concrete slabs, and these stresses can combine with traffic loadings to contribute to fatigue cracking (Choubane and Tia 1995, Wei et al. 2016). Modern pavement design procedures such as PMED account for these stresses when predicting concrete pavement performance (AASHTO 2008). Second, due to the deformation of the surface, curling and warping can also be a significant contributor to pavement roughness (Chang et al. 2008). For certain combinations of climates and concrete materials, curling and warping can cause changes in IRI as great as 30 in./mi in a single day (Merritt et al. 2015).

A number of researchers (Byrum 2000, Chang et al. 2008, Alhasan 2018) have developed methods to detect joints in concrete pavements from a continuous longitudinal profile and use curve-fitting methods to characterize the curled/warped shape of individual slabs. In particular, the second-generation curvature index (2GCI) approach, which fits the shape of the slab according to a second-order polynomial, has emerged as a standard method for characterizing concrete pavement curling and warping from surface profile measurements (Chang et al. 2008). Figure 12 shows an example of a curve fit to the raw elevation profile corresponding to a curled-up concrete pavement slab.

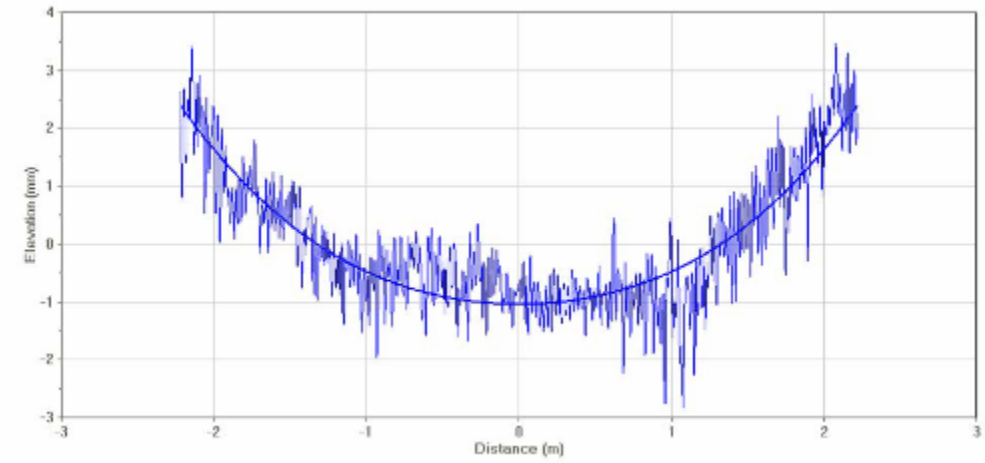

Chang et al. 2008

Figure 12. Fitted profile to characterize concrete slab curling/warping

Building on this work, Tian et al. (2023) developed a MATLAB algorithm to process concrete pavement profile data and characterize curling and warping behavior. This algorithm used the 2GCI fitting model to detect each joint in the profile and produce a curvature profile for the

pavement that consisted only of the fitted curvature profile for each slab, correcting for the grade of each slab. This process is outlined in Figure 13.

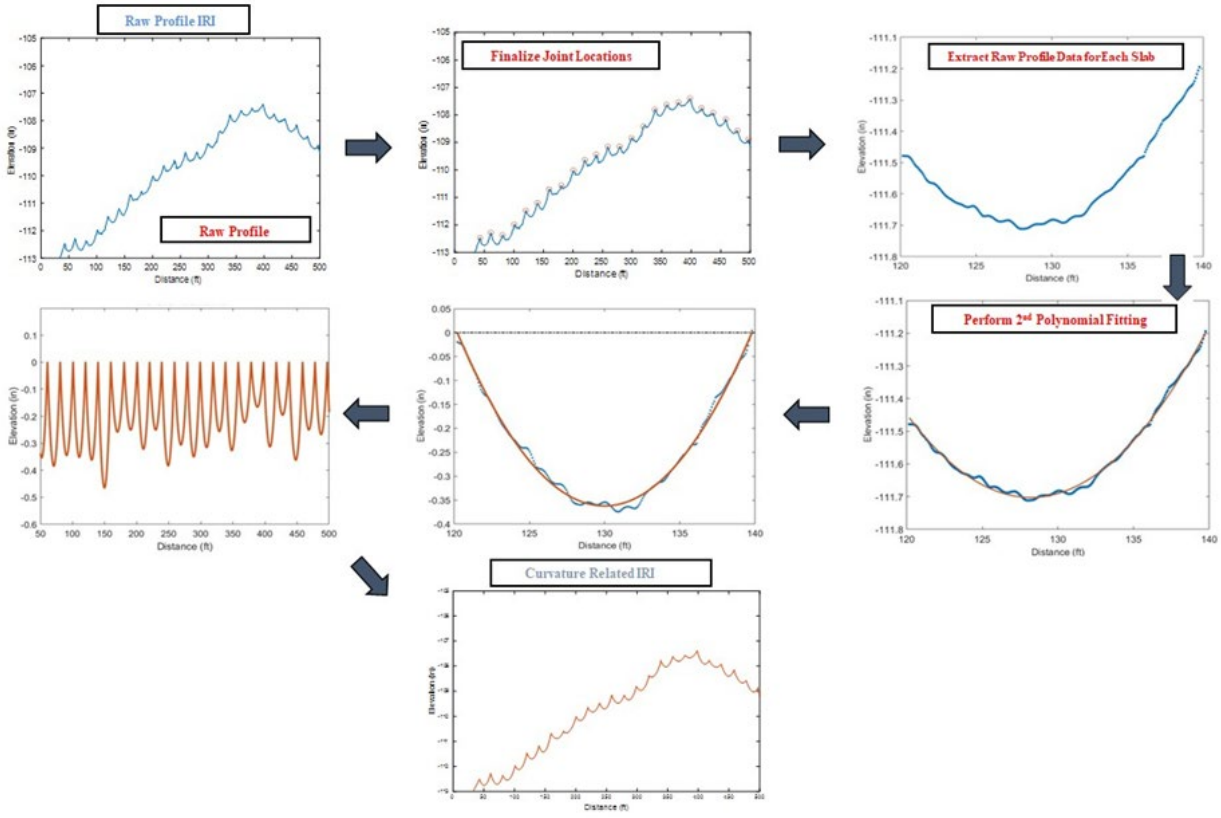

Tian et al. 2023

Figure 13. Overview of MATLAB algorithm to apply 2GCI fitting model

Using the profile obtained from this algorithm, Tian et al. (2023) proposed two different ways to measure the degree of curling and warping in a given pavement section. First, the profile could be input into any type of software capable of calculating IRI from a pavement profile (e.g., ProVAL). The IRI value calculated from this curvature profile could be characterized as the Curvature IRI for the pavement section, or the IRI solely due to curling and warping.

Second, the algorithm also calculated the distance measured between a diagonal line drawn between the two edges of the slab and the point of maximum deflection in the fitted curvature profile. This deflection could be used by itself to measure the degree of curling in a concrete slab and normalized by slab length to characterize the deflection ratio to account for joint spacing (Tian et al. 2023).

2.7.2. Profile Measurements at Concrete Overlay Test Sites

In this study, the truck-mounted high-speed inertial profiler system (SSI CS9300) pictured in Figure 10 was used to record profile measurements at each concrete overlay test site. The profiler consisted of three sensors mounted on the front bumper over the left wheel path, right wheel path, and the center of the vehicle.

Each site was visited three times to collect data, once each in the spring, summer, and fall of 2023. The visits during three distinct times of year were intended to capture any seasonal variation in pavement smoothness and/or curling and warping behavior. No visits were made in the winter due to the difficulty of performing profiling measurements in winter conditions and because Tian et al. (2023) previously found minimal insight into smoothness or curling/warping behavior when attempting to take measurements in the winter.

During each visit, profile measurements were recorded twice per day, once in the morning and once in the afternoon, to capture any diurnal variation in pavement smoothness and/or curling and warping behavior. Three separate profile runs were obtained for each morning and afternoon measurement. The profile runs covered the same area of investigation as previous testing at all test sites, which included the entirety of each of the test sections at Sites 4, 6, and 7.

After the surface profiles were obtained, they were analyzed in ProVAL to obtain measurements of IRI to characterize pavement smoothness. From there, the profiles were analyzed using the algorithm developed by Tian et al. (2023) to characterize curling and warping in terms of Curvature IRI, deflection, and deflection ratio. The results of the three runs were averaged to obtain IRI, Curvature IRI, deflection, and deflection ratio results for each combination of season and time of day, and these results were all averaged together to obtain single values for comparison with other test sites.

3. RESULTS

3.1. Performance Prediction

This section presents the results for predicted cracking and faulting at the end of the 40-year design life for each test site. Data for Sites 1, 2, and 5 are plotted together, while data for Sites 4, 6, and 7 are each plotted separately. The predicted IRI values from PMED for each site are not plotted in this section as there was minimal variation in the IRI predictions between any section, and there were no apparent trends related to thickness, joint spacing, fibers, or bond condition. Appendix A contains the full predicted cracking, faulting, and IRI results for each section.

3.1.1. Sites 1, 2, and 5

Figure 14 plots predicted cracking values at Sites 1, 2, and 5 obtained from PMED, while Figure 15 plots predicted values for the same sites obtained from the BCOA-ME (for Sites 1 and 5) and UNOL (for Site 2) design tools. PMED predicted similar amounts of cracking (between about 1% and 2%) for each of these sites. Meanwhile, BCOA-ME predicted a somewhat higher percentage of cracked slabs for Site 1 (5%) and a much higher percentage of cracked slabs at the end of the design life for Site 2 (20%).

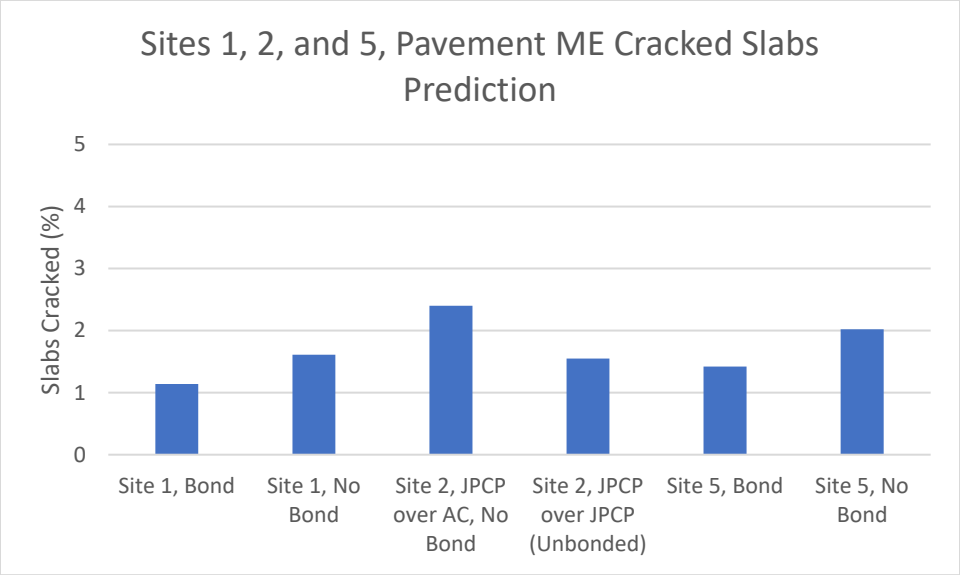

Figure 14. PMED predicted cracking at Sites 1, 2, and 5

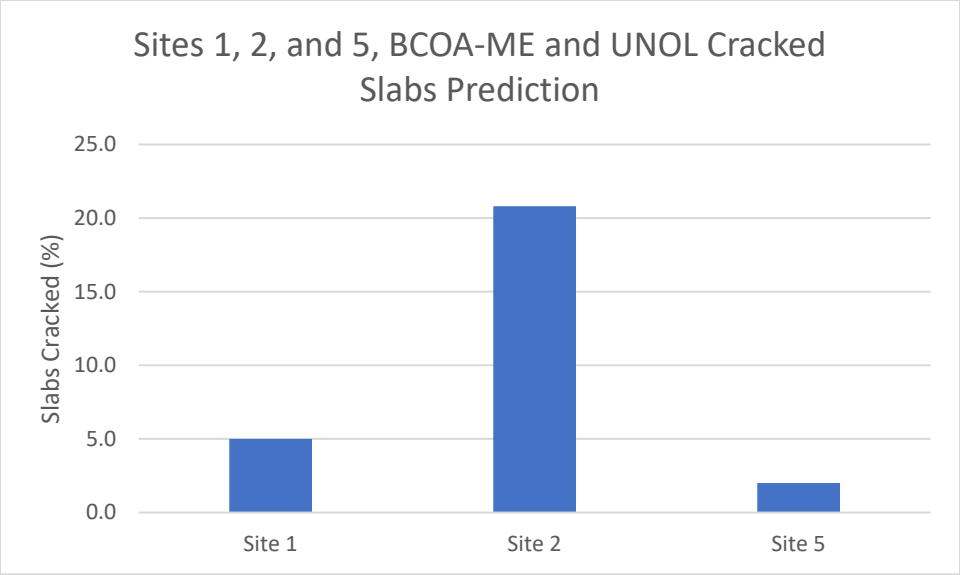

Figure 15. BCOA-ME and UNOL predicted cracked slabs at Sites 1, 2, and 5

Figure 16 plots predicted mean joint faulting at Sites 1, 2, and 5 from PMED, while Figure 17 plots predicted mean joint faulting for the same sites from the BCOA-ME (for Sites 1 and 5) and UNOL (for Site 2) design tools. PMED predicted more faulting for each test site than BCOA-ME and UNOL, which predicted very little (if any) faulting, but PMED faulting predictions were still very low for 40 years.

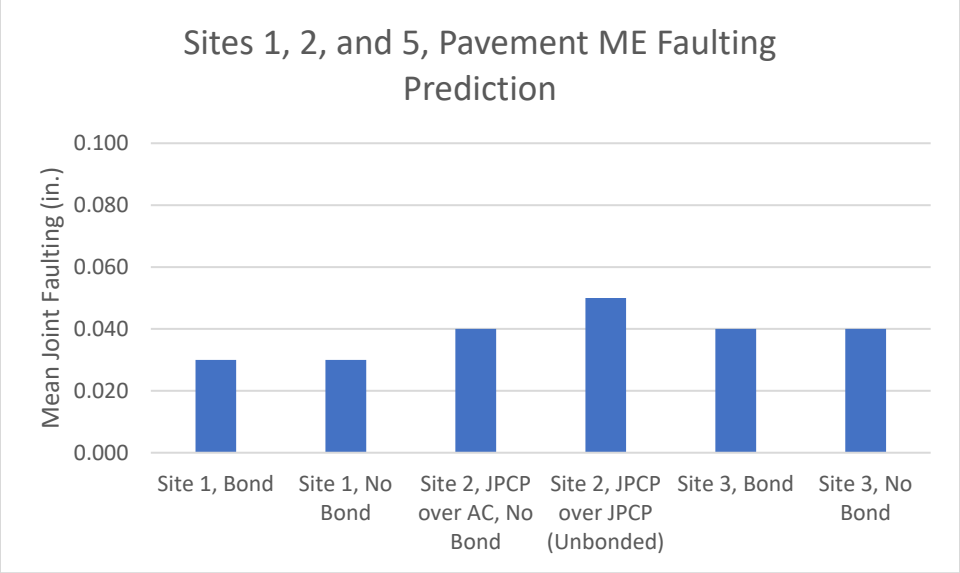

Figure 16. PMED predicted faulting at Sites 1, 2, and 5

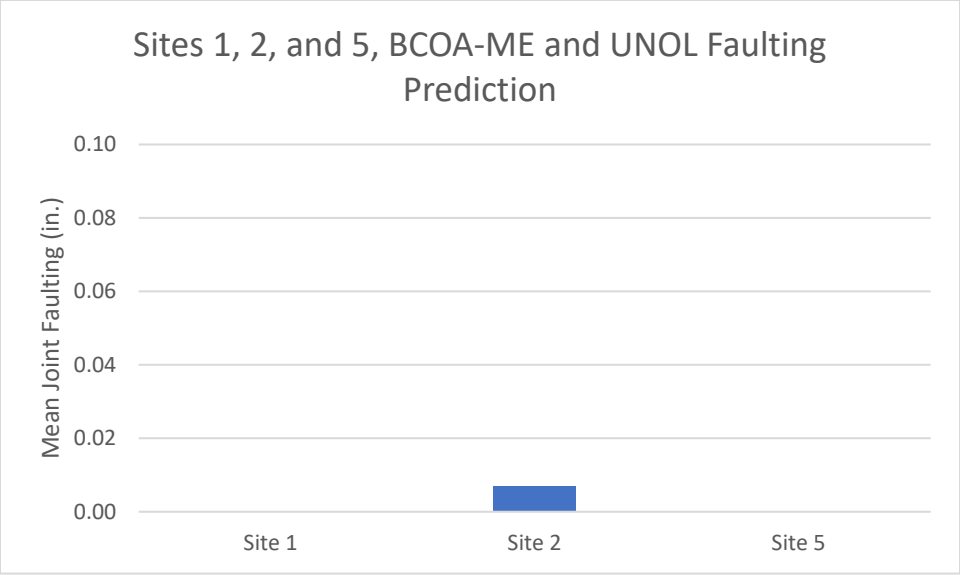

Figure 17. BCOA-ME and UNOL predicted faulting at Sites 1, 2, and 5

3.1.2. Site 4

Figures 18 and 19 plot the predicted cracking values obtained from PMED and BCOA-ME, respectively, for Site 4. The data in Figures 18 and 19 are sorted by joint spacing and assumed bond condition. PMED predicted relatively modest cracking values, with no site exceeding 5% slabs cracked. Predicted faulting increased with joint spacing and was higher for cases with no assumed bond between the concrete and asphalt layers and those without fiber reinforcement.

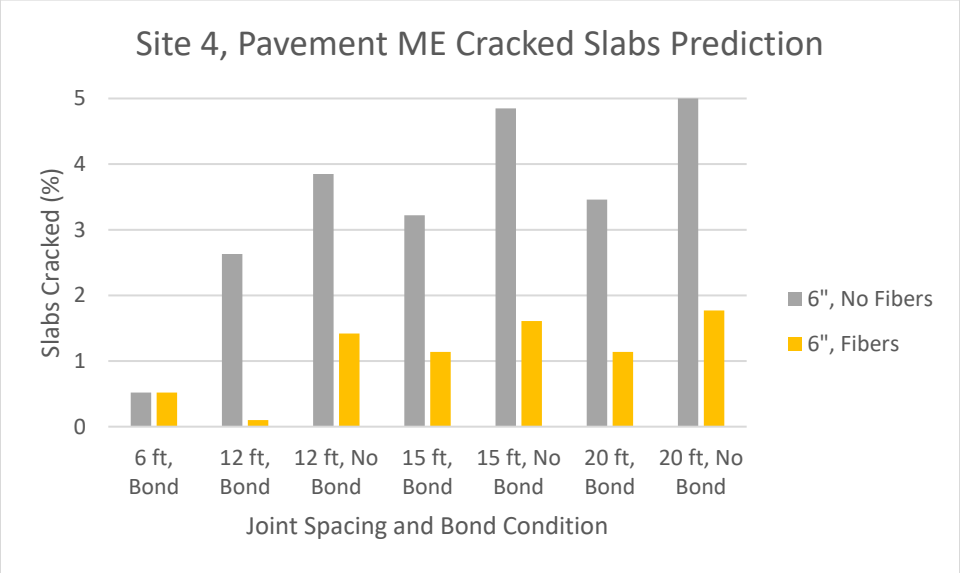

Figure 18. PMED predicted cracking at Site 4

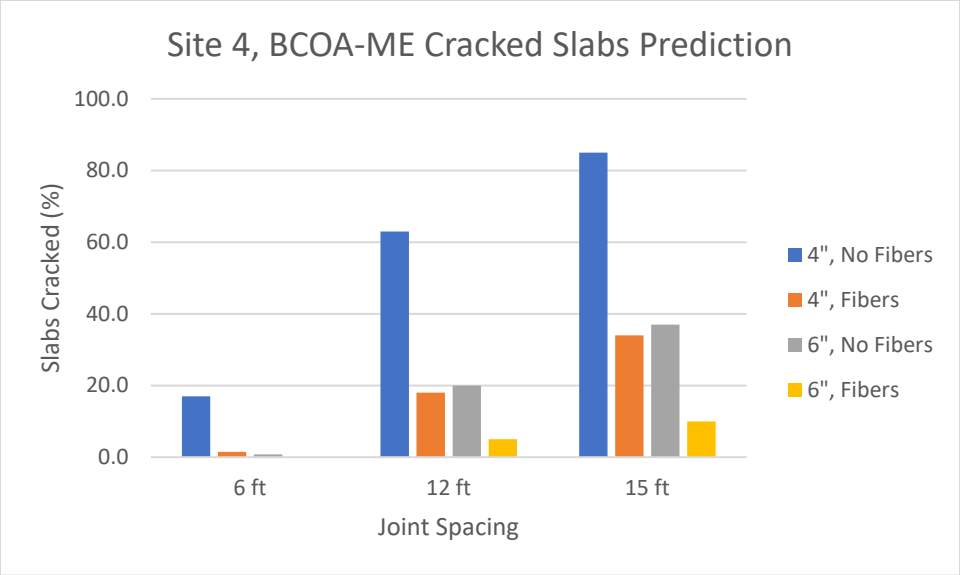

Figure 19. BCOA-ME predicted cracking at Site 4

Meanwhile, BCOA-ME predicted much higher percentages of slabs cracked in all cases, particularly for sites with 12 ft and 15 ft joint spacing. At the sites with 4 in. thickness without fibers, predicted slab cracking ranged from 63% at 12 ft joint spacing to 85% at 15 ft joint spacing. Predicted slab cracking values for the corresponding 4 in. sections with fibers were 18% and 34%, still much higher than predicted by PMED. Increasing the thickness to 6 in. reduced predicted cracking relative to the corresponding 4 in. sections, but values were again still much higher than those predicted by PMED.

Figures 20 and 21 plot predicted faulting from PMED and BCOA-ME, respectively, for Site 4. Faulting predictions were modest for both design procedures. The PMED faulting predictions did not exhibit any trends related to bond, joint spacing, or fiber content (and the bond conditions are plotted together in Figure 20), while BCOA-ME only predicted faulting for sites with 15 ft joint spacing.

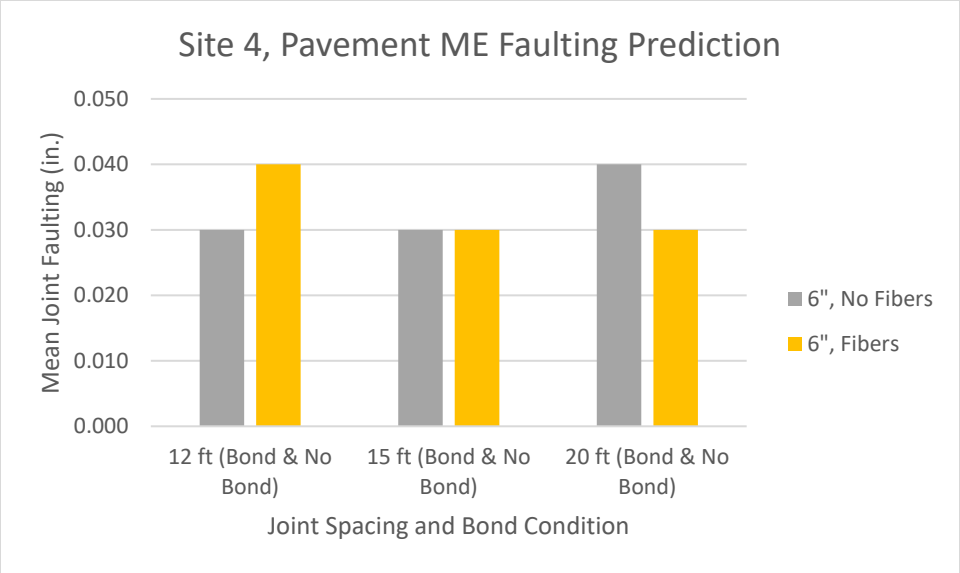

Figure 20. PMED predicted faulting at Site 4

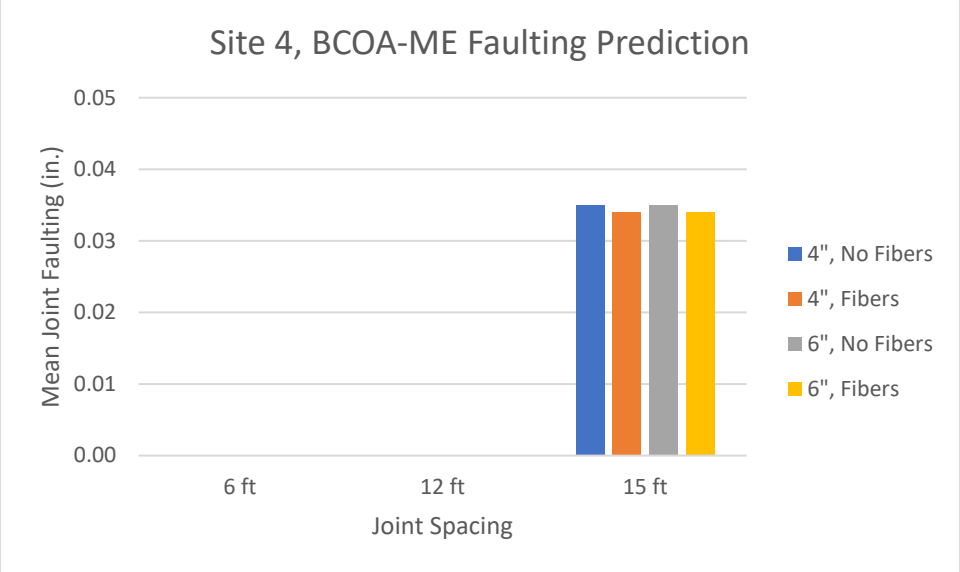

Figure 21. BCOA-ME predicted faulting at Site 4

3.1.3. Site 6

Figures 22 and 23 plot the predicted cracking values obtained from PMED and the UNOL design tool, respectively, for Site 6, sorted by joint spacing and fiber content. Like the results for Site 4, PMED predicted less than 5% slabs cracked for all test sites. PMED predicted increased cracking in sections without fibers and increased cracking with increasing joint spacing up to 20 ft. However, at 30 ft and 40 ft joint spacing, these trends in predicted cracking broke down. It is possible that PMED is not able to model overlays with these joint spacing values very well, as 30

ft and 40 ft transverse joint spacing designs are highly unusual in all types of jointed concrete pavements today and are not commonly considered by any design model.

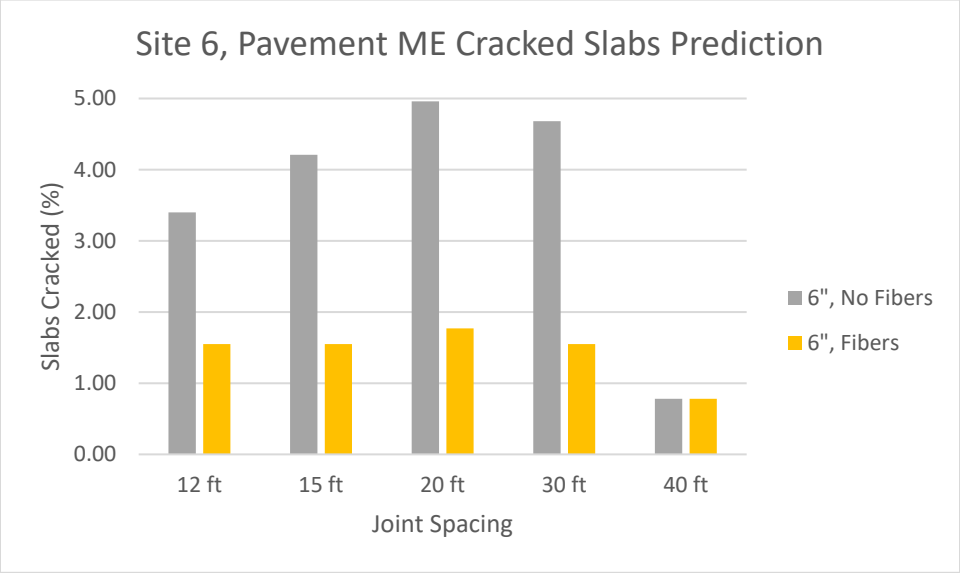

Figure 22. PMED predicted cracking at Site 6

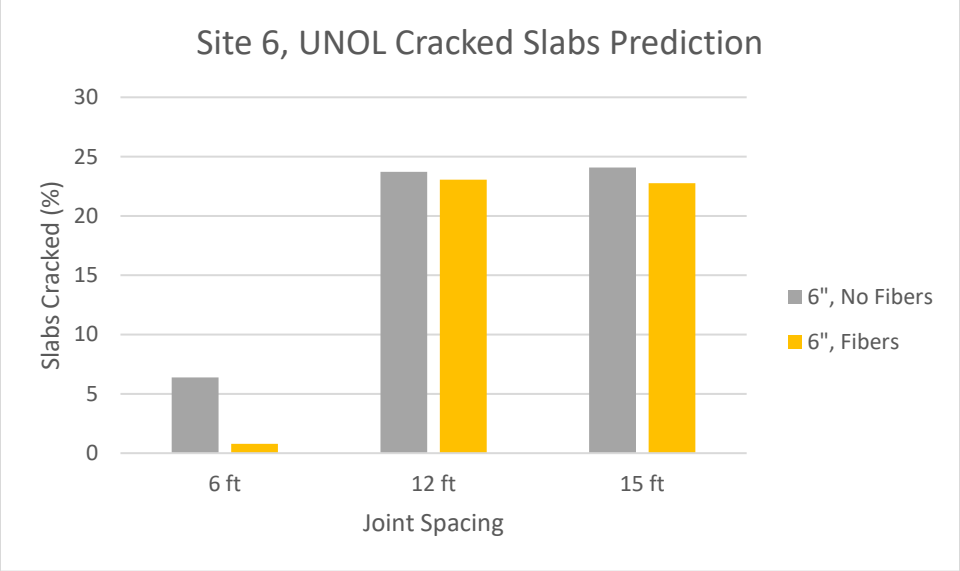

Figure 23. UNOL predicted cracking at Site 6

Meanwhile, like the results for Site 4, the alternative design tool (UNOL in this case) predicted much greater amounts of slab cracking for sections with longer joint spacings. UNOL cracking predictions ranged from 22.8% to 24.1% for all sections with 12 and 15 ft joint spacing, regardless of whether the sections were fiber reinforced.

Figures 24 and 25 plot the predicted mean joint faulting from PMED and the UNOL design tool, respectively, for Site 6, sorted by joint spacing and fiber content. PMED predicted more faulting at Site 6 than any other test site in this study, with predicted faulting increasing with joint spacing up to 20 ft. The UNOL design tool predicted very little faulting at all joint spacings. Fiber reinforcement had no bearing on faulting predictions by either model.

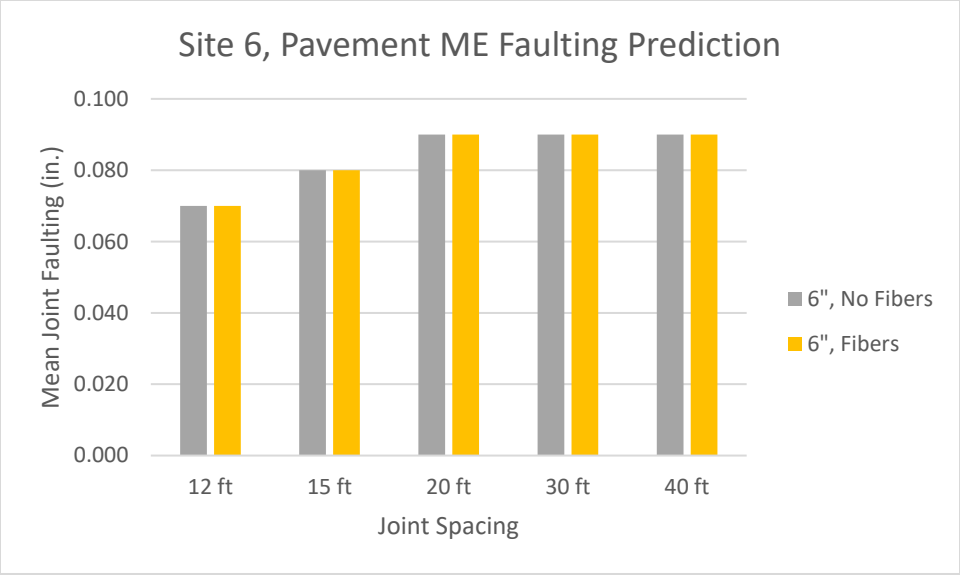

Figure 24. PMED predicted faulting at Site 6

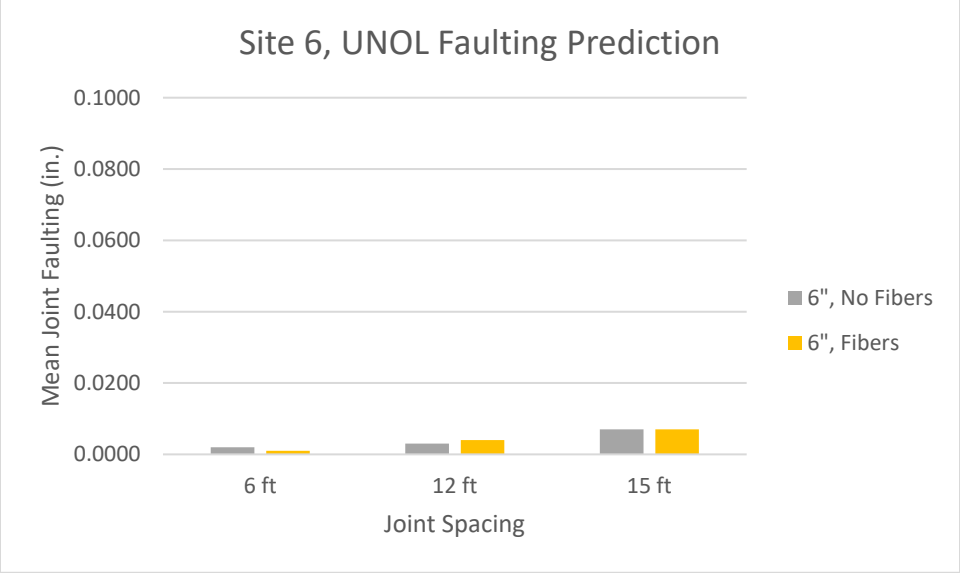

Figure 25. UNOL predicted faulting at Site 6

3.1.4. Site 7

Figures 26 and 27 plot the predicted cracking values obtained from PMED and BCOA-ME, respectively, for Site 7, sorted by joint spacing and fiber content. Unlike the predicted cracking values at Sites 4 and 6, the PMED and BCOA-ME models were in relatively close agreement for Site 7, with less than 5% slabs cracked for each design run using both design tools. Both design tools predicted increased cracking with increased joint spacing. PMED also predicted greater cracking values when assuming no bond between the concrete and asphalt.

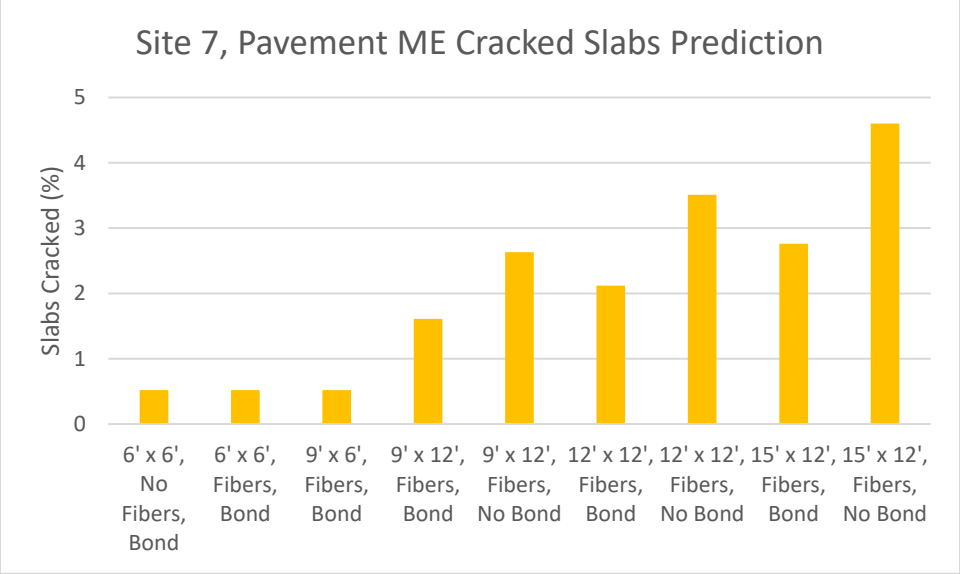

Figure 26. PMED predicted cracking at Site 7

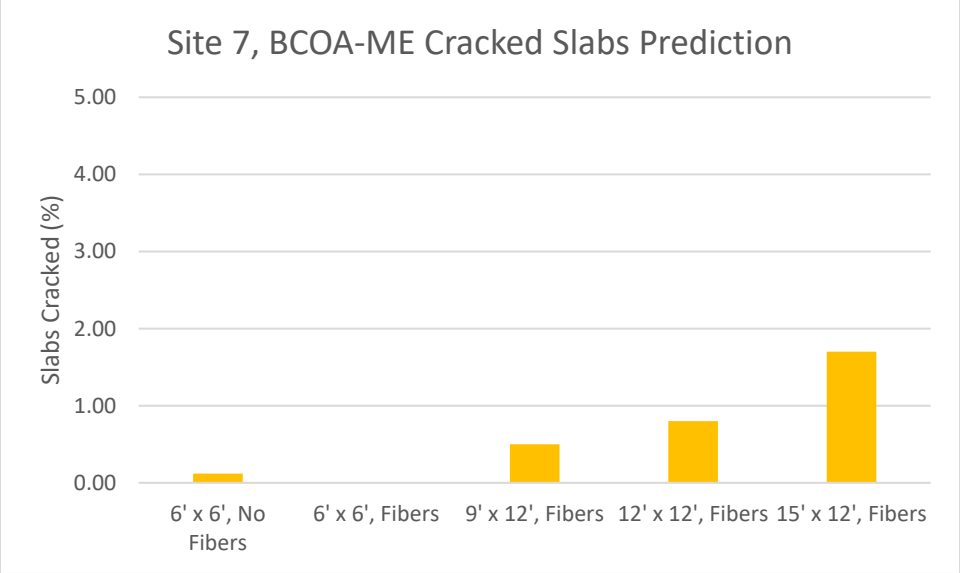

Figure 27. PMED predicted cracking at Site 7

Figures 28 and 29 plot the predicted faulting values obtained from PMED and BCOA-ME, respectively, for Site 7, sorted by joint spacing and fiber content. Faulting predictions from PMED were not sensitive to joint spacing or bond condition. (Both bond conditions are plotted together in Figure 29.) BCOA-ME only predicted faulting in the section with 15 ft joint spacing, but the predicted mean faulting value (0.11 in.) was modest for a 40-year design.

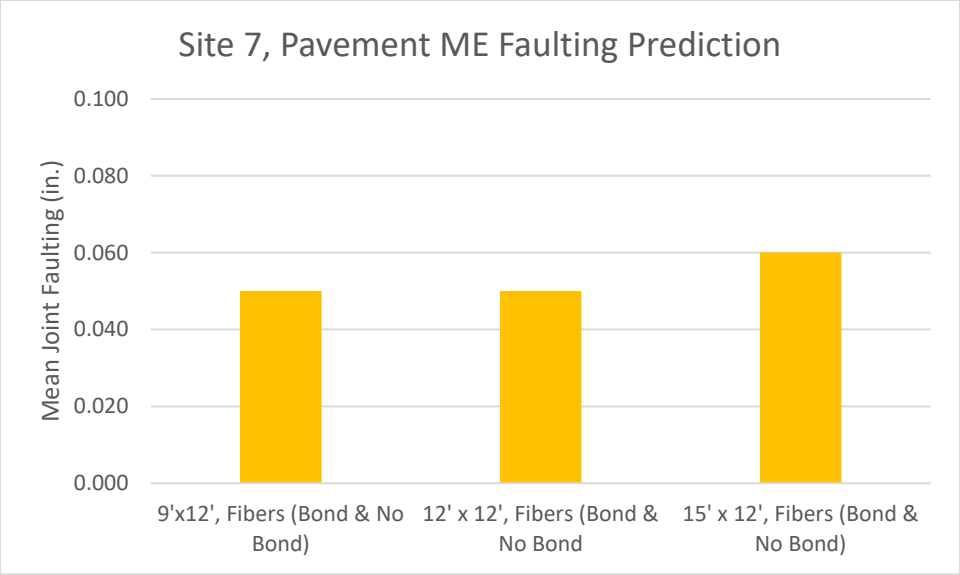

Figure 28. PMED predicted faulting at Site 7

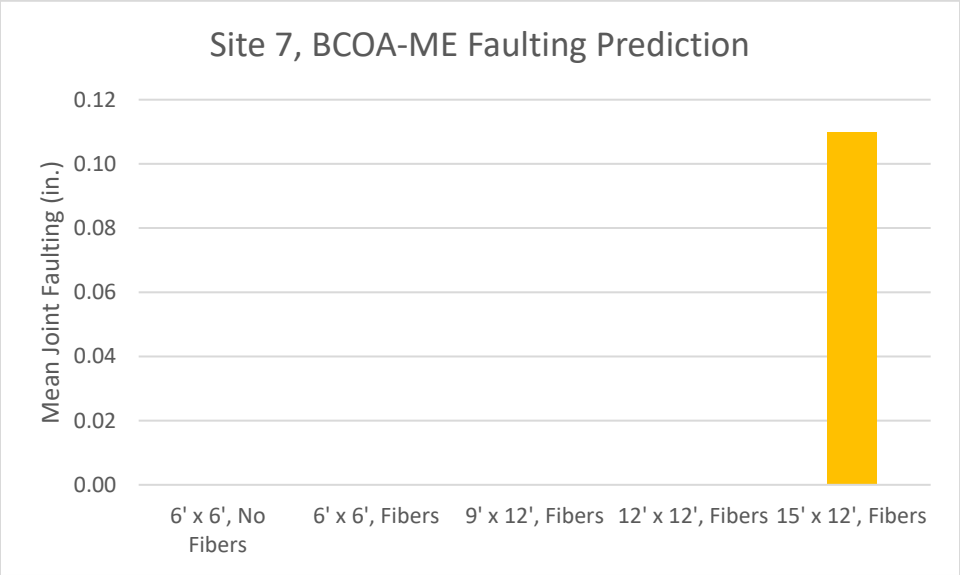

Figure 29. BCOA-ME predicted faulting at Site 7

3.2. Visual Distress Surveys

This section presents the results of the visual distress surveys conducted at each site. These results focused on distresses at Sites 4 and 6, as no distresses were observed in the areas under investigation at Sites 1, 2, 5, or 7.

3.2.1. Site 4

Three distresses were observed at Site 4: transverse cracking, corner cracking, and longitudinal cracking. All of the cracking at Site 4 was classified as low severity according to FHWA's Long-Term Pavement Performance (LTPP) Distress Identification Manual (Miller and Bellinger 2014). Figures 30 and 31 show the transverse and corner cracking results at Site 4, organized by thickness, joint spacing, and whether or not the mix contained fibers. Figures 32(a) and 32(b) show typical examples of transverse and longitudinal cracking observed at Site 4.

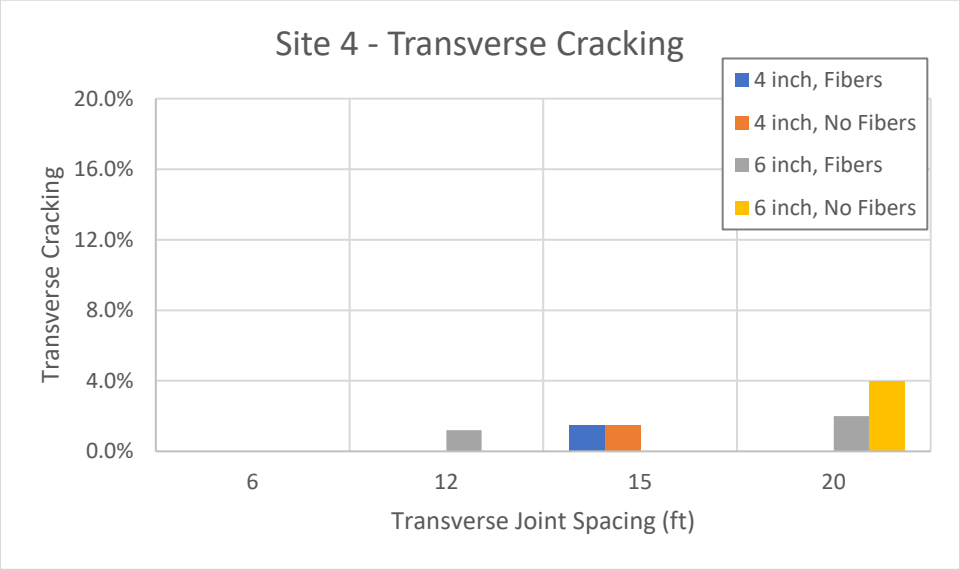

Figure 30. Transverse cracking observed at Site 4

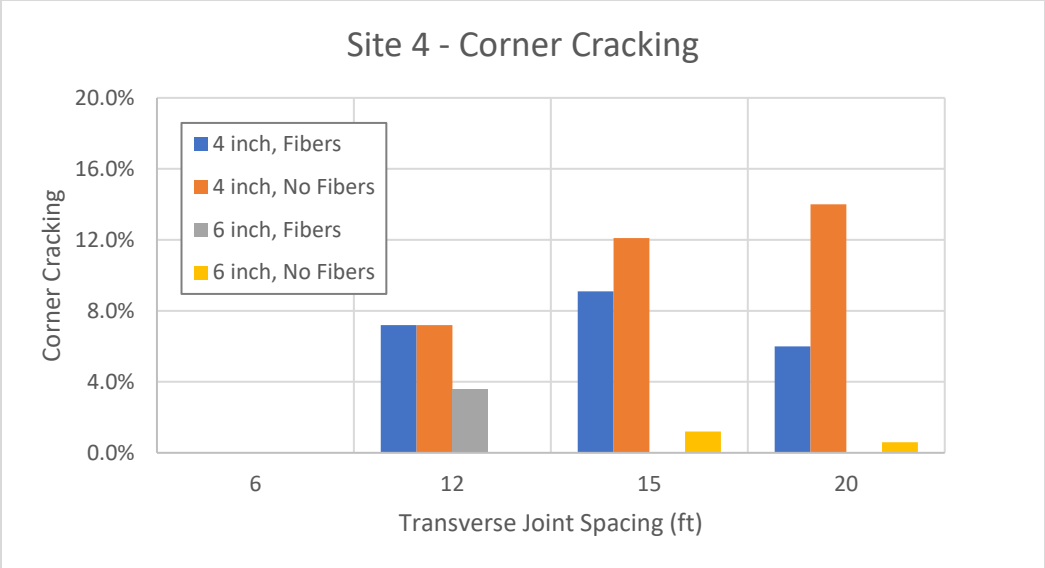

Figure 31. Corner cracking observed at Site 4

(a) (b)

Figure 32. Typical (a) corner and (b) transverse cracking observed at Site 4

Figure 33 shows longitudinal cracking results at Site 4, organized by joint spacing, thickness, and whether or not the mix contained fibers. Note that this longitudinal cracking appeared to be reflective cracking that resulted from longitudinal cracks in the underlying pavement. Figure 34(a) shows the existing asphalt surface prior to overlay, with longitudinal cracks that were prevalent throughout the project. Figure 34(b) shows a typical example of longitudinal cracking in the concrete overlay.

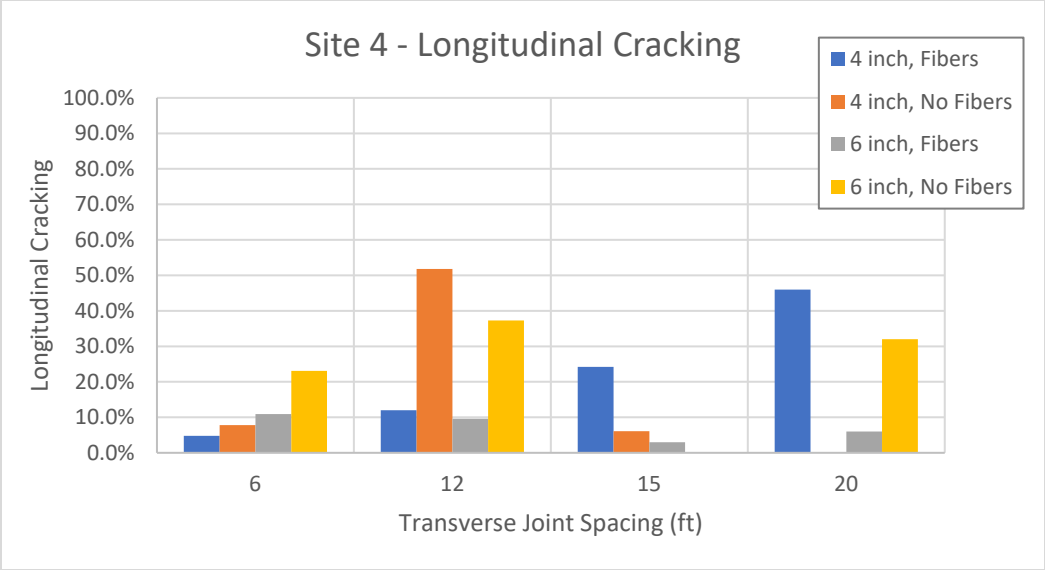

Figure 33. Longitudinal cracking observed at Site 4

(a) (b)

Figure 34. Longitudinal cracking at Site 4 (a) prior to overlay and (b) post-overlay

As demonstrated in Figures 34(a) and 34(b), the pattern of longitudinal cracking that developed in the overlay was very similar to that of the existing asphalt surface prior to overlay. The cracking appeared within one year of construction and did not appear to result from traffic loads. Notably, as of 2023, the longitudinal reflective cracking in the sections with fibers has held together more tightly than in the sections without fibers. The Mitchell County secondary roads department has filled the cracks in the sections without fibers, as pictured in Figure 34(b), but has left them unsealed to date in the sections containing fibers.

3.2.2. Site 6

Few distresses were observed at Site 6, except for transverse cracking in the sections with 30 ft and 40 ft transverse joint spacing that did not contain fibers. These transverse cracks appeared in

the middle of nearly every slab in Sections 6F and 6G, as plotted in Figure 35, and were classified as medium severity according to the FHWA LTPP Distress Identification Manual. Figure 36 shows a typical example of one of these mid-panel transverse cracks, which was also beginning to exhibit some spalling. Figures 37 and 38 plot the observed corner and longitudinal cracking, respectively, which were also generally more likely to occur at longer joint spacing designs.

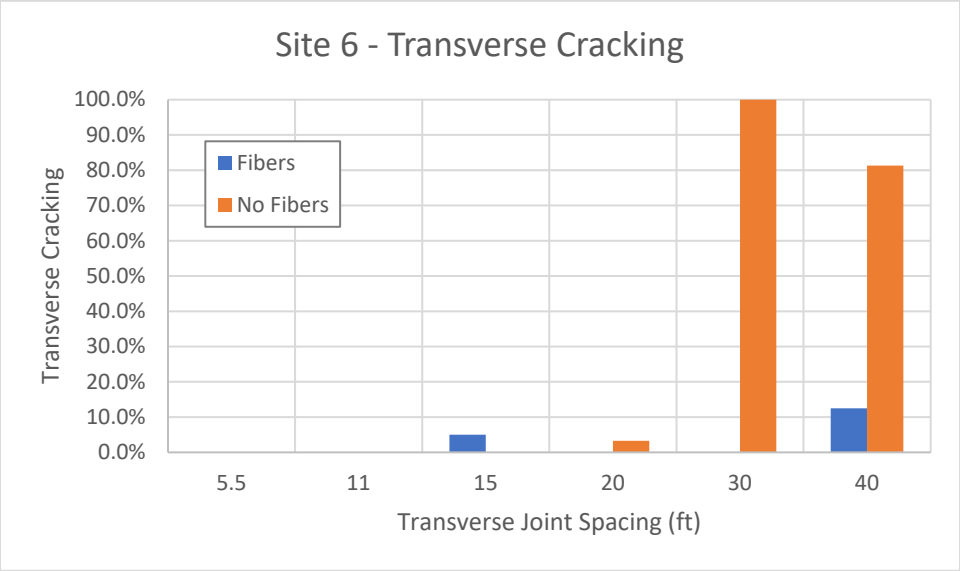

Figure 35. Transverse cracking observed at Site 6

Figure 36. Typical mid-panel transverse crack observed at Site 6

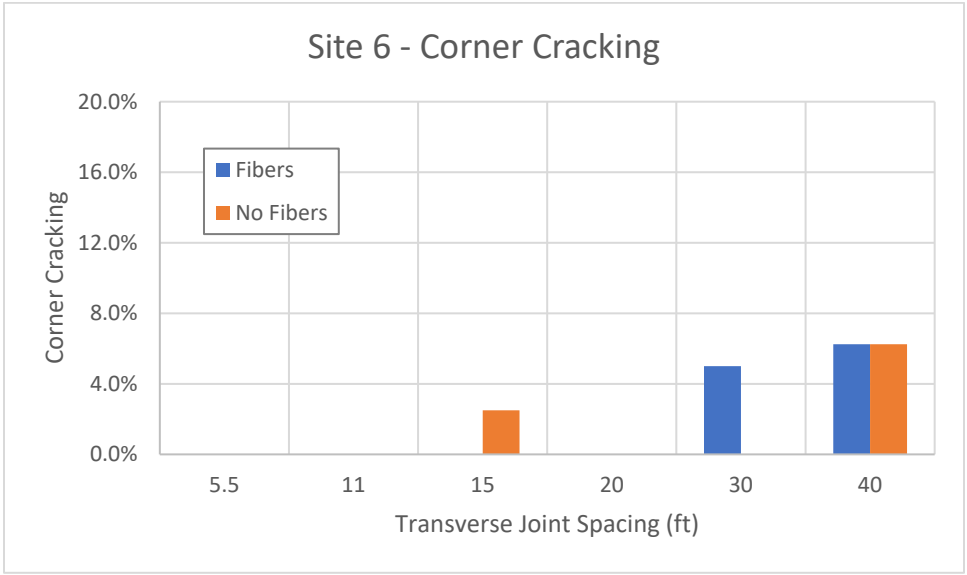

Figure 37. Corner cracking observed at Site 6

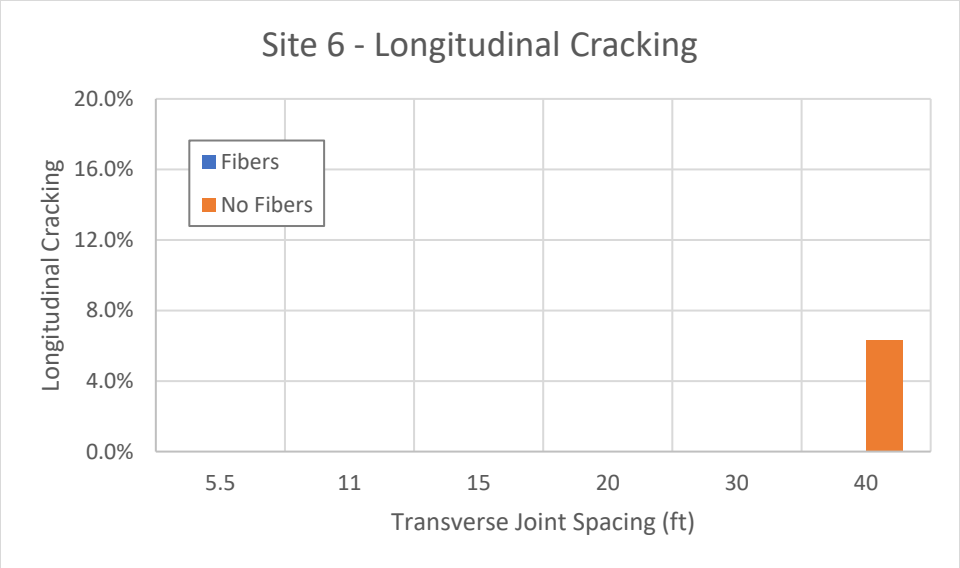

Figure 38. Longitudinal cracking observed at Site 6

One final notable aspect of Site 6 was that nearly the entire area of investigation was diamond ground to correct smoothness after construction. A high percentage (and often 100%) of every individual section was diamond ground, except for Sites 6F and 6G. Table 8 shows the percentage of slabs diamond ground for each section at Site 6.

Table 8. Percentage of slabs diamond ground at Site 6

Section	Thickness (in.)	Joint Spacing (ft)	Fibers	Diamond Grinding
6A	6	11	No	100.0%
6B	6	5.5	Yes	100.0%
6C	6	11	Yes	100.0%
6D	6	15	Yes	100.0%
6E	6	20	Yes	66.7%
6F	6	30	Yes	0.0%
6G	6	40	Yes	0.0%
6H	6	40	No	100.0%
6I	6	30	No	100.0%
6J	6	20	No	100.0%
6K	6	15	No	76.2%
6L	6	5.5	No	57.1%

3.2.3. Additional Notes

While no distresses were observed in the area of investigation at Site 2, there were limited areas of the roadway outside of the area of investigation with longitudinal cracking. This cracking appeared to result from longitudinal cracks in the underlying pavement, similar to Site 4. The total number of slabs with longitudinal cracking throughout the entire 7 mi roadway at Site 2 was

estimated at less than 2%. Additionally, while no distresses were observed throughout Site 7, approximately 15% of the slabs in Site 7F had been diamond ground to correct smoothness after construction.

3.3. Ultrasonic Tomography for Joint Activation

Table 9 contains the observed rates of joint activation measured by the MIRA method at each test site. Sites 1 and 2 were the only two sections in the study that had a joint spacing of 12 ft by 12 ft with less than 100% joint activation. All transverse joints were activated in every other section with a transverse joint spacing of 12 ft or greater. Sections with 5.5 or 6 ft transverse joint spacings had joint activation rates ranging from 50% to 80%. The two sections with 9 ft transverse joint spacing, Sites 7E and 7F, achieved 100% transverse joint activation.

Table 9. Observed joint activation rates at each test site

Section	Overlay Type	Thickness (in.)	Joint Spacing (Transverse x Longitudinal), (ft x ft)	Fibers	Activation Rate (%)
1	COA-U	6	12 x 12	Yes	40
2	COA-U	6	12 x 12	Yes	60
4A	COA-B	4	6 x 6	No	50
4B	COA-B	4	12 x 12	No	100
4C	COA-B	4	15 x 12	No	100
4D	COA-B	4	20 x 12	No	100
4E	COA-B	4	20 x 12	Yes	100
4F	COA-B	4	15 x 12	Yes	100
4G	COA-B	4	12 x 12	Yes	100
4H	COA-B	4	6 x 6	Yes	40
4I	COA-U	6	6 x 6	Yes	50
4J	COA-U	6	12 x 12	Yes	100
4K	COA-U	6	15 x 12	Yes	100
4L	COA-U	6	20 x 12	Yes	100
4M	COA-U	6	20 x 12	No	100
4N	COA-U	6	15 x 12	No	100
4O	COA-U	6	12 x 12	No	100
4P	COA-U	6	6 x 6	No	70
5	COA-U	6	12 x 12	Yes	100
6A	COC-U	6	12 x 11	No	100
6B	COC-U	6	5.5 x 5.5	Yes	80
6C	COC-U	6	12 x 11	Yes	100
6D	COC-U	6	15 x 11	Yes	100
6E	COC-U	6	20 x 11	Yes	100
6F	COC-U	6	30 x 11	Yes	100
6G	COC-U	6	40 x 11	Yes	100
6H	COC-U	6	40 x 11	No	100
6I	COC-U	6	30 x 11	No	100
6J	COC-U	6	20 x 11	No	100
6K	COC-U	6	15 x 11	No	100
6L	COC-U	6	5.5 x 5.5	No	70
7A	COA-U	6	6 x 6	No	60
7B	COA-U	6	15 x 12	Yes	100
7C	COA-U	6	12 x 12	Yes	100
7D	COA-U	6	9 x 12	Yes	100
7E	COA-U	6	9 x 6	Yes	100
7F	COA-U	6	6 x 6	Yes	70

3.4. Falling Weight Deflectometer for Load Transfer Efficiency

3.4.1. Site 1

Table 10 lists the results of FWD testing for load transfer at Site 1, including the average deflection in the loaded slab (d_l) and the average joint LTE calculated at all 10 transverse joints. Figure 39 plots the LTE results on a slab-by-slab basis. Average joint LTE at Site 1 was classified as good according to Table 6, though some variation was observed between slabs, with differences as great as 16% between adjacent joints.

Table 10. Joint LTE results for Site 1

Test Date	Air Temp (°F)	Thickness (in.)	Transverse Joint Spacing (ft)	Fibers	d_l (mils)	Average Joint LTE (%)
10/23/2023	56	6	12	Yes	4.58	82.9

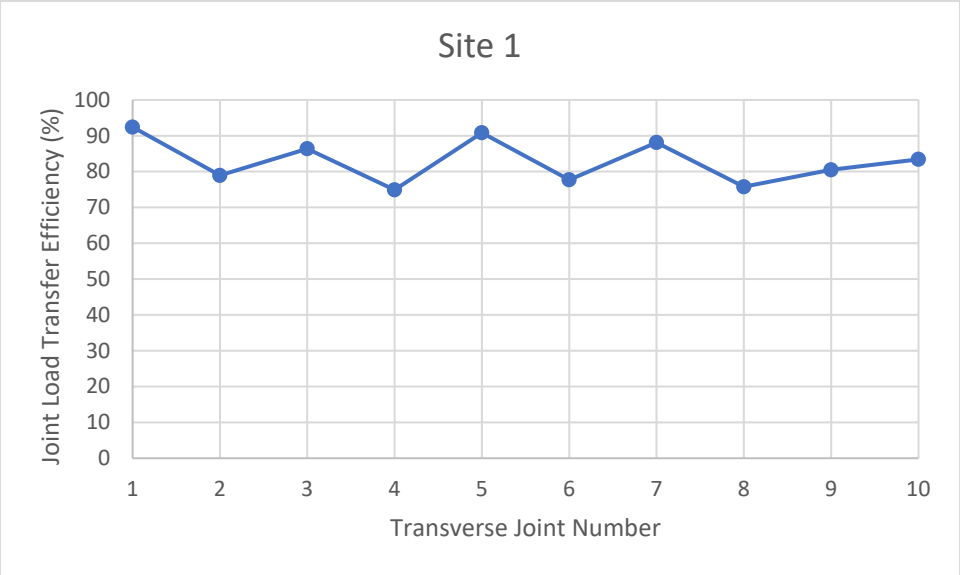

Figure 39. Joint-by-joint joint LTE results for Site 1

3.4.2. Site 2

Table 11 lists the results of FWD testing for joint LTE at Site 2, including the average deflection in the loaded slab and the average LTE calculated at all 10 transverse joints. Figure 40 plots the LTE results on a slab-by-slab basis. Average joint LTE at Site 2 was classified as poor according to Table 6. Besides a spike in joint LTE at the seventh transverse joint in Figure 40, joint LTE did not deviate by more than 10% between adjacent slabs.

Table 11. Joint LTE results for Site 2

Test Date	Air Temp (°F)	Separation Layer	Thickness (in.)	Transverse (ft)	Fibers	d_l (mils)	Average Joint LTE (%)
10/23/2023	57	Geotextile	6	12	Yes	13.5	47.8

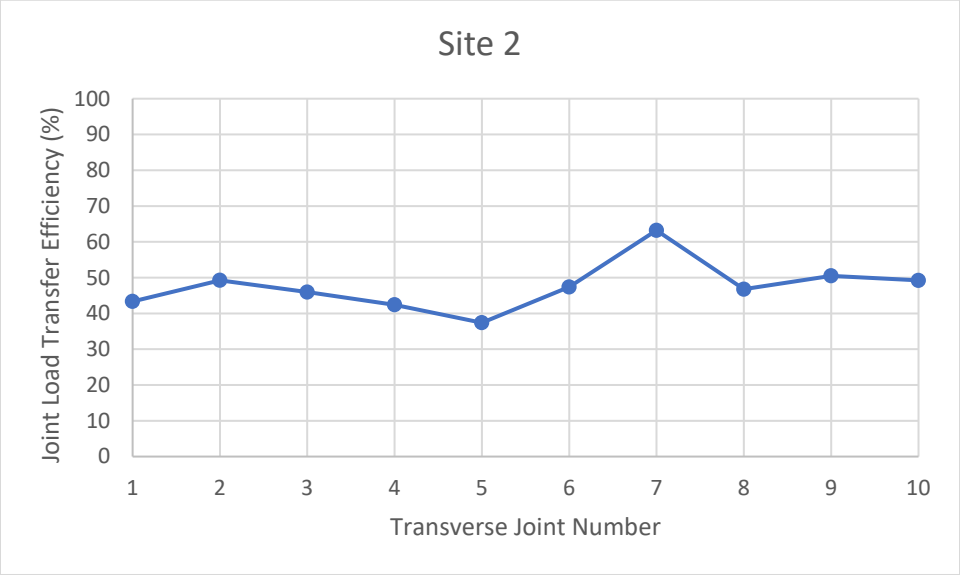

Figure 40. Joint-by-joint LTE results for Site 2

3.4.3. Site 4

Table 12 lists the average deflection and joint LTE values calculated for each of the 16 test sections at Site 4. Figure 41 summarizes the results at each section, organized by thickness, joint spacing, and fiber reinforcement.

Table 11. Joint LTE results for Site 4

Site	Test Date	Air Temp (°F)	Overlay Type	Thick-ness (in.)	Transverse Joint Spacing (ft)	Fibers	d_l (mils)	Average Joint LTE (%)
4A	10/23/2023	66	COA-B	4	6	No	5.62	90.5
4B	10/23/2023	65	COA-B	4	12	No	7.62	87.9
4C	10/23/2023	65	COA-B	4	15	No	6.47	87.0
4D	10/23/2023	66	COA-B	4	20	No	6.86	86.4
4E	10/24/2023	61	COA-B	4	20	Yes	8.13	88.6
4F	10/24/2023	62	COA-B	4	15	Yes	7.42	82.9
4G	10/24/2023	61	COA-B	4	12	Yes	6.80	85.2
4H	10/24/2023	63	COA-B	4	6	Yes	4.93	88.8
4I	10/24/2023	64	COA-U	6	6	Yes	3.92	91.3
4J	10/24/2023	65	COA-U	6	12	Yes	4.69	82.6
4K	10/24/2023	64	COA-U	6	15	Yes	5.21	83.7
4L	10/24/2023	64	COA-U	6	20	Yes	5.66	83.5
4M	10/24/2023	66	COA-U	6	20	No	6.40	84.0
4N	10/24/2023	65	COA-U	6	15	No	5.58	86.8
4O	10/24/2023	65	COA-U	6	12	No	5.96	88.0
4P	10/24/2023	65	COA-U	6	6	No	5.37	92.1

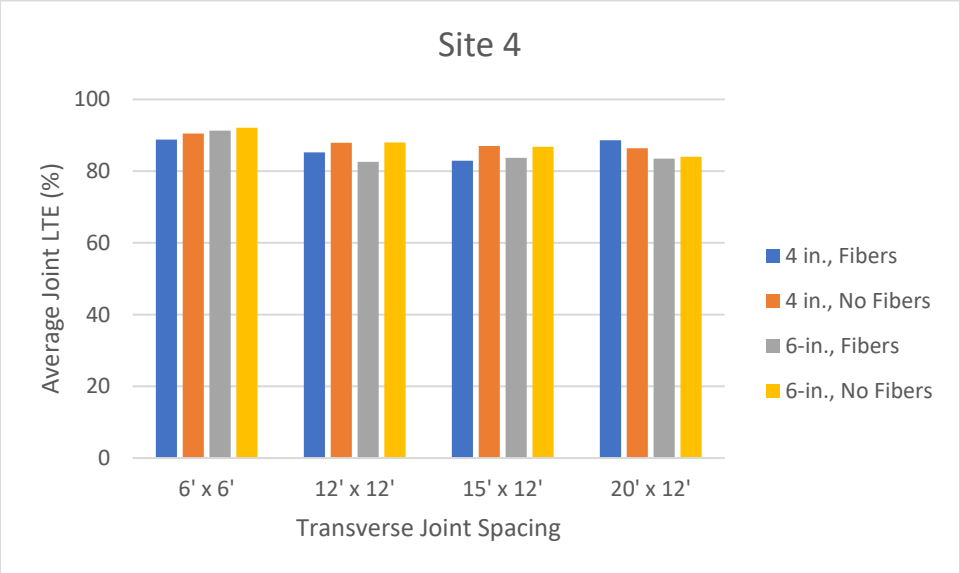

Figure 41. Summary of joint LTE results for Site 4

Each of the individual sections in Site 4 demonstrated consistently high joint LTE values, ranging from good to excellent according to Table 6, without any major jumps or dips between joints. Figure 42 presents the joint-by-joint LTE data for Site 4A, which was typical of all of the Site 4 sections. Appendix B contains figures corresponding to each of the other Site 4 sections.

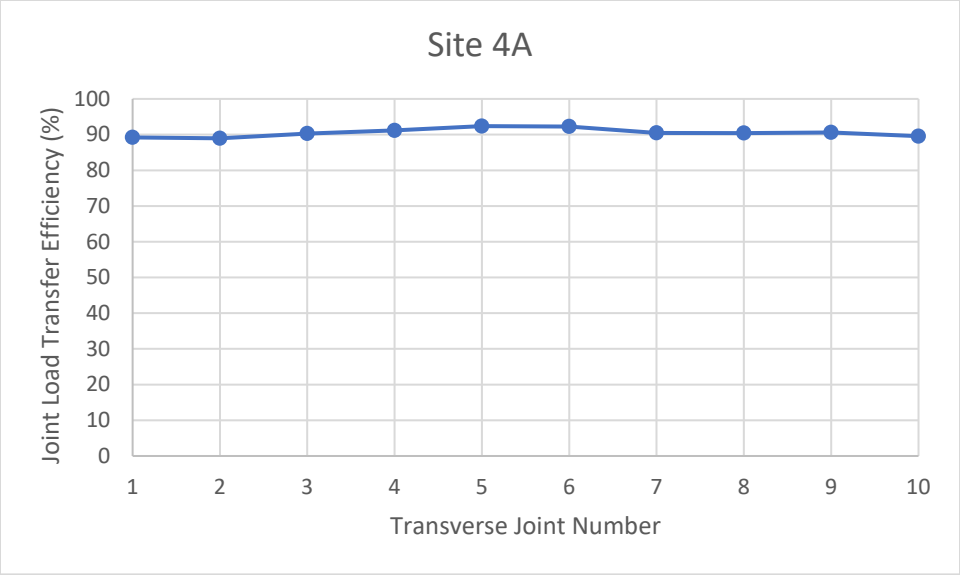

Figure 42. Joint-by-joint LTE results for Site 4A

3.4.4. Site 5

Table 13 lists the results of FWD testing for joint LTE at Site 5, including the average deflection in the loaded slab and the average LTE calculated at all 10 transverse joints. Figure 43 plots the LTE results on a slab-by-slab basis. Average joint LTE at Site 5 was classified as good according to Table 6. LTE results were consistent from slab to slab, with two dips of about 15% to 18% at Slabs 3 and 8 observed in Figure 43.

Table 12. Joint LTE results for Site 5

Test Date	Air Temp (°F)	Thickness (in.)	Transverse Joint Spacing (ft)	Fibers	d_l (mils)	Average Joint LTE (%)
10/23/2023	60	6	12	Yes	5.11	85.3

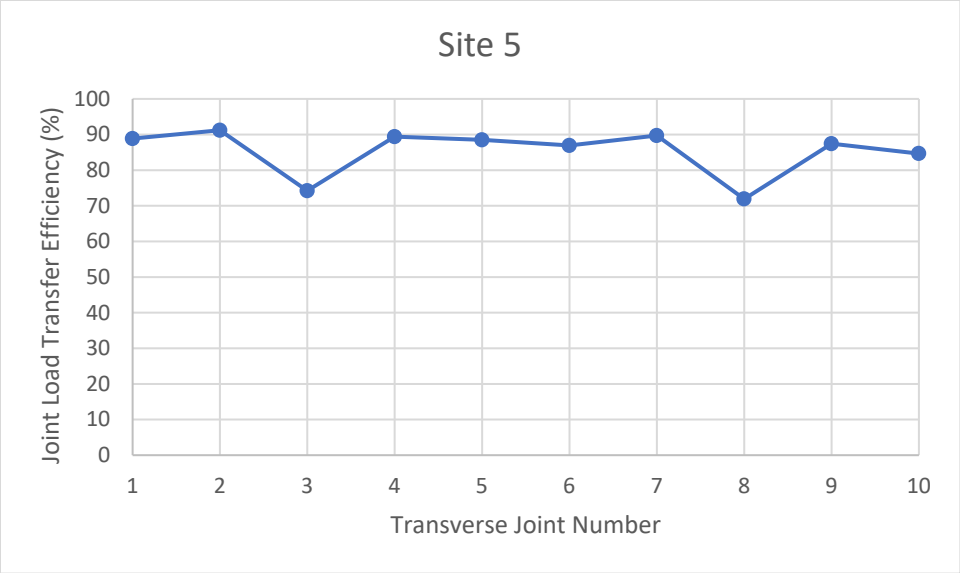

Figure 43. Joint-by-joint LTE results for Site 5

3.4.5. Site 6

Table 14 lists the average deflection and joint LTE values calculated for each of the 12 test sections at Site 6. Figure 44 summarizes the results at each section, organized by joint spacing and fiber reinforcement.

Table 13. Joint LTE results for Site 6

Site	Test Date	Air Temp (°F)	Separation Layer	Thick-ness (in.)	Transverse Joint Spacing (ft)	Fibers	d_l (mils)	Average Joint LTE (%)
6A	11/8/2023	54	Geotextile	6	11	No	9.93	41.7
6B	11/8/2023	54	Geotextile	6	5.5	Yes	11.0	66.0
6C	11/8/2023	53	Geotextile	6	11	Yes	11.0	47.1
6D	11/8/2023	55	Geotextile	6	15	Yes	16.2	44.2
6E	11/8/2023	53	Geotextile	6	20	Yes	12.9	51.1
6F	11/8/2023	54	Geotextile	6	30	Yes	14.9	37.1
6G	11/8/2023	53	Geotextile	6	40	Yes	14.8	31.7
6H	11/8/2023	54	Geotextile	6	40	No	17.8	36.6
6I	11/8/2023	55	Geotextile	6	30	No	11.3	43.8
6J	11/8/2023	54	Geotextile	6	20	No	14.1	35.8
6K	11/8/2023	54	Geotextile	6	11	No	16.8	35.1
6L	11/8/2023	55	Geotextile	6	5.5	No	10.6	65.2

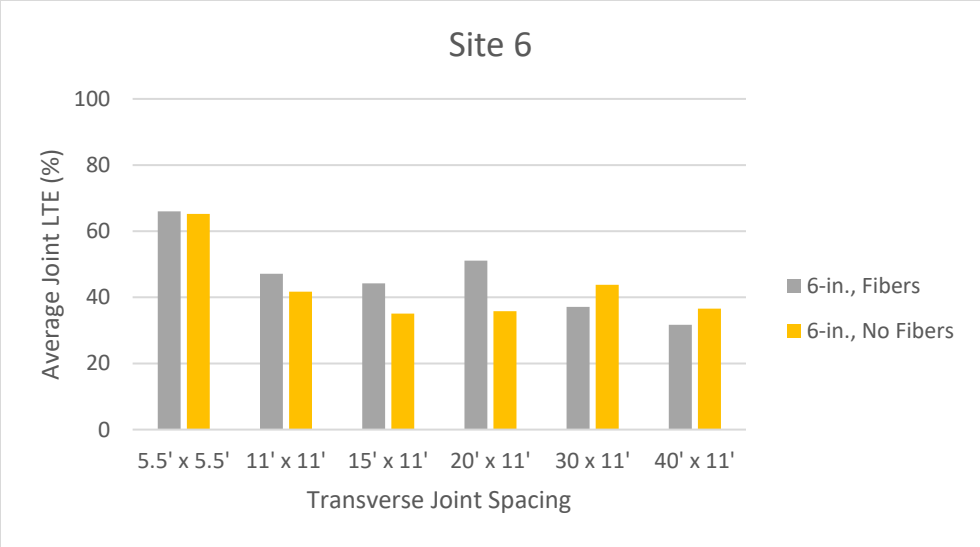

Figure 44. Summary of joint LTE results for Site 6

At Site 6, average joint LTE for the sections with shorter joint spacing (5.5 ft x 5.5 ft) were classified as fair according to Table 6, while all other sections were classified as poor. A variety of slab-by-slab LTE patterns were observed within individual sections at Site 6. Figures 45 and 46 plot the joint-by-joint LTE results for Site 6B and Site 6L, respectively, which were the two sections with 5.5 ft x 5.5 ft joint spacing. These sections demonstrated significant variation in joint LTE between adjacent slabs, with many instances of joint LTE measuring between 80% to 90% (good to excellent) in one slab followed by 30% to 50% (poor) in the adjacent slab.

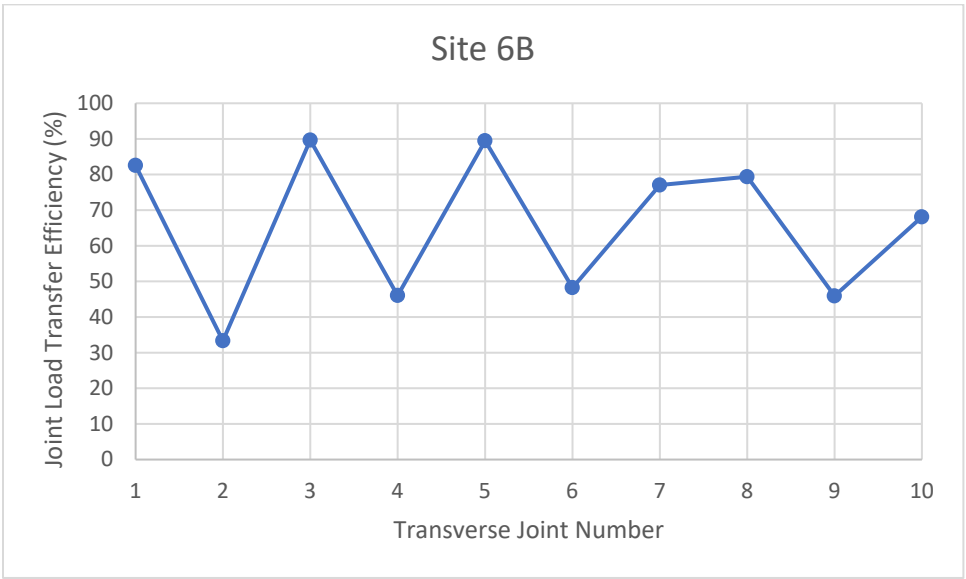

Figure 45. Joint-by-joint LTE results for Site 6B

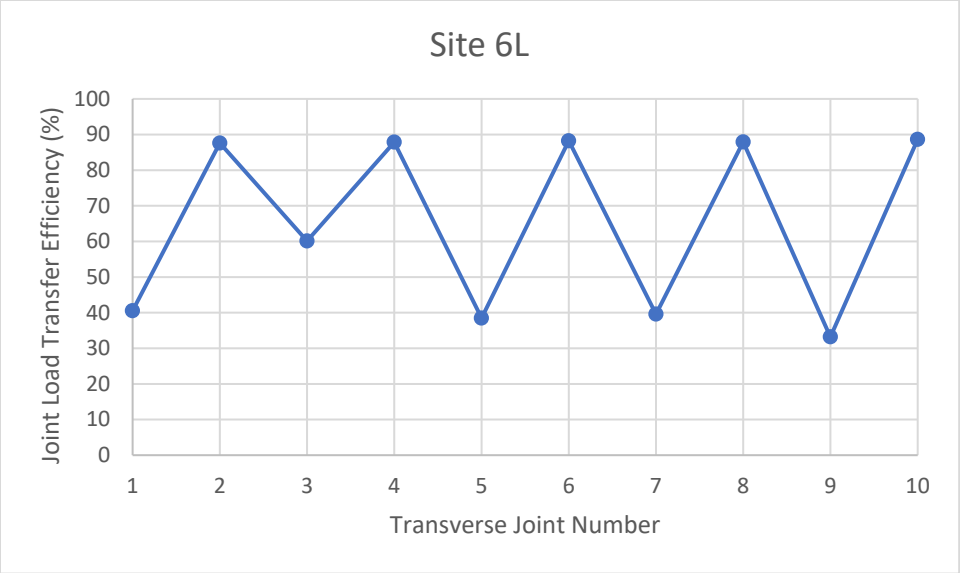

Figure 46. Joint-by-joint LTE results for Site 6L

For the most part, the other sections at Site 6 demonstrated consistently low joint LTE values. Figures 47 and 48 plot slab-by-slab results for Site 6C (12 ft joint spacing, containing fibers) and Site 6D (15 ft joint spacing, containing fibers), which show typical results at Site 6. In these sections, LTE values at adjacent joints generally remained within 10% of each other but occasionally demonstrated bumps and dips in the range of 20% to 30%. Figure 49 plots one of the more unusual joint-by-joint LTE results observed in this study at Site 6F (30 ft joint spacing, containing fibers). LTE values at Site 6F varied between 14.8% and 70.2%, although the pattern was not consistently up and down between adjacent slabs as at Sites 6B and 6L (Figures 45 and 46). Appendix B contains figures corresponding to each of the other Site 6 sections.

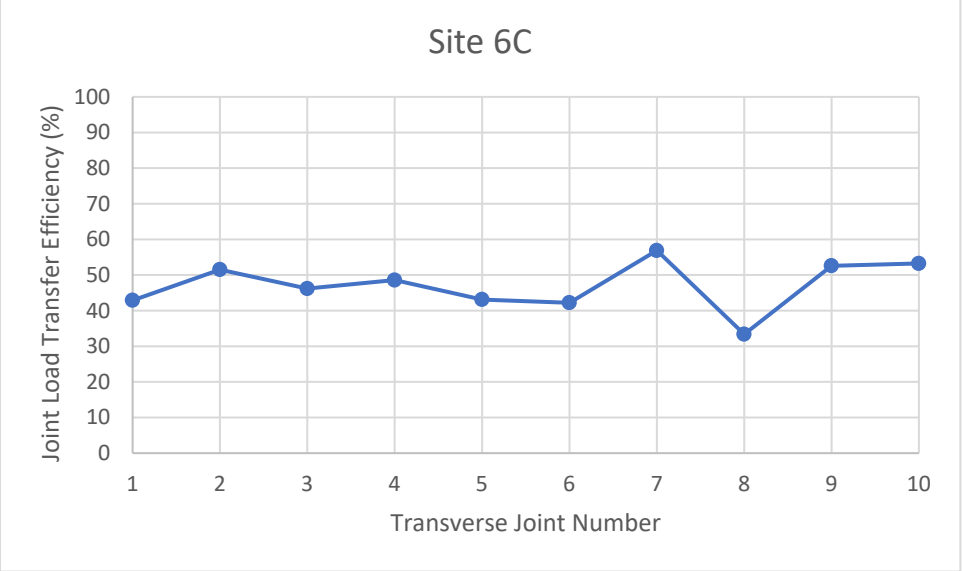

Figure 47. Joint-by-joint LTE results for Site 6C

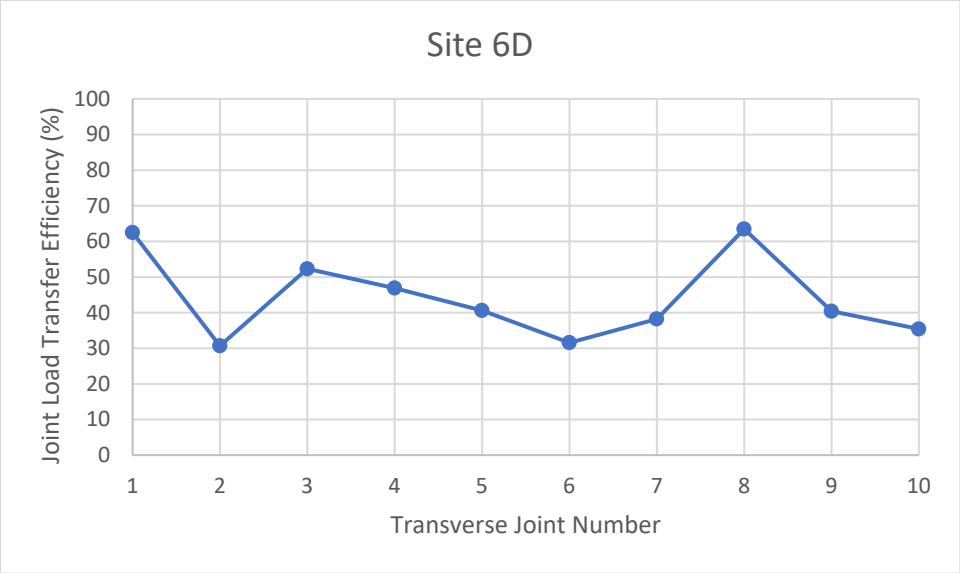

Figure 48. Joint-by-joint LTE results for Site 6D

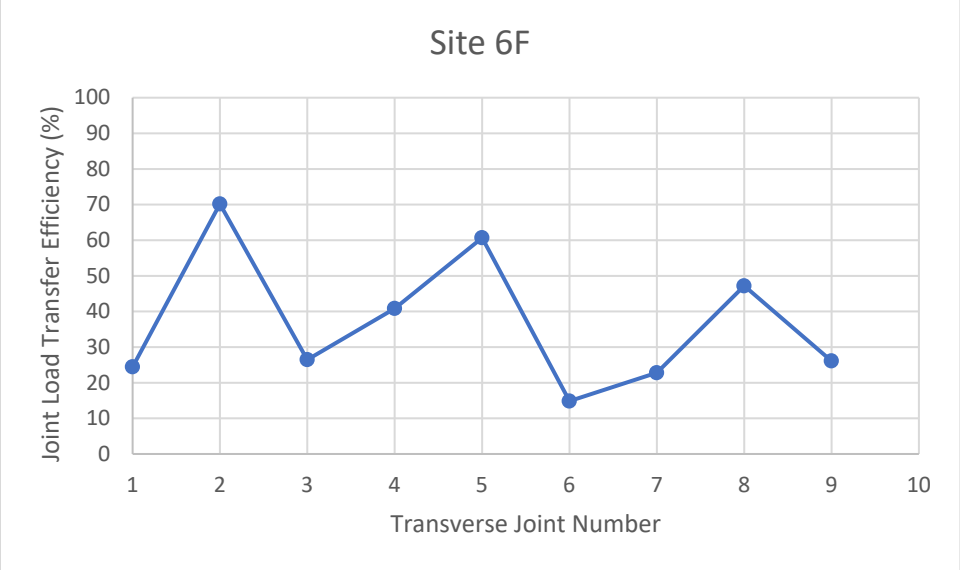

Figure 49. Joint-by-joint LTE results for Site 6F

3.4.6. Site 7

Table 15 lists the average joint LTE values calculated for each of the 12 test sections at Site 7. Figure 50 plots the results at each section, organized by joint spacing and fiber reinforcement. Figures 51 through 56 plot the joint-by-joint LTE results for each of the individual sections at Site 7. Overall, the average joint LTE measured at each of the Site 7 sections ranged from fair to good. The worst-performing section was Site 7B (15 ft transverse joint spacing, containing fibers), with an average joint LTE of 61.2%. As seen in Figure 52, Site 7B also demonstrated variation of 16% to 36% in joint LTE between adjacent slabs. Joint-by-joint results for the other

Site 7 sections indicated values generally close to the section values at most joints, with occasional dips in LTE at isolated slabs ranging from 20% to 60%.

Table 14. Joint LTE results for Site 7

Site	Test Date	Air Temp (°F)	Thickness (in.)	Transverse Joint Spacing (ft)	Fibers	d_l (mils)	Average Joint LTE (%)
7A	11/1/2023	45	6	6	No	3.03	88.4
7B	11/1/2023	44	6	15	Yes	6.90	61.2
7C	11/1/2023	44	6	12	Yes	6.45	77.8
7D	11/1/2023	45	6	9	Yes	6.77	77.4
7E	11/1/2023	47	6	9	Yes	5.10	86.9
7F	11/1/2023	47	6	6	Yes	3.86	87.6

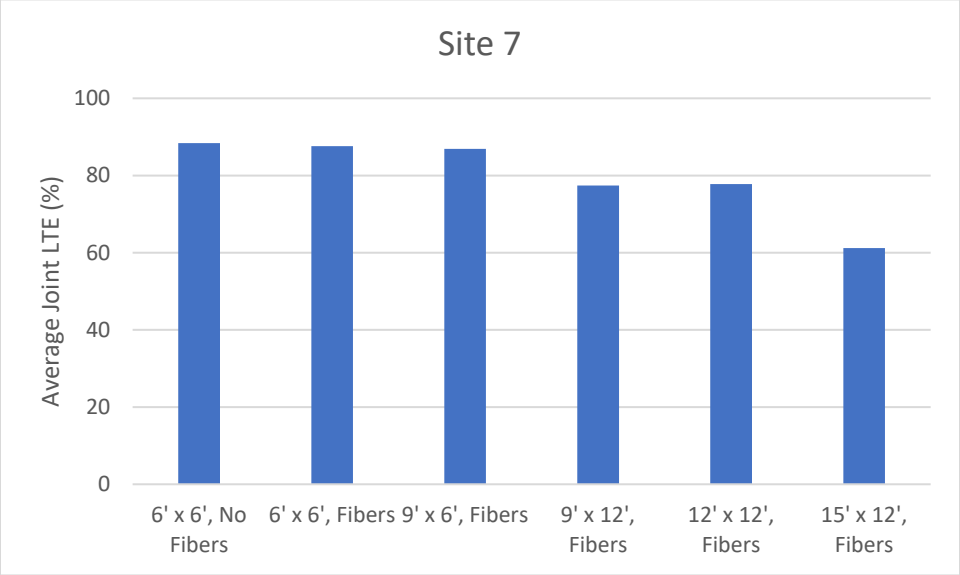

Figure 50. Summary of joint LTE results for Site 7

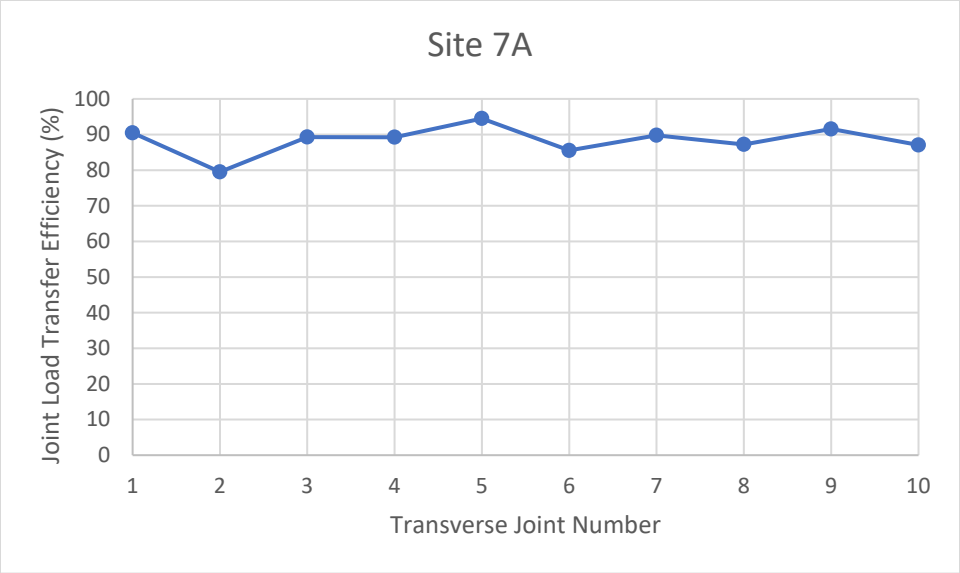

Figure 51. Joint-by-joint LTE results for Site 7A

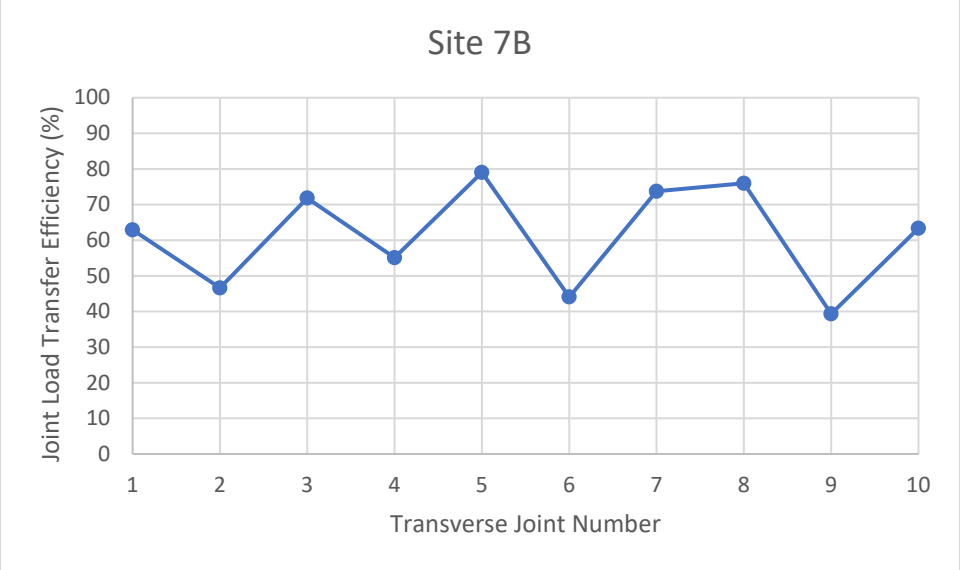

Figure 52. Joint-by-joint LTE results for Site 7B

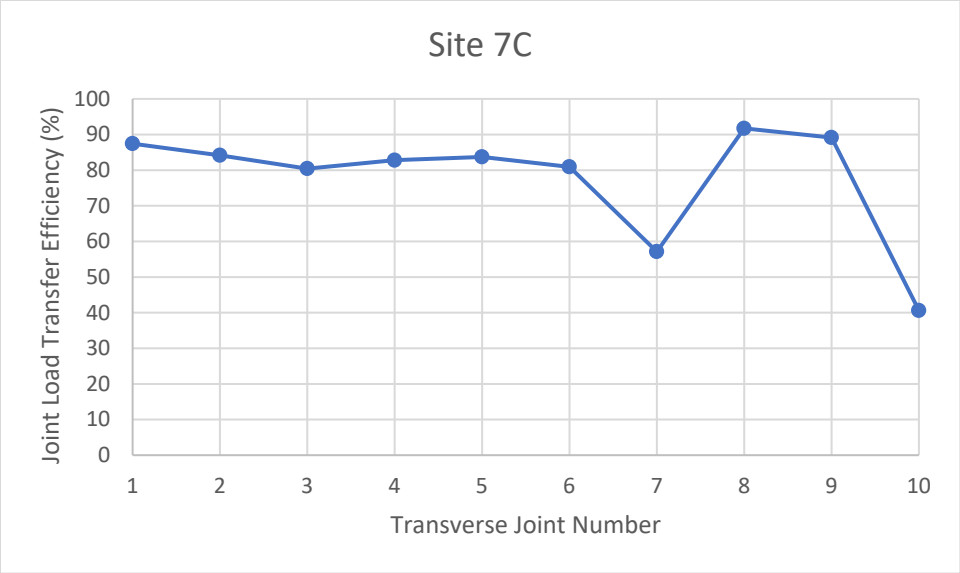

Figure 53. Joint-by-joint LTE results for Site 7C

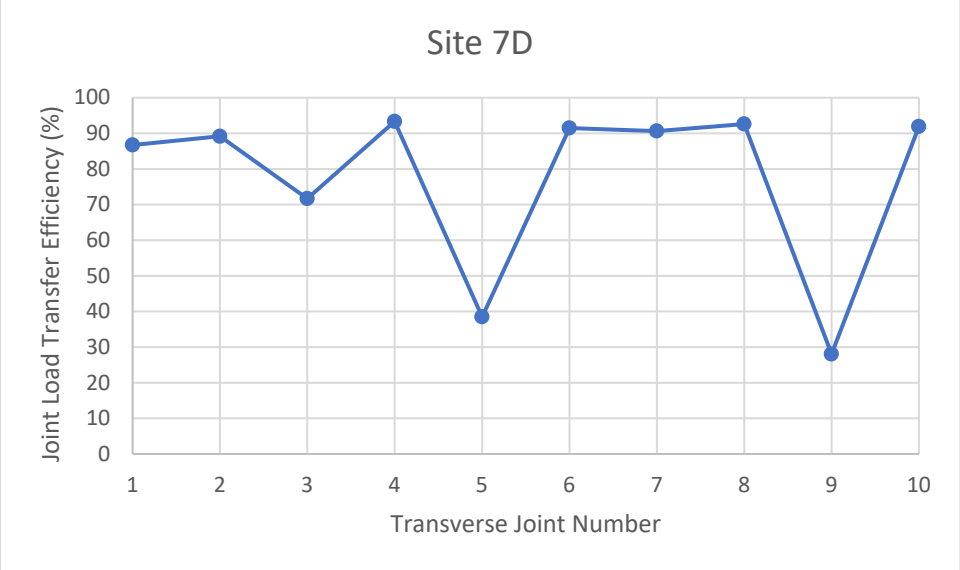

Figure 54. Joint-by-joint LTE results for Site 7D

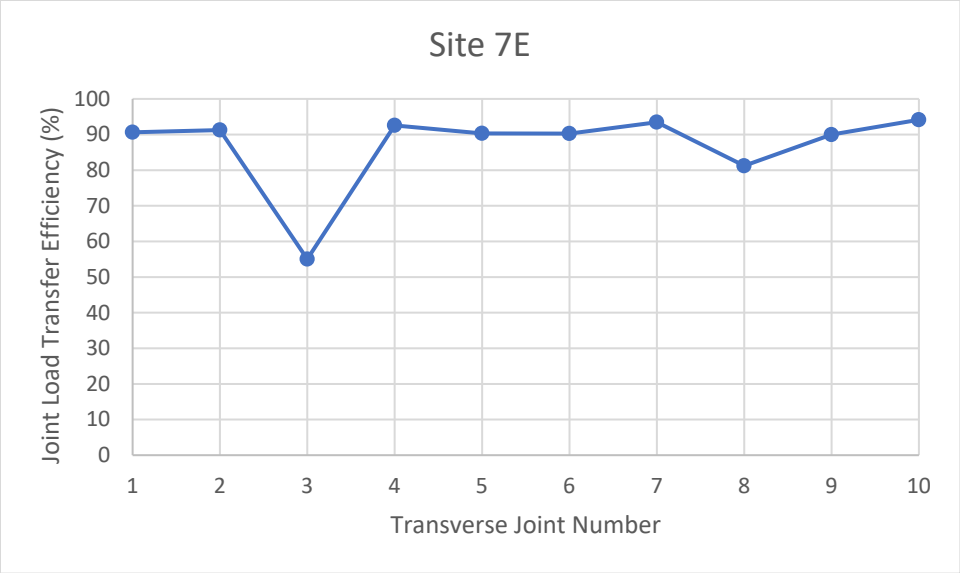

Figure 55. Joint-by-joint LTE results for Site 7E

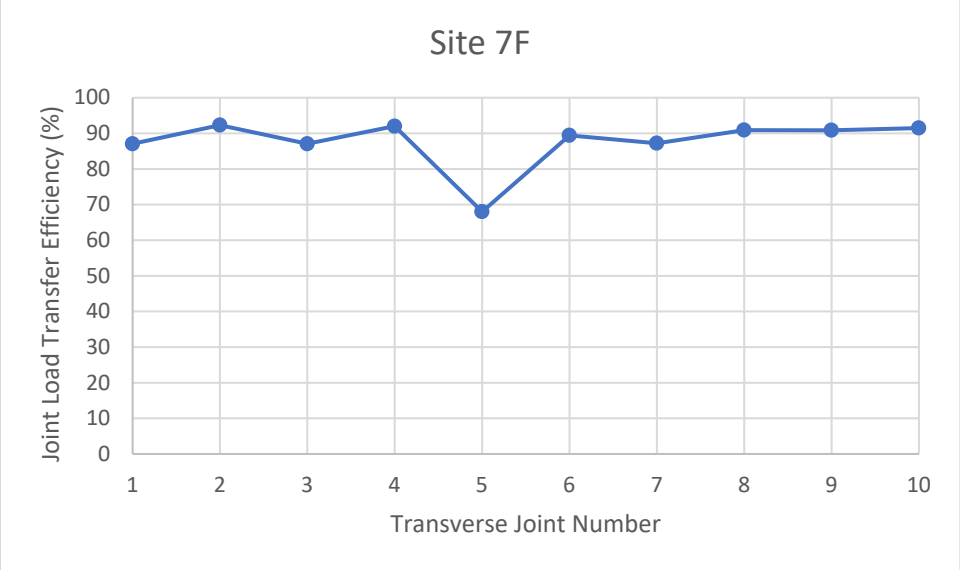

Figure 56. Joint-by-joint LTE results for Site 7F

3.5. Falling Weight Deflectometer for Structural Backcalculation

3.5.1. Site 1

Table 16 lists the results of FWD backcalculation for Site 1. The backcalculated effective thickness was 10.8 in., which was 4.8 in. greater than the overlay design thickness of 6 in. Given the magnitude of the difference between the design overlay thickness and effective thickness, the underlying layer appears to have contributed to the structural response of the overlay. The full

cross section of the underlying layer was a composite pavement consisting of 3 in. of HMA over an older 7 in. concrete pavement.

Table 15. FWD backcalculation results for Site 1

Test Date	Air Temp (°F)	Overlay Type	h_{PCC} (in.)	Fibers	D_0 (mils)	ℓ (in.)	k (psi/in.)	h_{eff} (in.)
10/23/2023	56	COA-U	6	Yes	3.91	31.3	451	10.8

3.5.2. Site 2

Table 17 lists the results of the FWD backcalculation for Site 2. The backcalculated effective thickness was 7.76 in., which was 1.76 in. higher than the overlay design thickness. Site 2 provides an interesting contrast with Site 1, as the overlay thickness (6 in.) and underlying pavement (a composite pavement with 3 in. HMA over 7 in. PCC) were identical except for the presence of a geotextile separation layer between the concrete and asphalt layers at Site 2. The maximum deflection at Site 2 (7.92 mils) was more than twice the maximum deflection at Site 1 (3.91 mils). The effective thickness at Site 2 (7.76 in.) was much closer to the overlay design thickness than at Site 1 (10.8 in.), indicating that the underlying layer did not contribute as much to the structural response of the overlay. The backcalculated k-value at Site 2 (263 psi/in.) was also much lower than at Site 1 (451 psi/in.).

Table 16. FWD backcalculation results for Site 2

Test Date	Air Temp (°F)	Overlay Type	Sep. Layer	h_{PCC} (in.)	Fibers	D_0 (mils)	ℓ (in.)	k (psi/in.)	h_{eff} (in.)
10/23/2023	57	COA-U	Geotextile	6	Yes	7.92	28	263	7.76

3.5.3. Site 4

Tables 18 and 19 list the results of the FWD backcalculation for each of the sections at Site 4. Table 18 contains the results for Sites 4A through 4H, which were each 4 in. thick. The average backcalculated effective thickness of these sections was 10.0 in., which was 6 in. higher than the overlay design thickness of 4 in. Table 19 contains the results for Sites 4I through 4P, which were each 6 in. thick. The average backcalculated effective thickness of these sections was 11.7 in., which was 5.7 in. greater than the overlay design thickness of 6 in. Both sets of test sections at Site 4 had the same underlying pavement structure (3 in. HMA over 7 in. PCC), and both appeared to receive a similar structural contribution from the underlying pavement. The underlying pavement structure at Site 4 also matched those of Sites 1 and 2. Overall, the structural response of the sections at Site 4 appeared to be much closer to that of Site 1.

Table 17. FWD backcalculation results for the 4 in. sections at Site 4

Site	Test Date	Air Temp (°F)	Overlay Type	h_{PCC} (in.)	Fibers	D_0 (mils)	ℓ (in.)	k (psi/in.)	h_{eff} (in.)
4A	10/23/2023	66	COA-B	4	No	6.35	31.3	311	8.77
4B	10/23/2023	65	COA-B	4	No	7.83	29.5	364	8.21
4C	10/23/2023	65	COA-B	4	No	4.40	33.6	357	11.0
4D	10/23/2023	66	COA-B	4	No	4.29	36.2	316	11.6
4E	10/24/2023	61	COA-B	4	Yes	5.31	32.8	303	10.0
4F	10/24/2023	62	COA-B	4	Yes	5.12	34.5	303	10.7
4G	10/24/2023	61	COA-B	4	Yes	4.75	33.0	336	10.5
4H	10/24/2023	63	COA-B	4	Yes	5.02	28.2	454	9.20
Averages						5.38	32.4	343	10.0

Table 18. FWD backcalculation results for the 6 in. sections at Site 4

Site	Test Date	Air Temp (°F)	Overlay Type	h_{PCC} (in.)	Fibers	D_0 (mils)	ℓ (in.)	k (psi/in.)	h_{eff} (in.)
4I	10/24/2023	64	COA-U	6	Yes	3.52	38.2	393	12.0
4J	10/24/2023	65	COA-U	6	Yes	2.96	30.7	601	11.6
4K	10/24/2023	64	COA-U	6	Yes	4.00	38.6	310	12.6
4L	10/24/2023	64	COA-U	6	Yes	3.30	30.8	538	11.2
4M	10/24/2023	66	COA-U	6	No	4.06	31.0	441	10.5
4N	10/24/2023	65	COA-U	6	No	3.57	35.8	392	12.3
4O	10/24/2023	65	COA-U	6	No	3.74	35.6	383	12.1
4P	10/24/2023	65	COA-U	6	No	5.18	37.0	263	11.3
Averages						3.79	34.7	415	11.7

3.5.4. Site 5

Table 20 lists the results of FWD backcalculation for Site 5. The backcalculated effective thickness was 9.86 in., which was 3.86 in. greater than the overlay design thickness of 6 in. Given the magnitude of the difference between the design overlay thickness and effective thickness, the underlying layer appears to have contributed to the structural response of the overlay. The underlying pavement at Site 5 was a 6 in. thick asphalt pavement.

Table 19. FWD backcalculation results for Site 5

Test Date	Air Temp (°F)	Overlay Type	h_{PCC} (in.)	Fibers	D_0 (mils)	ℓ (in.)	k (psi/in.)	h_{eff} (in.)
10/23/2023	60	COA-U	6	Yes	4.56	30.3	389	9.86

3.5.5. Site 6

Table 21 lists the results of the FWD backcalculation for each of the sections at Site 6. The average backcalculated effective thickness at Site 6 was 8.03 in., which was 2.03 in. greater than the design overlay thickness of 6 in. Site 6 was a COC–U overlay of an existing 7 in. PCC pavement with a geotextile separation layer.

Table 20. FWD backcalculation results for Site 6

Site	Test Date	Air Temp (°F)	Overlay Type	h_{PCC} (in.)	Fibers	D_0 (mils)	ℓ (in.)	k (psi/in.)	h_{eff} (in.)
6A	11/8/2023	54	COC-U	6	No	6.57	29.0	306	8.58
6B	11/8/2023	54	COC-U	6	Yes	8.68	30.3	245	8.21
6C	11/8/2023	53	COC-U	6	Yes	7.26	25.7	341	7.37
6D	11/8/2023	55	COC-U	6	Yes	8.90	25.6	230	7.60
6E	11/8/2023	53	COC-U	6	Yes	7.18	29.5	273	8.36
6F	11/8/2023	54	COC-U	6	Yes	6.63	29.6	308	8.73
6G	11/8/2023	53	COC-U	6	Yes	7.16	27.5	299	7.93
6H	11/8/2023	54	COC-U	6	No	7.32	29.9	266	8.44
6I	11/8/2023	55	COC-U	6	No	7.23	26.6	302	7.61
6J	11/8/2023	54	COC-U	6	No	6.96	30.4	263	8.69
6K	11/8/2023	54	COC-U	6	No	8.98	28.2	239	7.60
6L	11/8/2023	55	COC-U	6	No	8.71	26.3	278	7.20
Averages						7.63	28.2	279	8.03

3.5.6. Site 7

Table 22 lists the results of FWD backcalculation for each of the sections at Site 7. The average backcalculated effective thickness at Site 7 was 11.6 in., which was 5.6 in. greater than the overlay design thickness of 6 in. Given the magnitude of the difference between the design overlay thickness and effective thickness, the underlying layer appears to have contributed to the structural response of the overlay. The underlying pavement at Site 7 was a milled, 7 in. thick asphalt pavement.

Table 21. FWD backcalculation results for Site 7

Site	Test Date	Air Temp (°F)	Overlay Type	h_{PCC} (in.)	Fibers	D_0 (mils)	ℓ (in.)	k (psi/in.)	h_{eff} (in.)
7A	11/1/2023	45	COA-U	6	No	2.89	32.0	632	12.3
7B	11/1/2023	44	COA-U	6	Yes	4.22	32.3	387	10.7
7C	11/1/2023	44	COA-U	6	Yes	4.46	34.2	335	11.0
7D	11/1/2023	45	COA-U	6	Yes	4.68	34.3	323	10.9
7E	11/1/2023	47	COA-U	6	Yes	3.82	35.0	395	11.9
7F	11/1/2023	47	COA-U	6	Yes	3.30	34.6	486	12.5
Averages						3.90	33.7	426	11.6

3.5.7. Summary of Results

The backcalculated effective thickness and maximum center slab deflection values from each test site are plotted together in Figure 57 and 58, respectively. Values for the individual sections in Sites 4, 6, and 7 are averaged together in Figures 57 and 58.

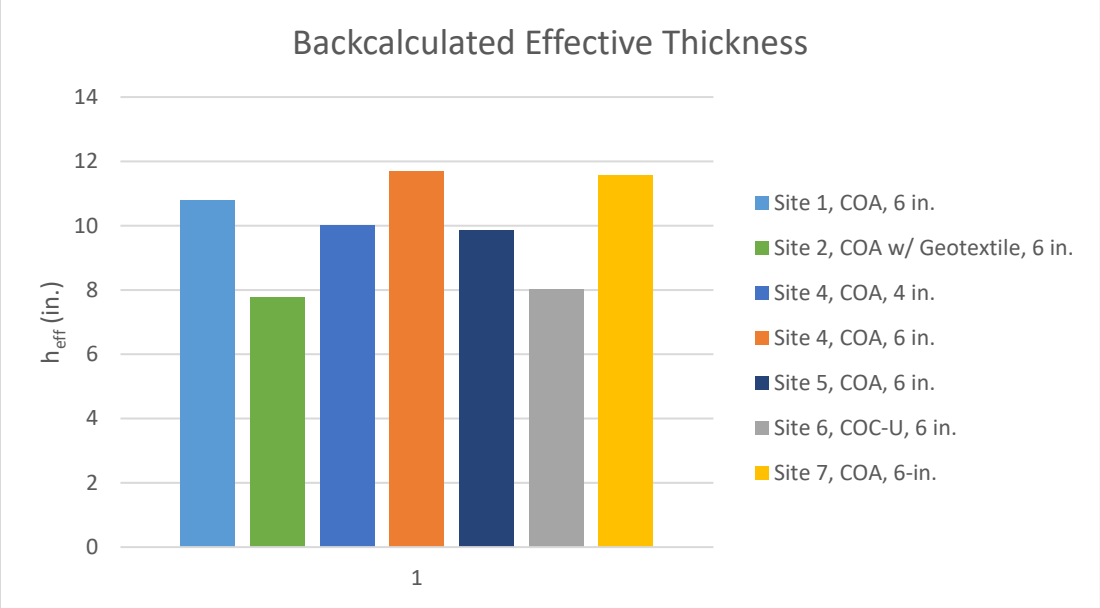

Figure 57. Summary of average backcalculated effective thickness values at each site

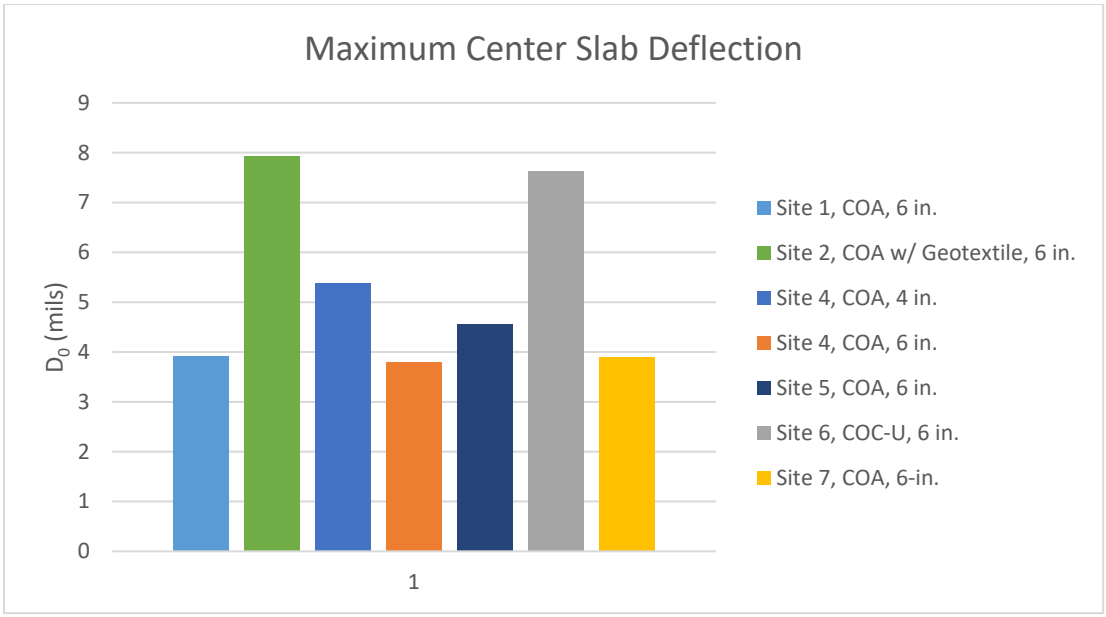

Figure 58. Summary of average maximum center slab deflection values at each site

3.6. High-Speed Surface Profiling

This section contains a summary of the results obtained from the high-speed profiling at each test site. Results are presented for each visit during different seasons and times of day: Spring Morning (AM), Spring Afternoon (PM), Summer AM, Summer PM, Winter AM, and Winter PM. Results were also averaged for each project across all six visits.

Four values are reported: IRI, Curvature IRI, deflection, and deflection ratio. IRI values correspond to the half ride index, calculated from the profiles obtained by the left and right wheel path sensors. Curvature IRI values were also calculated from the curvature profiles obtained just by the left and right wheel path lasers. Deflection and deflection ratio were calculated from all three sensors.

3.6.1. Site 1

Table 23 contains the results from the high-speed profiler runs at Site 1. Additionally, the IRI and Curvature IRI results are plotted in Figures 59 and 60, respectively. Both the IRI and Curvature IRI values were relatively consistent throughout the different seasons and at different times of day. The total range of IRI values across the six visits was 10.5 in./mi, compared to an average of 58.3 in./mi. The total range of Curvature IRI values across the six visits was 5.2 in./mi, compared to an average of 41.2 in./mi.

Table 22. High-speed profiler results for Site 1

Site 1: COA-U, 6 in., 12 ft x 12 ft, Fibers				
	IRI (in./mi)	**Curvature IRI (in./mi)**	**Deflection (in.)**	**Deflection Ratio (in./ft)**
Spring AM	65.0	44.0	0.0283	0.00236
Spring PM	61.1	40.8	0.0278	0.00231
Summer AM	54.5	38.8	0.0259	0.00216
Summer PM	55.9	40.1	0.0261	0.00217
Fall AM	57.3	42.4	0.0281	0.00234
Fall PM	55.9	41.0	0.0255	0.00212
Average	58.3	41.2	0.0269	0.00224

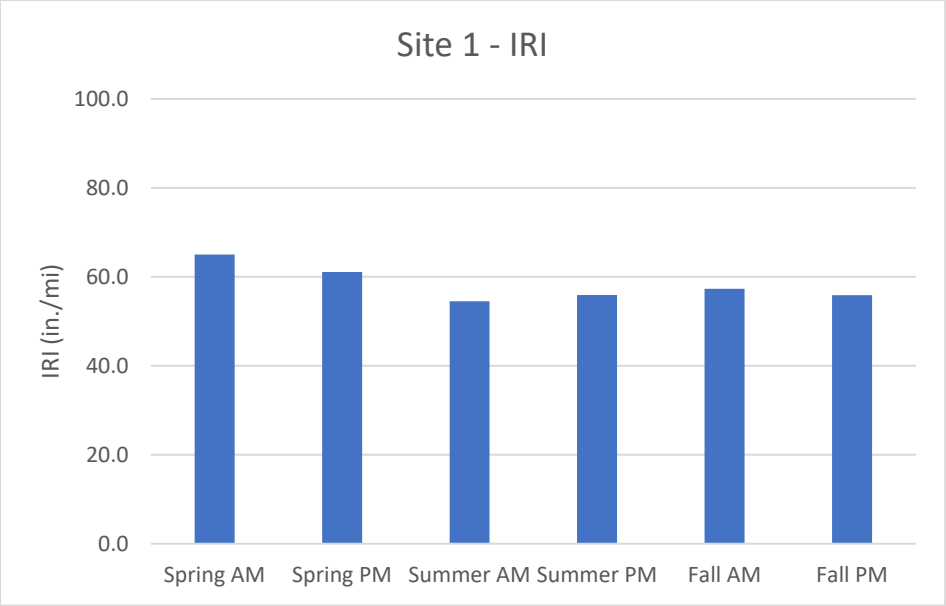

Figure 59. IRI results for Site 1

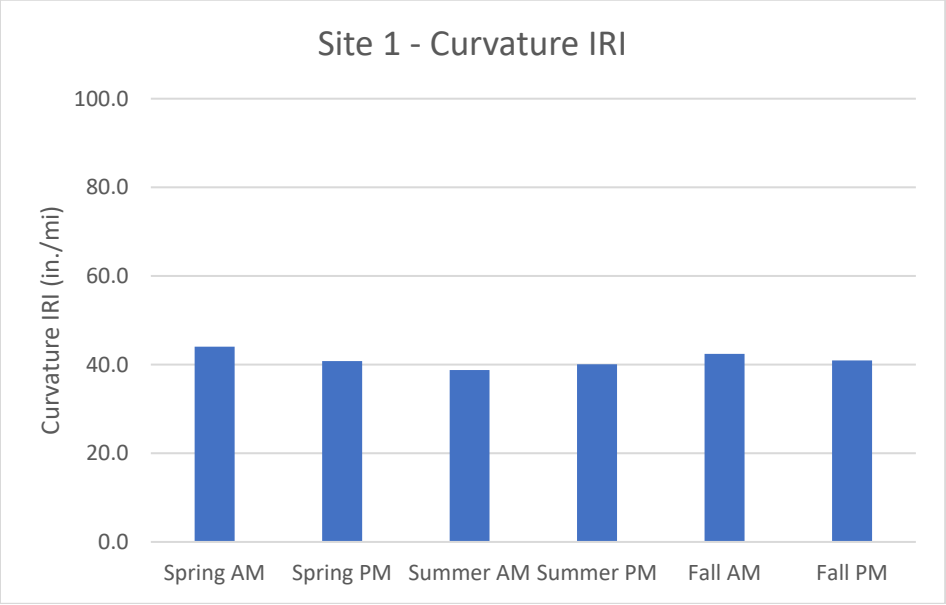

Figure 60. Curvature IRI results for Site 1

3.6.2. Site 2

Table 24 contains the results from the high-speed profiler runs at Site 2. Additionally, the IRI and Curvature IRI results are plotted in Figures 61 and 62, respectively. The total range of IRI values across the six visits was 14.7 in./mi, compared to an average of 63.7 in./mi. The highest IRI values were obtained during the fall morning and afternoon runs, while the lowest IRI values were obtained during the two spring runs. The range of Curvature IRI values across the six visits was 18.0 in./mi, compared to an average of 41.2 in./mi. The highest Curvature IRI values were

also obtained during the two fall runs, while the lowest Curvature IRI values were obtained during the two spring runs.

Table 23. High-speed profiler results for Site 2

Site 2: COA-U (w/ Geotextile), 6 in., 12 ft x 12 ft, Fibers				
	IRI (in./mi)	**Curvature IRI (in./mi)**	**Deflection (in.)**	**Deflection Ratio (in./ft)**
Spring AM	59.6	49.3	0.0253	0.00211
Spring PM	56.0	44.8	0.0270	0.00225
Summer AM	63.6	54.5	0.0336	0.00280
Summer PM	64.7	55.1	0.0328	0.00274
Fall AM	70.7	62.8	0.0382	0.00318
Fall PM	67.9	56.4	0.0322	0.00268
Average	63.7	53.8	0.0315	0.00263

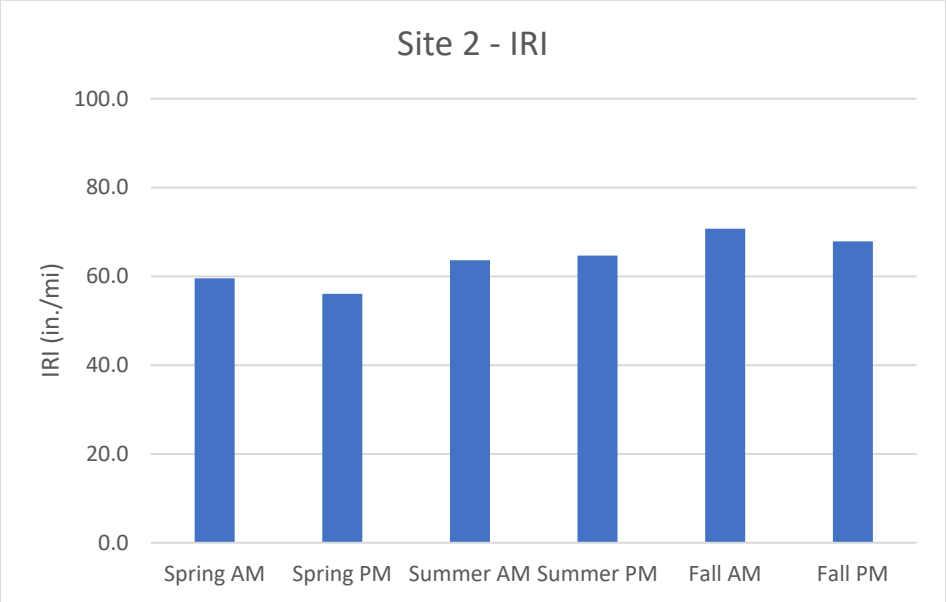

Figure 61. IRI results for Site 2

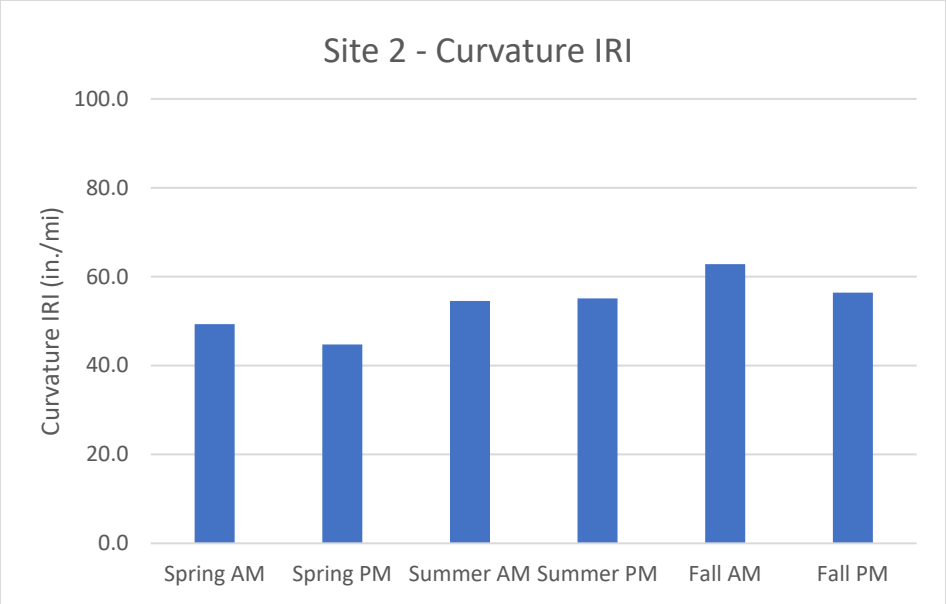

Figure 62. Curvature IRI results for Site 2

3.6.3. Site 4

Figures 63 through 70 plot the IRI and Curvature IRI results obtained at Site 4. Separate figures are provided for each combination of thickness and fiber reinforcement, with the results organized by joint spacing within each figure. Due to the significant number of individual sections within Site 4, the tables containing the full results of each high-speed profiler visit are included in Appendix C. The IRI and Curvature IRI results across all six visits are averaged together in Figures 71 and 72, respectively, for each combination of thickness, joint spacing, and fiber reinforcement.

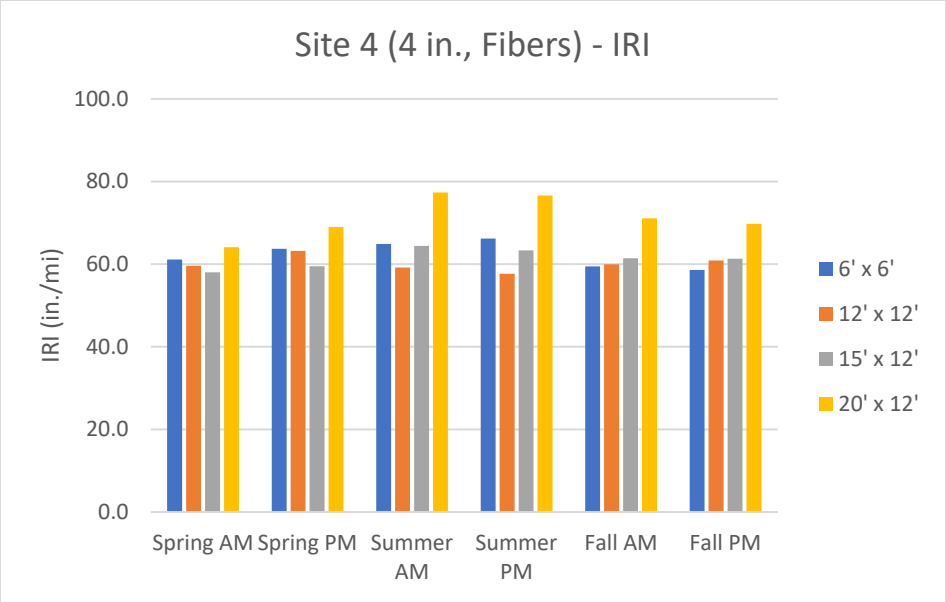

Figure 63. IRI results for 4 in. sections with fibers at Site 4

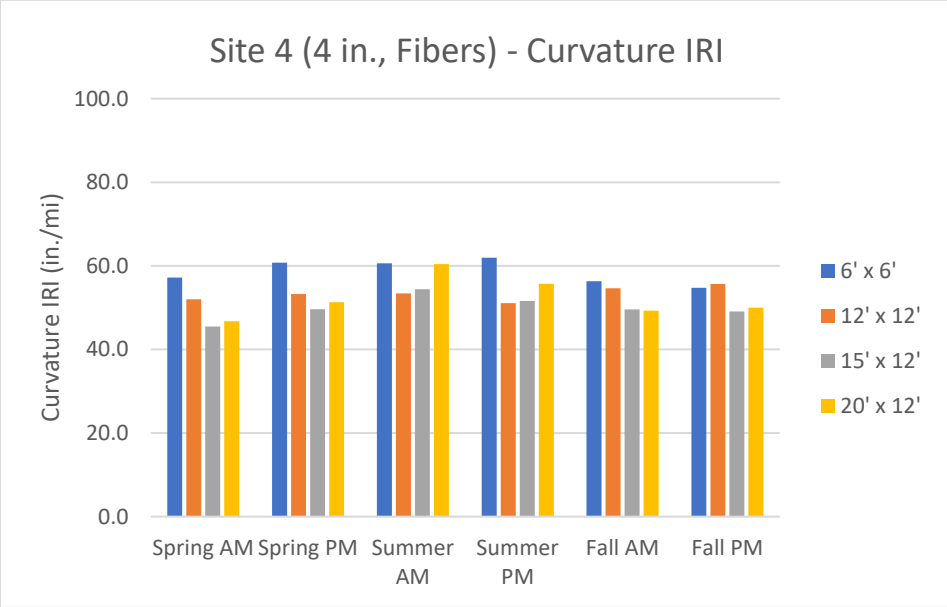

Figure 64. Curvature IRI results for 4 in. sections with fibers at Site 4

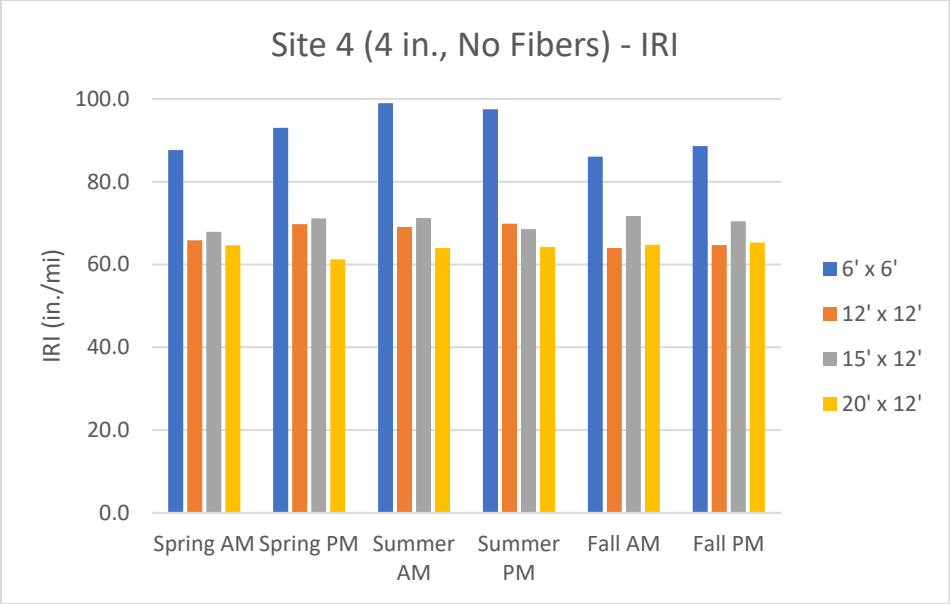

Figure 65. IRI results for 4 in. sections without fibers at Site 4

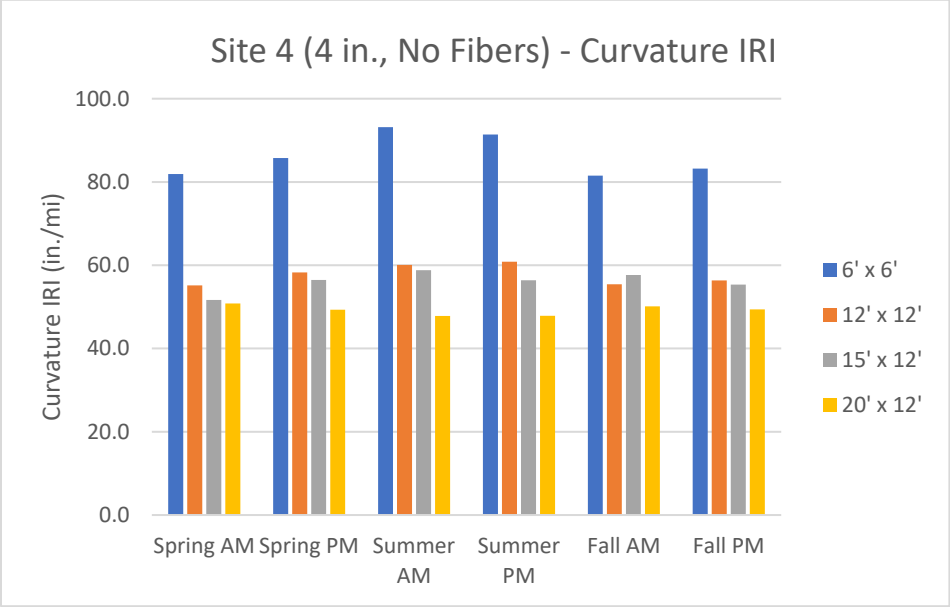

Figure 66. Curvature IRI results for 4 in. sections without fibers at Site 4

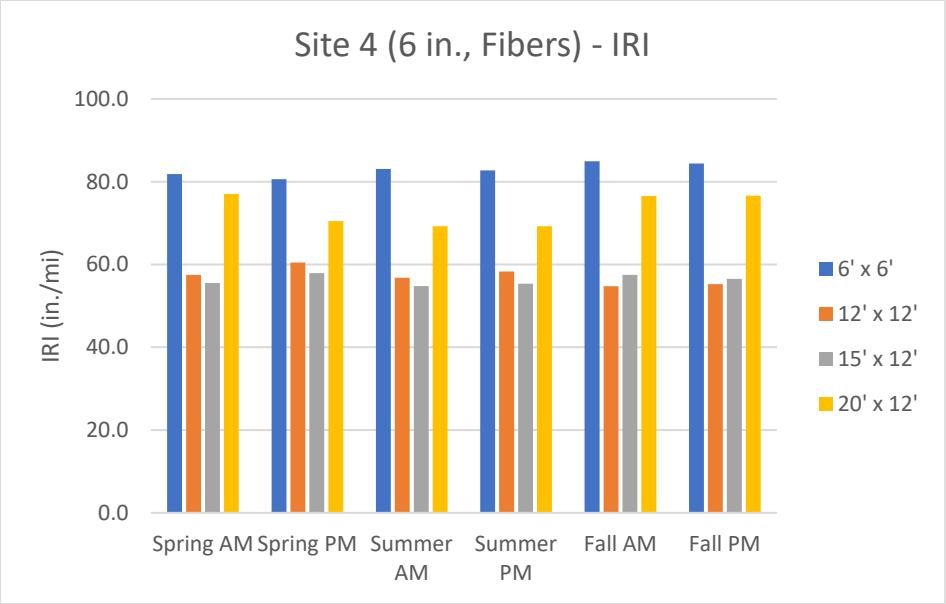

Figure 67. IRI results for 6 in. sections with fibers at Site 4

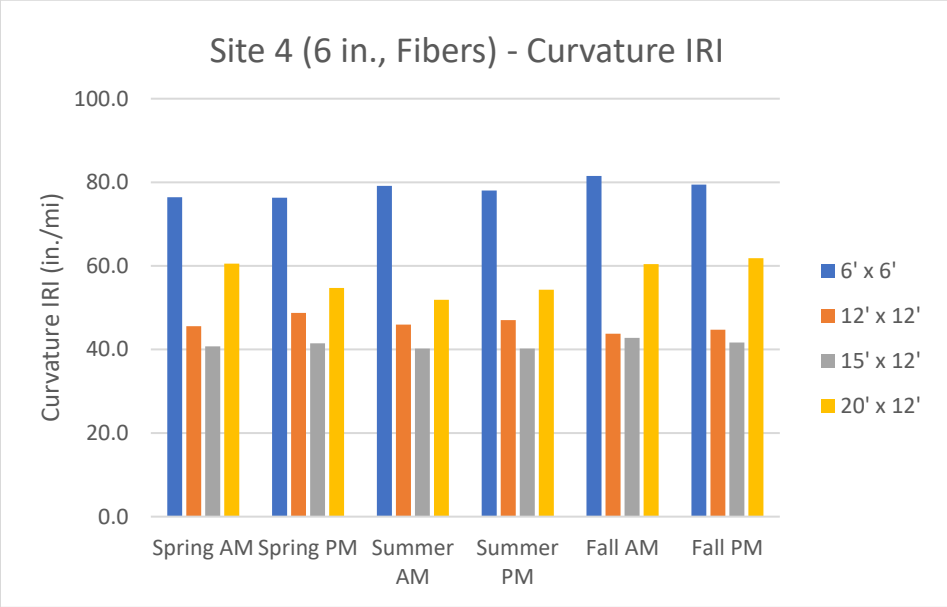

Figure 68. Curvature IRI results for 6 in. sections with fibers at Site 4

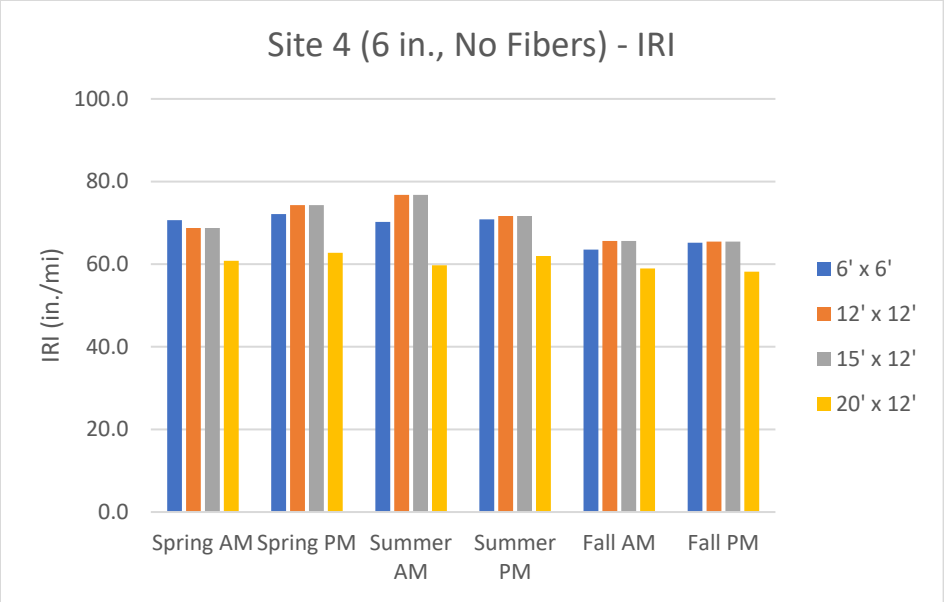

Figure 69. IRI results for 6 in. sections without fibers at Site 4

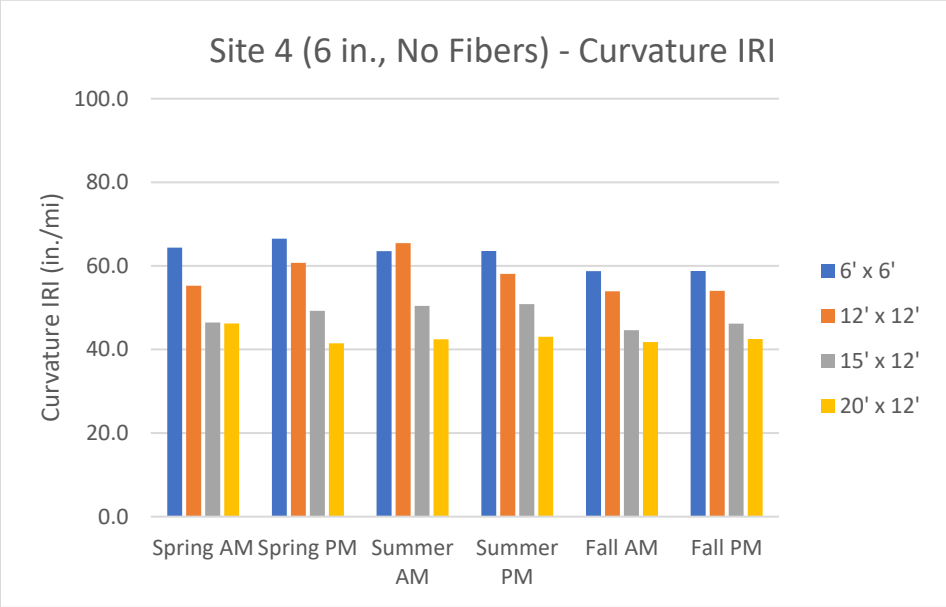

Figure 70. Curvature IRI results for 6 in. sections without fibers at Site 4

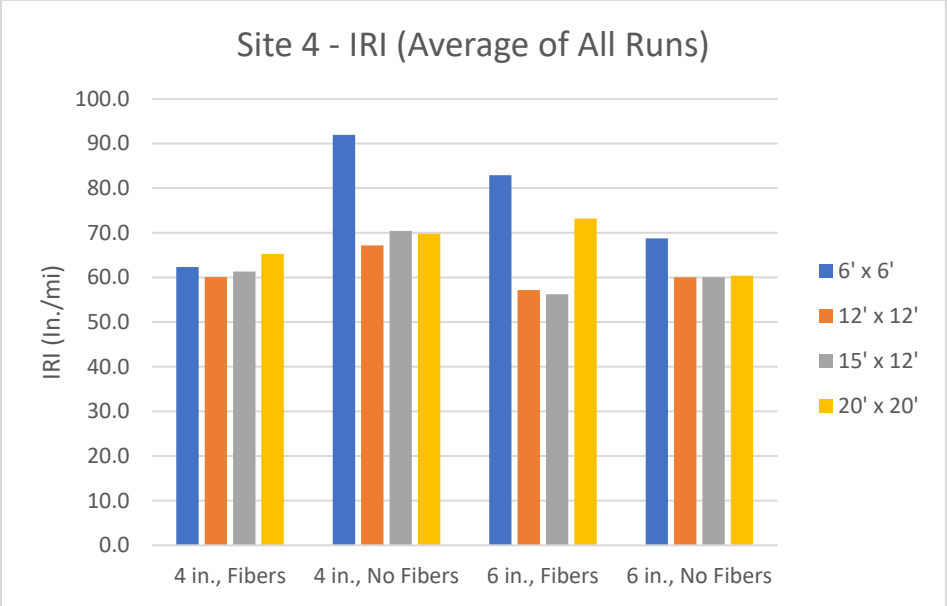

Figure 71. Average IRI results across all visits for Site 4

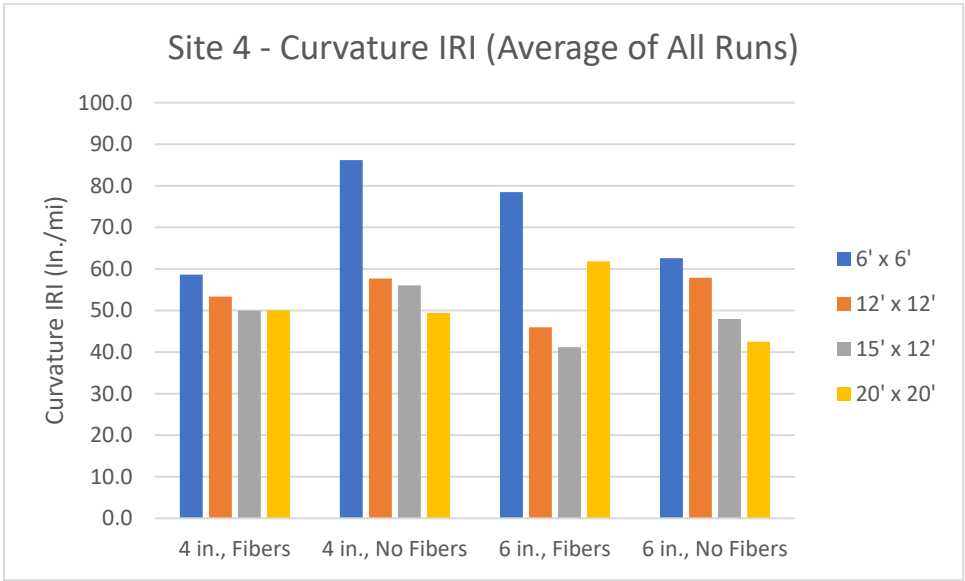

Figure 72. Average Curvature IRI results across all visits for Site 4

There were a number of notable trends in the results at Site 4. In general, sections with 6 ft joint spacing had the highest IRI and Curvature IRI values for each combination of thickness and fiber reinforcement. For the sections that were 4 in. thick without fibers and 6 in. thick with fibers, IRI values for the 6 ft joint sections were between 9 in./mi to 25 in./mi greater than the IRI values for the sections with longer joint spacings, and the Curvature IRI values were anywhere from 16 in./mi to 39 in./mi greater than the Curvature IRI values for the sections with longer joint spacings. For the sections that were 4 in. thick with fibers and 6 in. thick without fibers, these differences were not as large in magnitude.

There were no other consistent trends related to joint spacing, as most sections with the same thickness and fiber content had similar IRI and Curvature IRI values for each of the 12 ft, 15 ft, and 20 ft joint spacing designs. One exception was Site 4L, which was 6 in. thick with 20 ft joint spacing and fiber reinforcement and had an IRI and Curvature IRI about 20 in./mi greater than the corresponding sections with 12 ft (Site 4J) and 15 ft (Site 4K) joint spacing. That said, the average IRI for Site 4L was about 10 in./mi less than that of Site 4I, which was the corresponding section with 6 ft joint spacing, and the Curvature IRI for Site 4L was about 20 in./mi less than that of Site 4I.

In comparing sections with the same joint spacing to each other, there were no consistent trends between IRI or Curvature IRI and either thickness or fiber reinforcement. There were also no notable or consistent trends for any individual section between IRI or Curvature IRI and the season or time of day. The only section with a range of more than 10.0 in./mi for either IRI or Curvature IRI across all six visits was Site 4A, which was 4 in. thick with 6 ft joint spacing and without fiber reinforcement.

3.6.4. Site 5

Table 25 contains the results from the high-speed profiler runs at Site 2. Additionally, the IRI and Curvature IRI results are plotted in Figures 73 and 74, respectively. The total range of IRI values across the six visits was 11.7 in./mi, compared to an average of 41.1 in./mi. The highest IRI values were obtained during the spring morning and afternoon runs, while the lowest IRI values were obtained during the two fall runs. The range of Curvature IRI values across the six visits was 6.2 in./mi, compared to an average of 30.8 in./mi. The highest Curvature IRI values were also obtained during the two spring runs, while the lowest Curvature IRI values were obtained during the two fall runs.

Table 24. High-speed profiler results for Site 5

Site 5: COA-U, 6 in., 12 ft x 12 ft, Fibers				
	IRI (in./mi)	**Curvature IRI (in./mi)**	**Deflection (in.)**	**Deflection Ratio (in./ft)**
Spring AM	47.2	34.2	0.0234	0.00195
Spring PM	47.5	33.9	0.0241	0.00201
Summer AM	39.5	29.9	0.0212	0.00177
Summer PM	38.5	30.0	0.0209	0.00174
Fall AM	35.8	28.0	0.0176	0.00147
Fall PM	37.9	28.7	0.0189	0.00158
Average	41.1	30.8	0.0210	0.00175

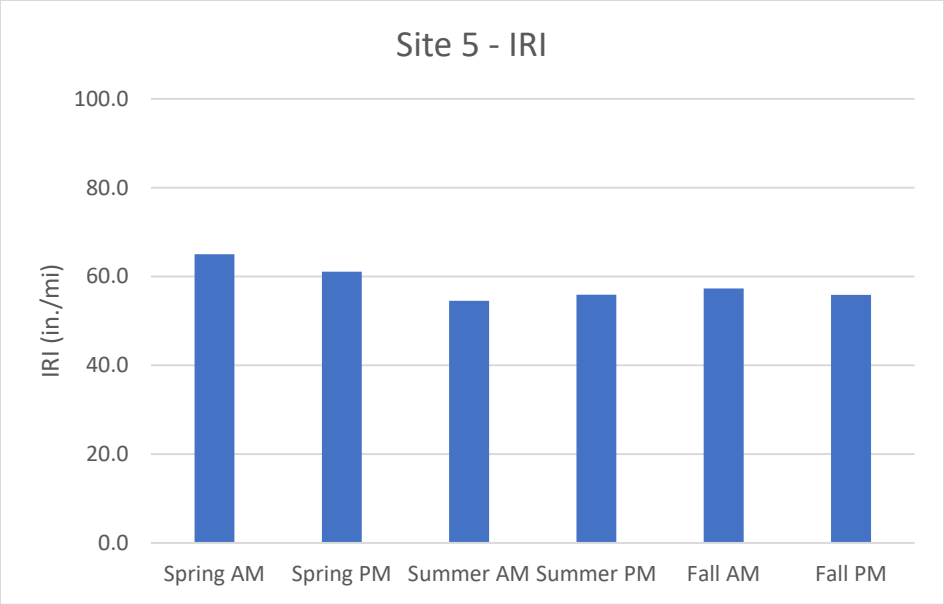

Figure 73. IRI results for Site 5

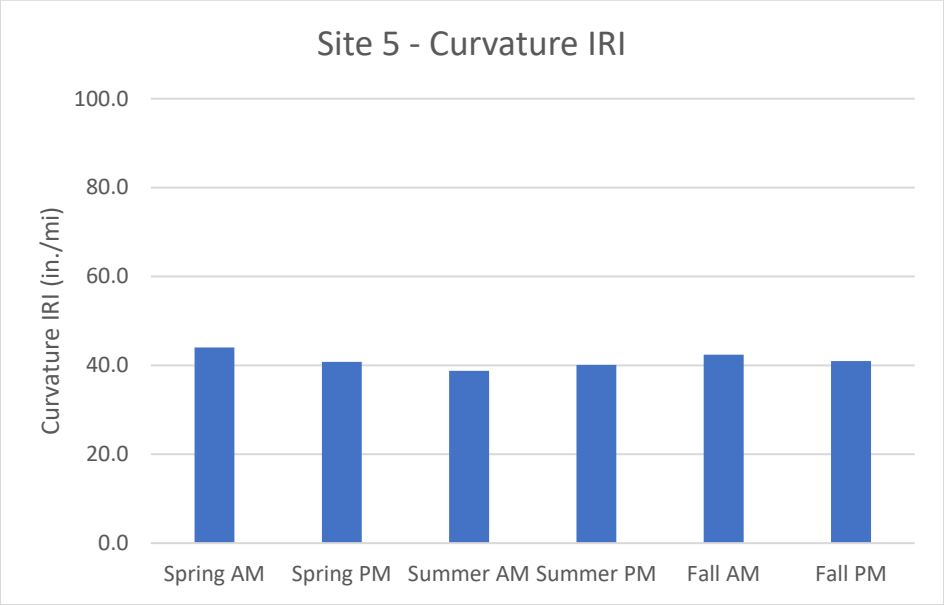

Figure 74. Curvature IRI results for Site 5

3.6.5. Site 6

Figures 75 through 78 plot the IRI and Curvature IRI results obtained at Site 6. Separate figures are provided for the sections with and without fiber reinforcement, with the results organized by joint spacing within each figure. Due to the significant number of individual sections within Site 6, the tables containing the full results of each high-speed profiler visit are included in Appendix C. The IRI and Curvature IRI results across all six visits are averaged together in Figures 79 and 80, respectively, for each combination of joint spacing and fiber reinforcement.

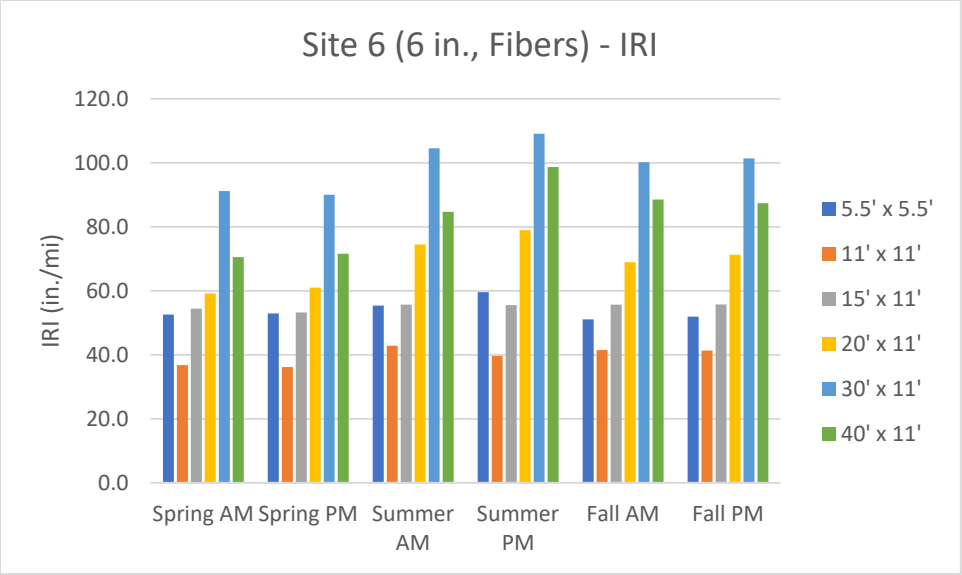

Figure 75. IRI results for sections with fibers at Site 6

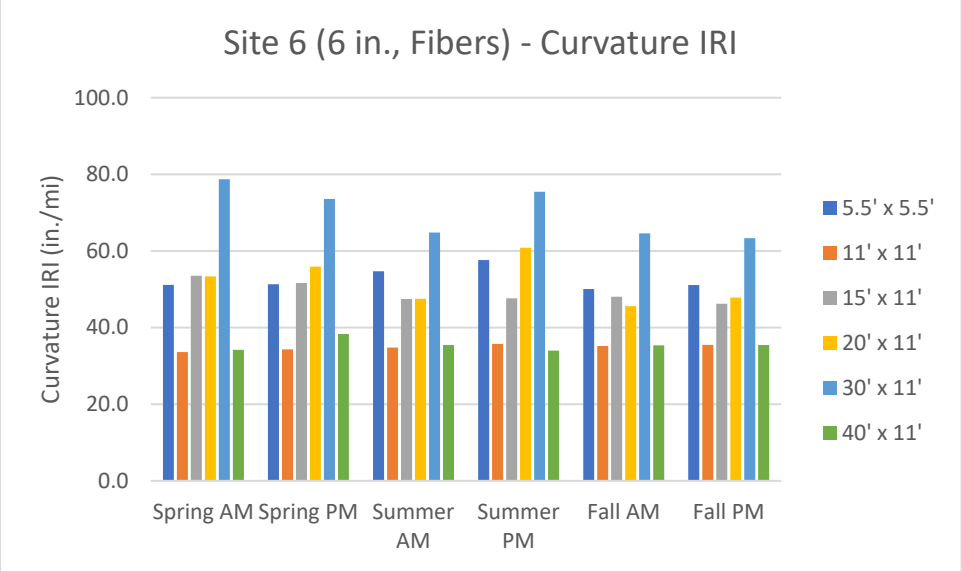

Figure 76. Curvature IRI results for sections with fibers at Site 6

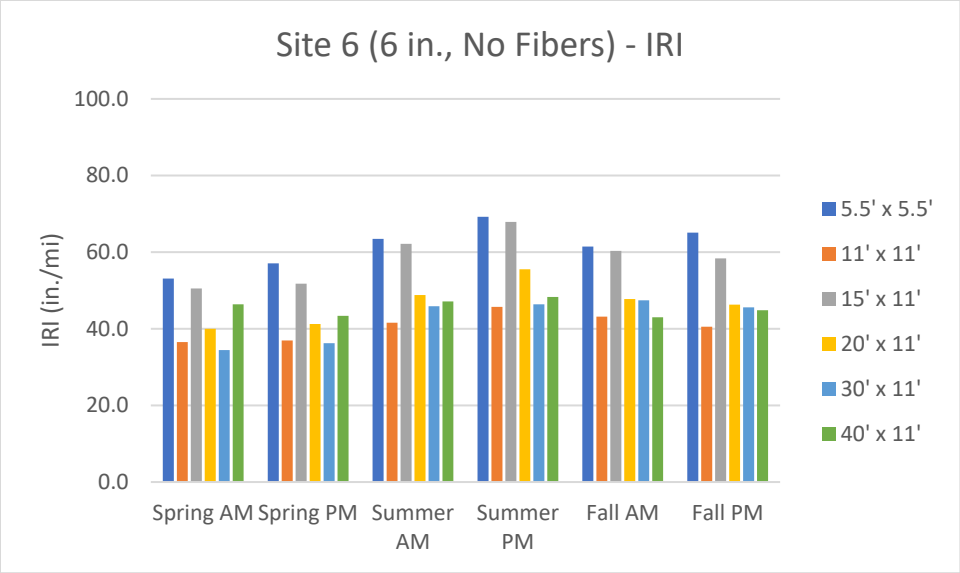

Figure 77. IRI results for sections without fibers at Site 6

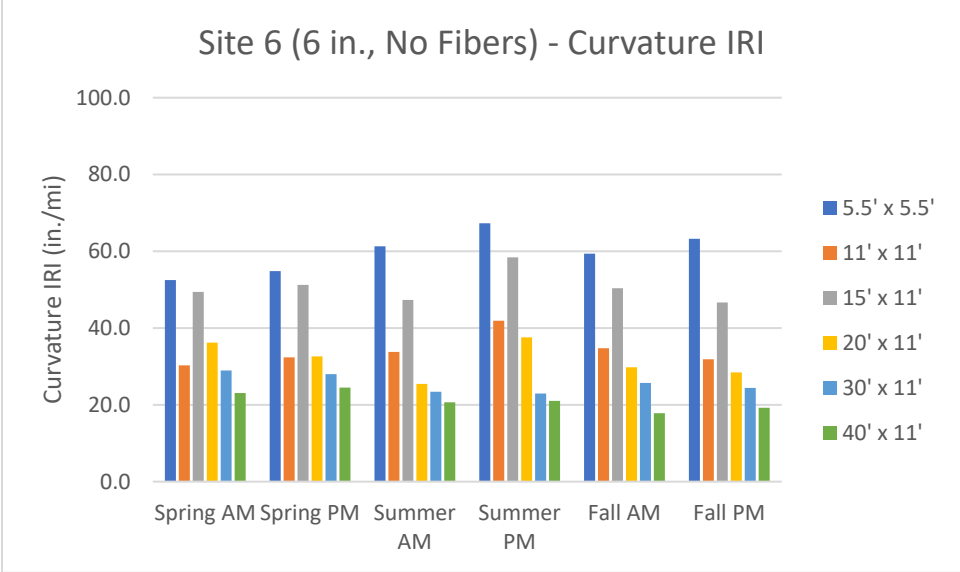

Figure 78. Curvature IRI results for sections without fibers at Site 6

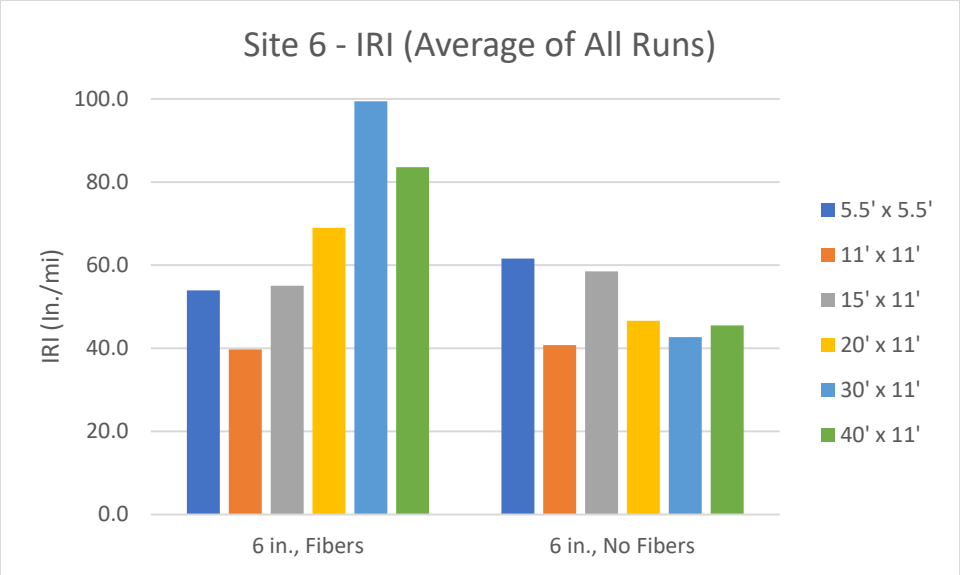

Figure 79. Average IRI results across all visits for Site 6

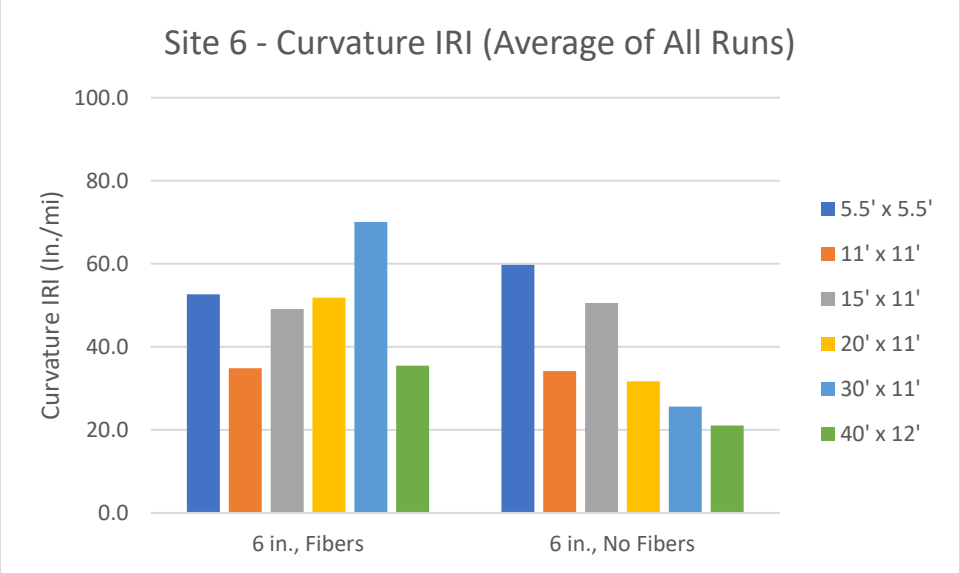

Figure 80. Average Curvature IRI results across all visits for Site 6

One complicating factor in analyzing IRI and Curvature IRI trends at Site 6 was the fact that significant portions of these test sites were diamond ground for smoothness after construction, as noted in Table 8. The two sections that had the highest IRI values averaged across all seasons, Site 6F (30 ft joint spacing with fibers, 99.4 in./mi) and Site 6G (40 ft joint spacing with fibers, 83.6 in./mi), were the only two sections that were not diamond ground. While Site 6G also had the highest average Curvature IRI value (70.1 in./mi) of any section at Site 6, Site 6H had one of the lowest average Curvature IRI values (35.5 in./mi) of any of the sections containing fibers. Otherwise, there were no apparent consistent trends between IRI or Curvature IRI and either joint spacing or fiber reinforcement.

With respect to season and time of day, IRI and Curvature IRI values at Site 6 were higher in the summer and fall than in the spring. Most of the individual sections had a range of IRI and Curvature IRI values between 5 in./mi and 10 in./mi across all six measurements. The sections with the highest IRI and Curvature IRI values (Sites 6B, 6D, 6K, and 6L) sometimes had ranges as high as 20 in./mi for both IRI and Curvature IRI across all six measurements.

3.6.6. Site 7

Figures 81 and 82 plot the IRI and Curvature IRI results, respectively, obtained at Site 7. Due to the significant number of individual sections within Site 7, the tables containing the full results of each high-speed profiler visit are included in Appendix C. The IRI and Curvature IRI results across all six visits are averaged together in Figures 83 and 84, respectively.

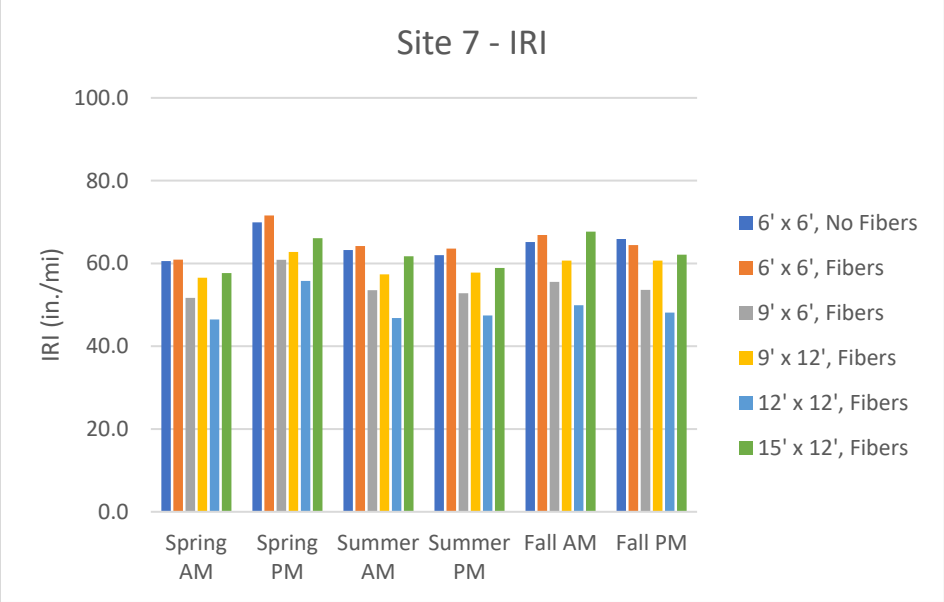

Figure 81. IRI results for Site 7

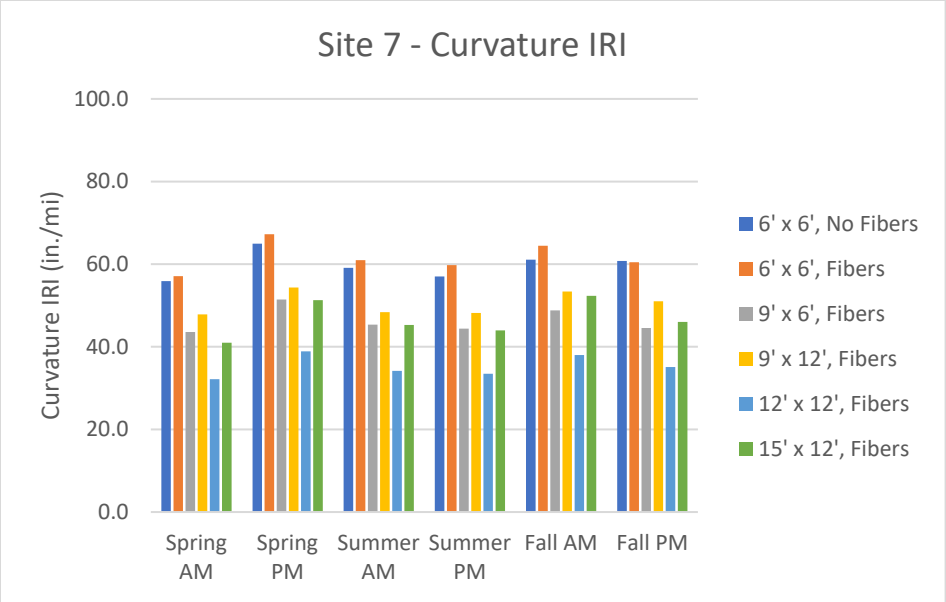

Figure 82. Curvature IRI results for Site 7

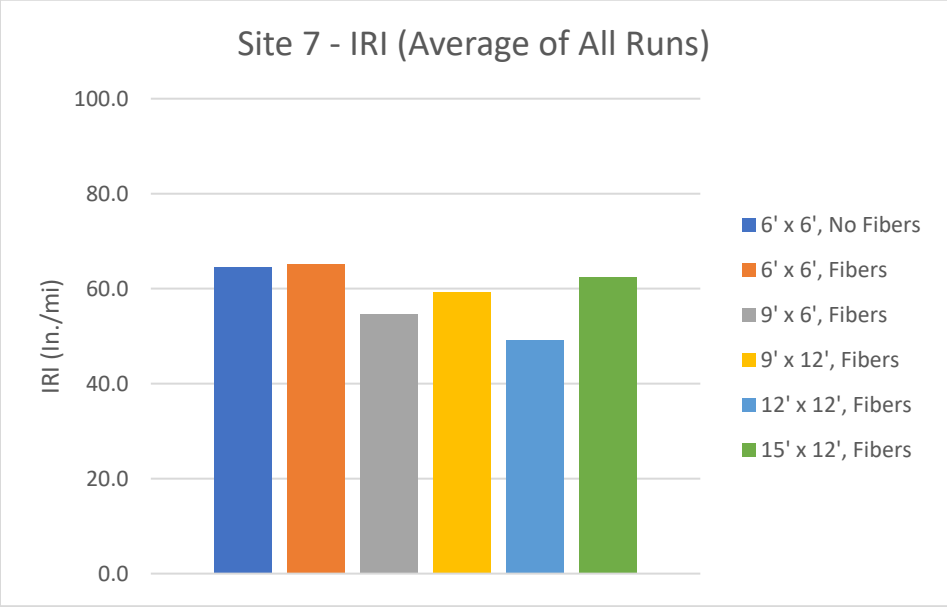

Figure 83. Average IRI results across all visits for Site 7

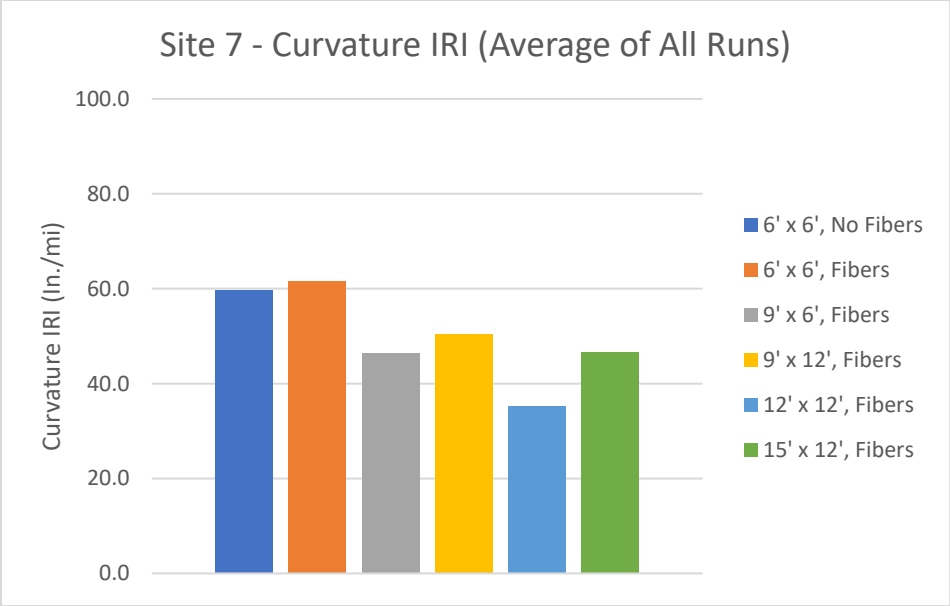

Figure 84. Average Curvature IRI results across all visits for Site 7

Few trends in IRI or Curvature IRI were discerned from the data for Site 7. Site 7C with 12 ft x 12 ft joint spacing had the lowest average IRI and Curvature IRI of any of the sections at Site 7, while the sections at Sites 7A and 7F with 6 ft transverse joint spacing had the highest average IRI and Curvature IRI values. Minimal variation was observed in IRI and Curvature IRI readings between different seasons and times of day. The range of IRI and Curvature IRI values across all six measurements for any given section did not exceed 10 in./mi, except for Sites 7A and 7F (6 x 6 ft joint spacing both with and without fibers), which had ranges of 10 to 12 in./mi in Curvature IRI.

4. DISCUSSION

4.1. Statistical Analysis of Trends in Joint LTE, IRI, and Curvature IRI

Sections 3.4 and 3.6 discussed general trends between concrete overlay design parameters, including thickness, joint spacing, and fiber reinforcement, as well as performance measures. For further investigation of these trends and to determine which effects might be statistically significant, the results of Site 4 and Site 6 were analyzed through multiple linear regression. Thickness, joint spacing, and fiber reinforcement were established as independent variables, and sum of squares F-tests were used to analyze their effects on transverse joint LTE, IRI, and Curvature IRI using the "emmeans" package in R (Lenth 2024). Additional linear regression was performed to analyze the relationship between transverse joint spacing and joint LTE, IRI, and Curvature IRI at Site 7.

4.1.1. Joint LTE

Table 26 presents the F-test results analyzing the size of the effects of thickness (4 in. and 6 in.), joint spacing (6 ft, 12 ft, 15 ft, and 20 ft), and fiber reinforcement (yes or no) on joint LTE at Site 4. The *df1* term indicates the degrees of freedom for each model term, *df2* indicates the degrees of freedom for all terms in the model, the *F-statistic* assesses the significance of the regression model, and the *p-value* analyzes the probability that the null hypothesis for each variable is true, i.e., that the variable does not affect the mean value of the response.

Table 25. Sum of squares F-test results for joint LTE at Site 4

Model Term	df1	df2	F-statistic	p-value
Thickness	1	10	0.466	0.511
Joint Spacing	3	10	7.09	0.00780
Fibers	1	10	4.30	0.065

Based on the results in Table 26 and assuming a 95% level of statistical significance (*p-value* of 0.05 or less), thickness and fiber reinforcement did not have a statistically significant effect on joint LTE at Site 4. Joint spacing, however, did have a statistically significant effect on joint LTE, with a *p-value* of 0.00780.

Table 27 contains the results of a pairwise linear contrast between each joint spacing at Site 4 to further investigate the effect of joint spacing on mean values for joint LTE. The *estimate* column is the difference between mean values for a given contrast, *SE* is the standard error for the contrast, *df* indicates the degrees of freedom for the contrast, the *t-statistic* assesses the significance of the contrast, and the *p-value* analyzes the probability that the null hypothesis is true, i.e., that there is no difference in the mean values in each contrast.

Table 26. Pairwise linear contrasts for joint spacing and joint LTE at Site 4

Contrast	Estimate	SE	df	t-statistic	p-value
6–12 ft	4.75	1.37	10	3.46	0.0265
6–15 ft	5.58	1.37	10	4.06	0.0103
6–20 ft	5.05	1.37	10	3.68	0.0187
12–15 ft	0.825	1.37	10	0.601	0.930
12–20 ft	0.300	1.37	10	0.218	0.997
15–20 ft	-0.525	1.37	10	-0.382	0.980

The results in Table 27 indicate that the differences between average joint LTE in the 6 ft sections and the sections with longer joint spacing designs, which ranged from 4.75% to 5.58%, were statistically significant, with a *p-value* of less than 0.05. The differences in average joint LTE between sections with 12 ft, 15 ft, and 20 ft joint spacing were not found to be significant.

Table 28 presents the results of the F-test analyzing the size of the effects of joint spacing (5.5 ft, 11 ft, 15 ft, 20 ft, 30 ft, and 40 ft) and fiber reinforcement (yes or no) on joint LTE at Site 6. (Thickness was not a variable at Site 6, so it was not included in this regression.) Like at Site 4, fiber reinforcement did not affect the mean values for joint LTE, but joint spacing was found to have a statistically significant effect on joint LTE.

Table 27. Sum of squares F-test results for joint LTE at Site 6

Model Term	df1	df2	F-statistic	p-value
Joint Spacing	5	5	6.68	0.0287
Fibers	1	5	0.846	0.400

Table 29 contains the results of a pairwise linear contrast to further investigate the effect of joint spacing on mean values for joint LTE at Site 6. The differences between average joint LTE for the sections with 5.5 ft joint spacing and the sections with 15 ft and 40 ft joint spacing designs were statistically significant to a 95% probability, with a *p-value* of less than 0.05, while the other differences between joint LTE for the sections with 5.5 ft joint spacing and those with longer joint spacing designs were not significant at this level of probability. None of the differences in average joint LTE between sections with joint spacings 11 ft or greater were found to be statistically significant.

Table 28. Pairwise linear contrasts for joint spacing and joint LTE at Site 6

Contrast	Estimate	SE	df	t-statistic	p-value
5.5–11 ft	21.2	5.96	5	3.56	0.0967
5.5–15 ft	26.0	5.96	5	4.35	0.0463
5.5–20 ft	22.2	5.96	5	3.72	0.0830
5.5–30 ft	25.2	5.96	5	4.22	0.0522
5.5–40 ft	31.5	5.96	5	5.28	0.0214
11–15 ft	4.75	5.96	5	0.797	0.956
11–20 ft	0.95	5.96	5	0.159	1.00
11–30 ft	3.95	5.96	5	0.663	0.979
11–40 ft	10.3	5.96	5	1.72	0.573
15–20 ft	-3.80	5.96	5	-0.637	0.982
15–30 ft	-0.80	5.96	5	-0.134	1.00
15–40 ft	5.50	5.96	5	0.923	0.925
20–30 ft	3.00	5.96	5	0.503	0.994
20–40 ft	9.30	5.96	5	1.56	0.650
30–40 ft	6.30	5.96	5	1.06	0.880

To further analyze trends between transverse joint spacing and joint LTE, Figure 85 plots a linear regression at Site 7, including linear trendlines. The results from Sites 4 and 6 were also plotted as a point of comparison. Table 30 contains slope (m) and coefficient of determination (R^2) values for each of the linear trendlines. Each test site demonstrated a trend of decreasing joint LTE with increasing joint spacing, although as discussed in Tables 27 and 29, only the differences between sections with 5.5 ft and 6 ft joint spacing and sections with longer joint spacings were significant at Site 4 and Site 6. The relationship at Site 7 had the slope with the greatest decreasing magnitude, as well as the highest R^2 value.

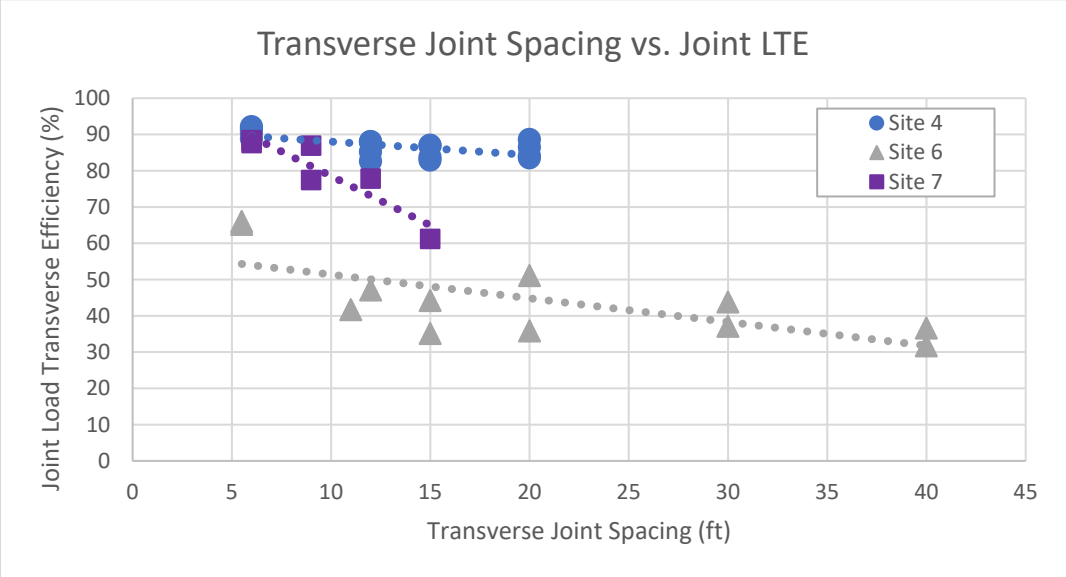

Figure 85. Transverse joint spacing versus joint LTE at Sites 4, 6, and 7

Table 29. Slope and R^2 values for joint spacing versus joint LTE trendlines at Sites 4, 6, and 7

Section	m	R^2
Site 4	-0.369	0.412
Site 6	-2.716	0.494
Site 7	-0.653	0.832

4.1.2. IRI and Curvature IRI

Tables 31 and 32 present the F-test results analyzing the size effects of thickness (4 in. and 6 in.), joint spacing (6 ft, 12 ft, 15 ft, and 20 ft), and fiber reinforcement (yes or no) on IRI and Curvature IRI, respectively, at Site 4. Thickness, joint spacing, and fiber reinforcement did not have a significant impact on mean values of IRI at Site 4. Meanwhile, neither thickness nor fiber reinforcement had a significant effect on Curvature IRI, but joint spacing was observed to have a significant effect on Curvature IRI, with a p-value of 0.014.

Table 30. Sum of squares F-test results for IRI at Site 4

Model Term	df1	df2	F-statistic	p-value
Thickness	1	10	0.291	0.601
Joint Spacing	3	10	2.12	0.161
Fibers	1	10	0.633	0.445

Table 31. Sum of squares F-test results for Curvature IRI at Site 4

Model Term	df1	df2	F-statistic	p-value
Thickness	1	10	0.716	0.417
Joint Spacing	3	10	5.92	0.014
Fibers	1	10	0.464	0.5112

Table 33 shows pairwise linear contrasts in Curvature IRI values between sections with different joint spacing. The only significant differences between sections with different joint spacings were between sections with 6 ft joint spacing and those with 15 ft and 20 ft joint spacing. Curvature IRI values for the 6 ft joint spacing sections were higher than the Curvature IRI values for sections with longer joint spacing designs, with differences ranging from 17.7 to 22.7 in./mi. No significant differences were observed in Curvature IRI between any of the sections with joint spacings of 12 ft or greater.

Table 32. Pairwise linear contrasts for joint spacing and Curvature IRI at Site 4

Contrast	Estimate	SE	df	t-statistic	p-value
6–12 ft	17.7	6.07	10	2.92	0.0624
6–15 ft	22.7	6.07	10	3.73	0.0172
6–20 ft	21.0	6.07	10	3.46	0.0262
12–15 ft	4.94	6.07	10	0.813	0.847
12–20 ft	3.31	6.07	10	0.545	0.946
15–20 ft	-1.63	6.07	10	-0.268	0.993

Tables 34 and 35 present the F-test results analyzing the effects of joint spacing (5.5 ft, 11 ft, 15 ft, 20 ft, 30 ft, and 40 ft) and fiber reinforcement on IRI and Curvature IRI, respectively, at Site 6. Neither joint spacing nor fibers were found to have a significant effect on either IRI or Curvature IRI.

Table 33. Sum of squares F-test results for IRI at Site 6

Model Term	df1	df2	F-statistic	p-value
Joint Spacing	5	5	1.352	0.374
Fibers	1	5	3.917	0.105

Table 34. Sum of squares F-test results for Curvature IRI at Site 6

Model Term	df1	df2	F-statistic	p-value
Joint Spacing	5	5	0.627	0.690
Fibers	1	5	1.74	0.244

Finally, Figures 86 and 87 plot linear regressions of transverse joint spacing versus IRI and Curvature IRI, respectively, at Site 7. The relationship between joint spacing and IRI was weak, with a low R^2 value. The relationship between transverse joint spacing and Curvature IRI showed a clearer decrease in Curvature IRI with increasing joint spacing and had a higher R^2 value.

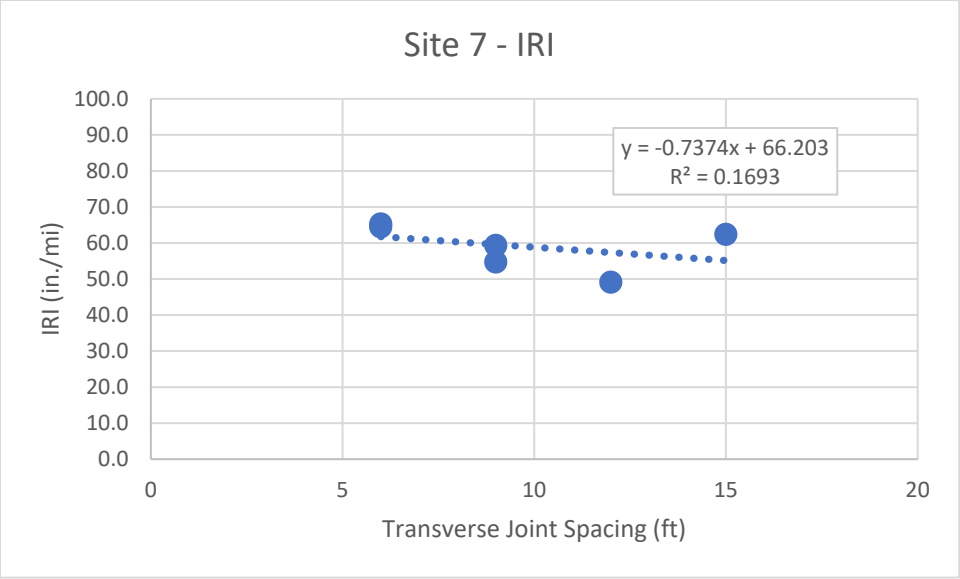

Figure 86. Transverse joint spacing versus IRI at Site 7

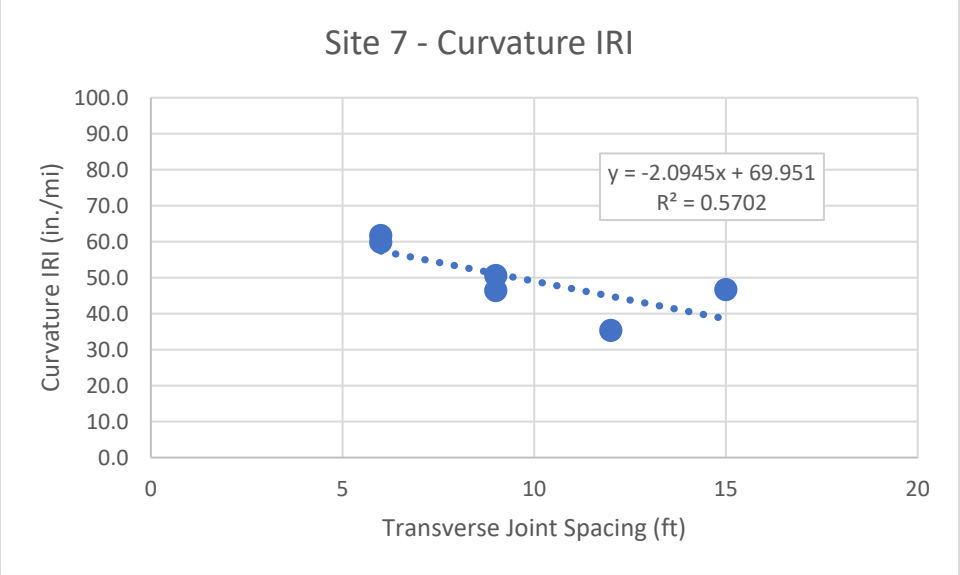

Figure 87. Transverse joint spacing versus Curvature IRI at Site 7

4.1.3. Summary of Findings

This statistical analysis found that neither overlay thickness (at Site 4) nor fiber reinforcement (at Site 4 and Site 6) had a statistically significant effect on concrete overlay performance in terms of joint LTE, IRI, or Curvature IRI to date. Meanwhile, the effect of transverse joint spacing on joint LTE was found to be significant at Sites 4 and 6. Overlay sections with shorter (5.5 ft or 6 ft) joint spacing designs had a higher joint LTE than sections with joint spacing designs of 11 ft or greater, and several of these differences were statistically significant. A general relationship between increasing joint spacing and decreasing joint LTE was also observed at Site 7.

Transverse joint spacing was not observed to have a significant effect on average IRI values at Sites 4, 6, or 7. At Site 4, transverse joint spacing had a statistically significant effect on Curvature IRI. Overlay sections with a 6 ft joint spacing had a greater Curvature IRI than those with longer joint spacings. However, this relationship was not significant at Site 6. Curvature IRI also decreased with increasing joint spacing at Site 7.

4.2. Comparing Performance of Different Overlay Types

The overlay sections at Site 1, Site 4, Site 5, and Site 7 were all conventional COA overlays. The sections with 4 in. thickness (Sites 4A through 4H) were categorized as bonded (COA–B) overlays, while the sections with 6 in. thickness (Sites 1, 5, 4I through 4P, and 7A through 7F) were categorized as unbonded (COA–U) overlays. Despite this distinction in categorization, the concrete layer was paved directly over the asphalt layer at each section, so the layers were free to bond together in practice.

The COC–U overlay sections at Site 6 each featured a geotextile separation layer, which deliberately ensured that the concrete overlay did not bond to the underlying pavement. The COA overlay at Site 2 was also constructed with a geotextile separation layer between the concrete overlay and the underlying asphalt layer. Thus, unlike the other COA projects in this study, the COA–U overlay at Site 2 was the only COA overlay section that was deliberately prevented from bonding to the underlying asphalt.

To gain further insight into how bond condition affected the performance of overlays in this study, results obtained from the conventional COA overlay sections were compared with those from the COC–U overlay sections and the COA overlay section at Site 2 with the geotextile separation layer. This analysis provided an opportunity to study the difference between bonded and unbonded overlays and how bonding affected the performance of COA–U overlays that are not necessarily designed to rely on bond condition.

4.2.1. Joint LTE

Tables 36 through 38 summarize the average values for deflection in the loaded slab and joint LTE obtained at each site, organized by type of overlay. The average joint LTE for the COA–B overlay sections was 87.2%, the average joint LTE for the conventional COA–U overlay sections was 83.7%, and the average joint LTE for the COC–U overlay sections plus the COA overlay with the geotextile separation layer dropped to 44.9%. Deflection trends mirrored those of joint LTE. The average deflection in the loaded slab was 6.73 mils in the COA–B overlay sections, the average deflection in the loaded slab was 5.29 mils in the COA–U overlay sections, and the average deflection in the loaded slab increased to 13.7 in the COC–U overlay sections plus the COA section with the geotextile separation layer.

Table 35. Joint LTE results for COA–B overlays

Site	Test Date	Air Temp (°F)	Thickness (in.)	Transverse Joint Spacing (ft)	Fibers	d_l (mils)	Average Joint LTE (%)
4A	10/23/2023	66	4	6	No	5.62	90.5
4B	10/23/2023	65	4	12	No	7.62	87.9
4C	10/23/2023	65	4	15	No	6.47	87.0
4D	10/23/2023	66	4	20	No	6.86	86.4
4E	10/24/2023	61	4	20	Yes	8.13	88.6
4F	10/24/2023	62	4	15	Yes	7.42	82.9
4G	10/24/2023	61	4	12	Yes	6.80	85.2
4H	10/24/2023	63	4	6	Yes	4.93	88.8
Average						6.73	87.2

Table 36. Joint LTE results for conventional COA–U overlays

Site	Test Date	Air Temp (°F)	Thickness (in.)	Transverse Joint Spacing (ft)	Fibers	d_l (mils)	Average Joint LTE (%)
1	10/23/2023	56	6	12	Yes	4.58	82.9
4I	10/24/2023	64	6	6	Yes	3.92	91.3
4J	10/24/2023	65	6	12	Yes	4.69	82.6
4K	10/24/2023	64	6	15	Yes	5.21	83.7
4L	10/24/2023	64	6	20	Yes	5.66	83.5
4M	10/24/2023	66	6	20	No	6.40	84.0
4N	10/24/2023	65	6	15	No	5.58	86.8
4O	10/24/2023	65	6	12	No	5.96	88.0
4P	10/24/2023	65	6	6	No	5.37	92.1
5	10/23/2023	60	6	12	Yes	5.11	85.3
7A	11/1/2023	45	6	6	No	3.03	88.4
7B	11/1/2023	44	6	15	Yes	6.90	61.2
7C	11/1/2023	44	6	12	Yes	6.45	77.8
7D	11/1/2023	45	6	9	Yes	6.77	77.4
7E	11/1/2023	47	6	9	Yes	5.10	86.9
7F	11/1/2023	47	6	6	Yes	3.86	87.6
Average						5.29	83.7

Table 37. Joint LTE results for COC–U overlays and COA overlay with geotextile

Site	Test Date	Air Temp (°F)	Thickness (in.)	Transverse Joint Spacing (ft)	Fibers	d_l (mils)	Average Joint LTE (%)
2	10/23/2023	57	6	12	Yes	13.5	47.8
6A	11/8/2023	54	6	11	No	9.93	41.7
6B	11/8/2023	54	6	5.5	Yes	11.0	66
6C	11/8/2023	53	6	11	Yes	11.0	47.1
6D	11/8/2023	55	6	15	Yes	16.2	44.2
6E	11/8/2023	53	6	20	Yes	12.9	51.1
6F	11/8/2023	54	6	30	Yes	14.9	37.1
6G	11/8/2023	53	6	40	Yes	14.8	31.7
6H	11/8/2023	54	6	40	No	17.8	36.6
6I	11/8/2023	55	6	30	No	11.3	43.8
6J	11/8/2023	54	6	20	No	14.1	35.8
6K	11/8/2023	54	6	11	No	16.8	35.1
6L	11/8/2023	55	6	5.5	No	10.6	65.2
Average						13.7	44.9

To analyze these differences, t-tests were performed to compare the mean LTE values of the COA–B and conventional COA–U overlays to each other, as well as to compare all conventional COA overlays to the group of COC–U overlays plus the COA overlay with the geotextile. Tables 39 and 40 show the results of the t-tests.

Table 38. Comparison of average joint LTE for COA–B and COA–U overlays

	COA–B Overlays	COA–U Overlays
Mean Joint LTE (%)	87.2	83.7
Variance	5.58	52.6
Observations	8	16
t-statistic	2.07	
p-value	0.208	

Table 39. Comparison of average joint LTE for conventional COA overlays and COC–U overlays and COA with geotextile

	Conventional COA Overlays	COC–U Overlays and COA with Geotextile
Mean Joint LTE (%)	85.9	44.9
Variance	38.8	117
Observations	24	13
t-statistic	2.03	
p-value	3.17×10^{-16}	

The results of this analysis showed that the difference in average joint LTE between the COA–B and COA–U overlay sites was not significant to a 95% probability, with a *p-value* of greater than 0.05. However, the analysis did find a significant difference in the average joint LTE between all of the conventional COA overlay sites and the group of COC–U overlay sites plus the COA overlay with the geotextile, with a *p-value* of less than 0.05.

Overall, the average joint LTE values were similar for all COA overlay sections in this study, whether or not they were designed to bond to the underlying asphalt. Additionally, the average joint LTE values for all COA overlays were significantly greater than those of the COC–U overlay sections, as well as the COA overlay section that was deliberately unbonded with a geotextile separation layer. These findings indicate that bonding to the underlying asphalt layer provides a benefit to load transfer in COA overlays.

Comparing the results of Site 1, Site 2, and Site 4J provides particularly good insight into this behavior. These overlays have essentially the same structural design, a 6 in. PCC overlay of a composite pavement (3 in. HMA over 7 in. PCC) with 12 ft joint spacing, 4 lb/yd^3 fiber reinforcement, and similar traffic volumes. The average joint LTE values at Site 1 (82.9%) and Site 4A (82.6%) were much higher than those at Site 2 (47.8%). The only difference between the structure of these sections was the presence of the geotextile separation layer at Site 2 that ensured that the overlay would not bond to the underlying asphalt. These findings also suggest that the overlays at Site 1 and Site 4J are well bonded to the asphalt, even though they were not designed as bonded overlays.

It is concerning that the COC–U overlay sections and the COA overlay with a geotextile had such poor average joint LTE values just 5 to 6 years after construction. These findings indicate that the overlays at Site 2 and Site 6 may be under-designed relative to the traffic volume and could be prone to developing faulting in the future. These findings also suggest that COC–U overlays with a geotextile separation layer may need dowel bars to be able to achieve the same LTE as COA overlays at the same thickness or need to be designed thicker than a COA overlay to achieve the same load transfer performance at a given traffic volume.

4.2.2. FWD Backcalculation

Figure 88 plots the average backcalculated effective thickness at each site. This figure is similar to Figure 57, except in this case the columns in the chart distinguish between the overlay design thickness in blue and the portion of the effective thickness that exceeds the design thickness in orange. Presenting the data in this way helps make clear how much the underlying structure at each site contributes to the total backcalculated effective thickness. Table 41 lists these values along with the average maximum deflection, d_0, measured underneath the load plate at each center slab test.

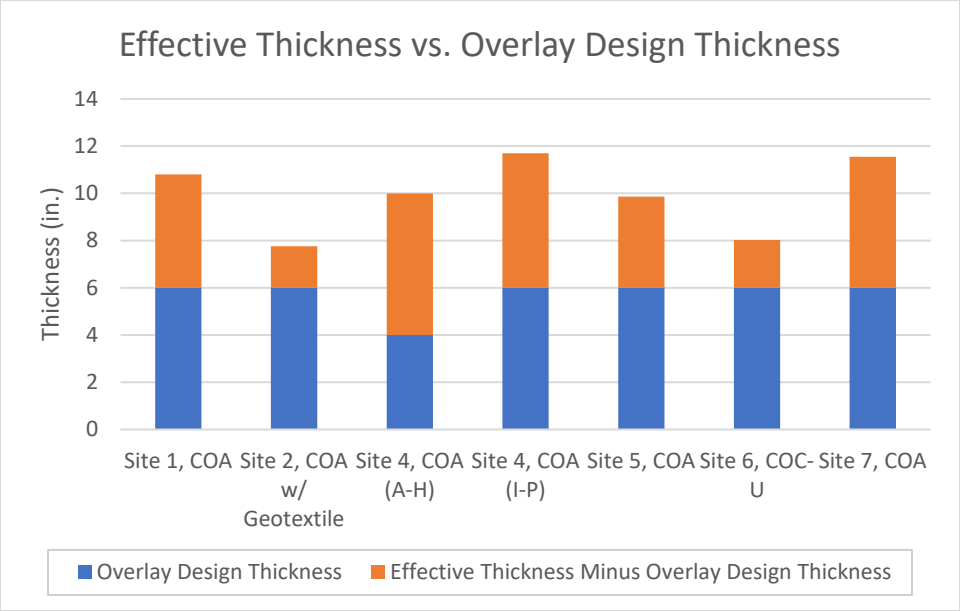

Figure 88. Effective thickness at each test site, including contribution from underlying layer

Table 40. Effective thickness at each test site, including contribution from underlying layer

Site	Overlay Type	Overlay Design Thickness (in.)	Effective Thickness Minus Overlay Design Thickness (in.)	Maximum Deflection, D_0 (mils)
1	COA–U	6	4.8	3.91
2	COA–U w/ Geotextile	6	1.8	7.92
4A-4H	COA–B	4	6.0	5.38
4I-4P	COA–U	6	5.7	3.79
5	COA–U	6	3.9	3.86
6 (All)	COC–U	6	2.0	7.63
7 (All)	COA–U	6	5.6	3.90

As previously discussed in Section 3.5, the total backcalculated effective thickness values at Site 1, Site 4, Site 5, and Site 7 exceeded the design concrete overlay thickness by large margins, from 3.9 in. to 6.0 in., depending on the project. These findings indicate a significant contribution from the underlying layer to the structural response of the overlay. By contrast, the total backcalculated effective thickness values at Site 2 and Site 6 exceeded the design thickness by just 1.7 in. and 2.0 in., respectively.

Trends in average maximum deflection values, d_0, between each set of projects were similar. Deflection values at Site 1, Site 4, Site 5, and Site 7 ranged from 3.79 mils to 5.38 mils. Meanwhile, average deflection values measured at Site 2 and Site 6 were much higher, measuring 7.92 mils and 7.63 mils, respectively. Overall, it is clear that the underlying asphalt in the conventional COA overlay sections made substantial contributions to the structure of the

overlay system, and these contributions were similar regardless of whether the overlay was designed as a COA–B overlay or COA–U overlay. The overlays at Site 2 and Site 6 that were deliberately debonded from the underlying pavement layers experienced more deflection and had a lower effective thickness than COA projects with the same overlay thickness.

4.2.2.1. Smoothness and Curling/Warping Behavior

Any differences in smoothness or curling/warping behavior between the COA and COC–U sections were also of interest for this study. However, the extensive diamond grinding that was performed after construction at Site 6 had a significant confounding effect on IRI and Curvature IRI at those sections. It can also be difficult to compare smoothness and curling/warping behavior between projects built at different locations due to the influence of weather conditions at the time of construction on built-in curling and warping behavior, which previous studies of pavements in Iowa have shown can have significant effects (Tian et al. 2023). It is much easier to analyze differences in smoothness and curling/warping behavior between test sections built at the same location at the same time of year, which was true of the analysis of Sites 4, 6, and 7 in Section 4.1.

4.2.3. Summary of Findings

Comparing the results from FWD testing for both characterization of joint LTE and backcalculated structural response, it is clear that bonding between the concrete and asphalt layers in the conventional COA overlays enhanced joint LTE performance and contributed to the structure of the overlay system. These effects were similar regardless of whether the overlay was designed to bond to the underlying asphalt (COA–B) or designed without the deliberate intent to bond to the underlying asphalt (COA–U). Meanwhile, the COC–U overlays and COA overlays that were deliberately debonded from the underlying asphalt via geotextile separation layer did not benefit from these same effects. Overall, these results indicate that the overlays at Site 2 (COA–U with geotextile) and Site 6 (COC–U) were not performing as well under traffic as the conventional COA sections with the same overlay thickness and similar traffic volumes.

4.3. Joint Activation and Overlay Performance

Past research (Gross et al. 2019) and the results of this study in Section 3.3 have found that joints sometimes do not activate in concrete overlays, especially in overlays with a 6 ft or shorter transverse joint spacing design. As discussed in Section 3.3, all of the overlay sections in this study with a joint spacing of 5.5 to 6 ft had unactivated joints. Given the variety of other measurements taken at these sections related to concrete overlay performance, this study provided a good opportunity to investigate whether unactivated joints affected the performance of the concrete overlay sections and whether there were any signs of dominant joint behavior.

As discussed in Section 3.4, FWD testing to measure joint LTE found several projects with significant variation in LTE between adjacent joints. For example, the joint-by-joint LTE results at Site 1 (Figure 39), Site 6B (Figure 45), and Site 6L (Figure 46) exhibited a characteristic “up-

and-down" pattern. Each of these three sites was also found to have unactivated transverse joints, with activation rates of 40% at Site 1, 80% at Site 6B, and 70% at Site 6L. This variation in LTE values from slab to slab could be a sign that the activated joints had to open more widely to compensate for unactivated joints, effectively behaving as dominant joints. Since they open more widely, dominant joints tend to have reduced aggregate interlock and reduced load transfer.

Meanwhile, there were no signs of dominant joint behavior in the other sections in this study with joint activation rates of less than 100%. These sites (Sites 2, 4A, 4H, 4I, 4P, 7A, and 7F) did not exhibit the same "up-and-down" trend in joint LTE. In fact, despite joint activation rates ranging from 40% to 70% at Sites 4A, 4H, 4I, and 4P, the average joint LTE values in each of these four sections were excellent, ranging from 88.8% to 92.1%.

To better understand the extent to which unactivated joints might contribute to variation in LTE and/or poor load transfer performance, Figure 89 plots the average joint LTE at each overlay site versus the standard deviation of the joint LTE measured from the 10 drops at each joint. Data points are distinguished based on whether the site had 100% joint activation (blue) or less than 100% joint activation (orange).

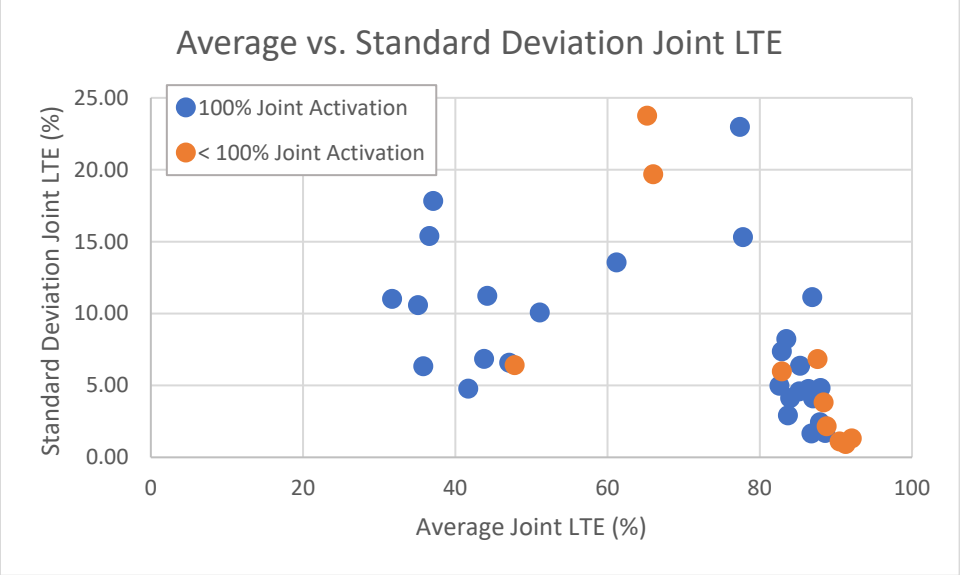

Figure 89. Average versus standard deviation of joint LTE at each site

There does not appear to be any notable differences in the behavior of projects with full joint activation and projects with less than 100% joint activation in Figure 89. Overlays with a higher average joint LTE generally had a lower standard deviation, which held true for both sets of projects. There were examples in both sets of projects of overlays with poor joint LTE and high standard deviations. That said, a joint activation rate of less than 100% did not appear to predict poor joint LTE. In fact, the worst-performing projects in this study in terms of LTE all had 100% joint activation rates.

Ultimately, the presence of unactivated joints in this study was not necessarily a sign of dominant joint behavior, nor did it predict poor results for joint LTE. Based on these findings, it does not appear that the potential for unactivated joints needs to be a concern that would affect the selection of a joint spacing design for concrete overlays.

4.4. Predicted Performance vs. Results

Each of the concrete overlay test sites was seven years old or less at the time of this report, so the 40-year predicted performance results from Section 3.1 were not expected to match measurements taken in the field. That said, analysis of trends in predicted and observed performance of the various sections led to some interesting observations.

4.4.1. Sites 1, 2, and 5

The design modules used to predict performance at Sites 1 and 5 predicted very little cracking or faulting in these sections, and no distresses were observed to date in either of those sections. The UNOL design tool predicted 20.8% slab cracking at Site 2 at 40 years, but minimal faulting. While it does not have any cracking to date, the poor joint LTE values measured at Site 2 at such an early age are a sign that faulting may develop in the future.

4.4.2. Site 4

First, it should be noted that the most prevalent distress observed at Site 4, longitudinal cracking, did not appear to be related to the performance of the overlay under traffic. As mentioned in Section 3.2.1 and shown in Figure 34, this longitudinal cracking closely resembled longitudinal cracking that was present in the existing asphalt surface prior to overlay. These longitudinal cracks also appeared within the overlay's first year of service. These pieces of evidence indicate that these longitudinal cracks are likely reflective cracks. While longitudinal reflective cracking is undesirable, it is not currently a performance concern for this overlay, and it is a good sign that fiber reinforcement has helped hold the cracks tighter relative to the sections with plain concrete.

Beyond longitudinal cracking, the most prevalent distress type at Site 4 was corner cracking. The percentage of slabs with corner cracking observed in the 4 in. sections with 12 ft joint spacing or greater at Site 4 already exceeded the percentage of total slabs cracked predicted to occur in 40 years by the PMED design runs. BCOA-ME predicted much higher levels of cracked slabs than PMED for these Site 4 sections. Performance should continue to be monitored to track the future levels of slab cracking at Site 4.

While the type and predicted levels of cracking were very different, both the BCOA-ME and PMED design modules predicted greater amounts of cracking at Site 4 in the sections with lower thicknesses, longer joint spacing designs, and no fibers. These predicted trends appear to correlate well with observed cracking trends to date, though again, the levels of cracking and types of cracking present at Site 4 to date were not very high.

4.4.3. Site 6

The most notable distress to date at Site 6 was that nearly 100% of the slabs in the sections with 30 ft and 40 ft joint spacing experienced mid-slab transverse cracking. PMED did not predict this cracking, but as discussed in Section 3.1.3, it is likely that PMED is not able to model these unusual joint spacing designs very well. (The UNOL design module does not even consider transverse joint spacing designs greater than 15 ft.) This mid-slab cracking was characteristic of slabs designed with too-long joint spacing. Notably, there was only one mid-slab transverse crack in the fiber-reinforced sections with 30 ft and 40 ft joint spacings. This finding indicates that fiber reinforcement can potentially extend concrete overlay joint spacing to these limits without the occurrence of mid-panel cracks.

Like at Site 2, the UNOL design module predicted minimal faulting at Site 6, despite the fact that consistently low joint LTE values were observed to date. PMED predicted 40-year faulting values between 0.070 and 0.090 in., with generally increasing faulting with increasing joint spacing.

4.4.4. Site 7

The distresses predicted at Site 7 by both PMED and BCOA-ME were minimal, and no distresses have been observed to date. In general, both design procedures predicted more cracking in sections with longer joint spacing designs and without fibers.

4.5. Sensitivity of Smoothness and Curling/Warping to Seasonal and Diurnal Effects

High-speed profiler testing found very little sensitivity in IRI or Curvature IRI to the season or time of day of testing. At most of the concrete overlay test sites, the range of IRI and Curvature IRI values obtained across all six measurements was less than 10 in./mi. The small number of projects that did exhibit larger ranges of IRI and Curvature IRI values across different seasons and times of day (e.g., sites with transverse joint spacing of 6 ft or less) tended to be the projects that had the highest roughness or curvature-related roughness on average to begin with. Ultimately, these findings suggest that built-in curling and warping was a more significant factor in the roughness and curvature-related roughness of these concrete overlay test sites than seasonal or diurnal effects.

5. CONCLUSIONS

This study carried out a field investigation into the performance of six FRC overlay projects that have been constructed in Iowa in recent years. These projects included COA overlays, including projects specifically designed to bond to the underlying asphalt (COA–B overlays) as well as those without consideration of the bond to the underlying asphalt (COA–U overlays), a COC–U overlay, and a COA overlay with a geotextile separation layer that ensured that it did not bond to the underlying asphalt. Several of these projects included test sections with varying thickness and joint spacing designs and with and without fiber reinforcement.

The investigation was wide-ranging, including tests that characterized many aspects of pavement performance and properties that have not previously been employed to study FRC overlays. Methods included modeling to predict performance, visual distress surveys, ultrasonic tomography to measure joint activation, FWD testing to characterize joint LTE and backcalculate structural properties, and high-speed profiling to measure pavement smoothness and characterize curling and warping behavior.

The following were the key findings of this investigation:

- Most of the overlay sections have yet to develop any distresses related to traffic loading. Where cracking occurred at Site 4 and Site 6, cracking rates were lower in fiber-reinforced sections compared to sections that did not contain fibers. The most common distress that was observed at Site 4 was corner cracking.
- Fibers may be able to extend joint spacing beyond commonly accepted design limits for concrete overlays if desired, as fiber reinforcement prevented mid-slab transverse cracking in overlays with joint spacing designs of 30 ft and 40 ft.
- Beyond cracking performance, the overlay sections containing fiber reinforcement have not demonstrated significant differences to date in LTE, pavement smoothness, or curling and warping behavior relative to the sections that did not contain fibers.
- Decreasing transverse joint spacing from longer joint spacing designs (i.e., 11 ft or greater) to shorter joint spacing designs (e.g., 5.5 to 6 ft) generally improved LTE in the overlay sections, although the magnitude of these differences was not large at all test sites.
- Pavement smoothness and curling/warping behavior were generally not affected by thickness or joint spacing design. While the highest average IRI and Curvature IRI values measured at most of the test sites occurred in overlays with shorter joint spacing designs (e.g., 5.5 to 6 ft), the difference between these values and the average values for other joint spacing designs were only statistically significant in a limited number of cases.
- The load transfer performance in the conventional COA sections was significantly better than in the COC–U overlay sections and the COA overlay section with a geotextile separation layer, including in sections that had the same overlay thickness and similar traffic volumes. The conventional COA sections also demonstrated enhanced structural capacity and lower deflection under loading. These trends were true both for the COA overlays designed as bonded (COA–B) overlays and for the COA overlays designed as unbonded (COA–U) overlays, indicating that both sets of overlay projects benefitted from bonding to the underlying asphalt.

- The COC–U overlay sections and the COA overlay with a geotextile separation layer demonstrated poor load transfer performance just five to six years after construction.
- It is important to note that the poor performance of the COC–U overlay sections and the COA overlay with a geotextile separation layer should not be interpreted to conclude that geotextile separation layers were inadequate or are a poor choice for concrete overlays. Rather, the disparate performance outcomes between these overlay sections and the conventional COA overlays was a consequence of the nature of the bonded system versus the unbonded systems for the overlays included in this study.
- Unactivated joints were present in each of the overlay sections with shorter joint spacing designs (e.g., 5.5 to 6 ft), with joint activation rates ranging from 40% to 80%. With just a couple of exceptions, joint activation rates were 100% for the rest of the sections with joint spacings of 9 ft or greater. However, the presence of unactivated joints did not predict poor performance in terms of LTE.

These findings could have a number of implications for the design of concrete overlays in the future, including the following:

- Fibers did not appear to provide performance benefits to concrete overlays at the dosage rate (4 lb/yd^3) used in this study in terms of load transfer, smoothness, or curling/warping behavior at early ages, three to seven years after construction. It does not appear that these factors need to be considered in the design of FRC overlays unless these benefits are realized at later ages or unless they can be realized at higher dosage rates.
- While overlays with shorter joint spacing designs (e.g., 5.5 to 6 ft) in this study did not achieve joint activation rates of 100%, unactivated joints did not correlate with any performance issues. The overlays with shorter joint spacing designs also generally demonstrated improved LTE. There does not appear to be any reason for concerns about unactivated joints to guide the selection of concrete overlay joint spacing design.
- Regardless of whether the COA overlays in this study were designed as bonded overlays (COA–B) or without the intention to bond to the underlying asphalt layer (COA–U), all of the COA overlays demonstrated improved load transfer and enhanced structural response under loading relative to COC–U overlays and the COA overlay that contained a geotextile separation layer that ensured that it did not bond to the underlying asphalt. The benefits of bonding to the underlying asphalt layer should be considered in the design of all COA overlays, and the distinction between COA–B and COA–U overlays may not be useful or meaningful in practice.

REFERENCES

AASHTO. 1993. *AASHTO Guide for Design of Pavement Structures.* American Association of State Highway and Transportation Officials, Washington, DC.

AASHTO. 2008. *Mechanistic-Empirical Pavement Design Guide: A Manual of Practice*. American Association of State Highway and Transportation Officials, Washington, DC.

ACI. 2008. *Guide for Specifying, Proportioning, and Production of Fiber-Reinforced Concrete*. American Concrete Institute, Farmington Hills, MI.

ACI. 2018. *Guide to Design with Fiber-Reinforced Concrete*. American Concrete Institute, Farmington Hills, MI.

Alhasan, A. 2018. Characterizing the Impact of Curling and Warping on Ride Quality. Road Profile Users' Group, September 18–21, Rapid City, SD. https://rpug.org/download/2018/6.5-Ahmad%20Alhasan.pdf.

ARA. 2016. *Integrating the Bonded Concrete Overlay of Asphalt (BCOA-ME) Design Procedure into the AASHTOWare Pavement ME Software*. Applied Research Associates, Albuqurque, NM.

ASTM. 2021. *Standard Practice for Computing International Roughness Index of Roads from Longitudinal Profile Measurements*. ASTM International, West Conshohocken, PA.

Barenberg, E., and A. Ioannides. 1989. *Structural Evaluation of Concrete Slabs Using Falling Weight Deflectometer Results*. Advanced Construction Technology Center, Urbana, IL.

Barman, M., and B. Hansen. 2018. *Comparison of Performances of Structural Fibers and Development of Specification for Using Them in Thin Concrete Overlays*. Local Road Research Board, Minnesota Department of Transportation, St. Paul, MN.

Barman, M., S. Roy, A. Tiwari, and T. Burnham. 2021. Influence of Structural Synthetic Fibers on the Transverse Joint Behavior and Faulting of Ultra-Thin and Thin Concrete Pavements. 100th Annual Transportation Research Board Meeting, January 26.

Bordelon, A., and J. Roesler. 2012. Design with Fiber Reinforcement for Thin Concrete Overlays Bonded to Asphalt. *Journal of Transportation Engineering*, Vol. 138, No. 4.

Byrum, C. 2000. Analysis by High-Speed Profile of Jointed Concrete Pavement Slab Curvatures. *Transportation Research Record*, Vol. 1730, pp. 1–9.

Ceylan, H., S. Yang, K. Gopalakrishnan, S. Kim, P. Taylor, and A. Alhasan. 2016. *Impact of Curling and Warping on Concrete Pavement*. Institute for Transportation, Iowa State University, Ames, IA.

Chang, G., S. Karamihas, R. Rasumssen, D. Merritt, and M. Swanlund. 2008. Quantifying the Impact of Jointed Concrete Pavement Curling and Warping on Pavement Uneveness. *Proceedings of the 6th Symposium on Pavement Surface Characteristics*, Potoroz, Slovenia.

Choubane, B., and M. Tia. 1995. Analysis and Verification of Thermal-Gradient Effects on Concrete Pavement. *ASCE Journal of Transportation Engineering*, Vol. 121, No. 1, pp. 75–81.

Crovetti, J. 1994. Design and Evaluation of Jointed Concrete Pavement Systems Incorporating Free Draining Base Layers. PhD dissertation. University of Illinois at Urbana-Champaign, IL.

Federal Register. 2017. *National Performance Management Measures; Assessing Performance of the National Highway System, Freight Movement on the Interstate System, and Congestion Mitigation and Air Quality Improvement Program*. Federal Highway Administration, Washington, DC.

Ferrebee, E., A. Gieraltowski, and G. Voigt. 2018. Creation and Development of PavementDesigner.org – A Unified Industry-Wide Pavement Design Tool for Concrete and Cement-Based Solutions. *Proceedings of the 13th International Symposium on Concrete Roads*, Berlin, Germany, June 19–22.

Fick, G., J. Gross, M. Snyder, D. Harrington, and T. Cackler. 2021. *Guide to Concrete Overlays*. Fourth Edition. National Concrete Pavement Technology Center, Iowa State University, Ames, IA.

Gross, J., D. King, D. Harrington, H. Ceylan, Y. Chen, S. Kim, P. Taylor, and O. Kaya. 2017. *Concrete Overlay Performance on Iowa's Roadways*. National Concrete Pavement Technology Center, Iowa State University, Ames, IA.

Gross, J., D. King, H. Ceylan, Y. Chen, and P. Taylor. 2019. *Optimizing Joint Spacing for Concrete Overlays with and without Structural Fiber Reinforcement*. National Concrete Pavement Technology Center, Iowa State University, Ames, IA.

Hall, K., M. Darter, T. Hoerner, and L. Khazanovich. 1997. *LTPP Data Analysis Phase I: Validation of Guidelines for k-value Selection and Concrete Pavement Performance Prediction*. ERES Consultants, Champaign, IL.

Ioannides, A. 1990. Dimensional Analysis in NDT Rigid Pavement Evaluation. *Journal of Transportation Engineering*, Vol. 116, No. 1, pp. 23–36.

Karamihas, S., T. Gillespie, S. Kohn, and R. Perera. *Guidelines for Longitudinal Pavement Profile Measurement*. University of Michigan Transportation Research Institute, Ann Arbor, MI.

Khazanovich, L., and A. Gotlif. 2003. *Evaluation of Joint and Crack Load Transfer, Final Report*. Office of Infrastructure Research and Development, Federal Highway Administration, Washington, DC.

Khazanovich, L, J. Vandenbossche, J. DeSantis, and S. Sachs. 2020. *Development of an Improved Design Procedure for Unbonded Concrete Overlays*. Minnesota Department of Transportation, St. Paul, MN.

Kim, M., and A. Bordelon. 2017a. *Cracking and Debonding of a Thin Fiber-Reinforced Concrete Overlay*. Mountain-Plains Consortium, University of Utah, Salt Lake City, UT.

Kim, M., and A. Bordelon. 2017b. Age-Dependent Properties of Fiber-Reinforced Concrete for Thin Concrete Overlays. *Construction and Building Materials*, Vol. 137, pp. 288–299.

King, D., and J. Roesler. 2014a. *Structural Performance of Ultra-Thin Whitetopping on Illinois Roadways and Parking Lots*. Illinois Center for Transportation, University of Illinois at Urbana-Champaign, IL.

King, D., and J. Roesler. 2014b. Backcalculation Procedure for Bonded Concrete Overlays of Asphalt Pavement. *Transportation Research Record*, Vol. 2457, No. 1, pp. 72–29.

Lenth, R. 2024. Estimated Marginal Means, aka Least-Squares Means. The Comprehensive R Archive Network. https://cran.r-project.org/package=emmeans.

Li, Z., N. Dufalla, F. Mu, and J. Vandenbossche. 2019. *Bonded Concrete Overlays of Asphalt Pavements Mechanistic-Empirical Design Guide (BCOA-ME) Theory Manual*. University of Pittsburgh, Pittsburgh, PA.

Merritt, D., G. Chang, H. Torres, K. Mohanraj, and R. Rasuussen. 2015. *Evaluating the Effects of Concrete Pavement Curling and Warping on Ride Quality*. Colorado Department of Transportation, Denver, CO.

Miller, J., and W. Bellinger. 2014. *Distress Identification Manual for the Long-Term Pavement Performance Program*. Fifth Revised Edition. Office of Infrastructure Research and Development, Federal Highway Administration, Washington DC.

Nassiri, S. 2011. Establishing Permanent Curl/Warp Temperature Gradient in Jointed Plain Concrete Pavements. PhD dissertation. University of Pittsburgh, Pittsburgh, PA.

Pierce, L., J. Bruinsma, K. Smith, M. Wade, K. Chatti, and J. Vandenbossche. 2017. *Using Falling Weight Deflectometer Data with Mechanistic-Empirical Design and Analysis, Volume III: Guidelines for Deflection Testing, Analysis, and Interpretation*. Applied Pavement Technology, Champaign, IL.

Roesler, J., A. Bordelon, A. Brand, and A. Amirkhanian. 2019. *Fiber-Reinforced Concrete for Pavement Overlays: Technical Overview*. National Concrete Pavement Technology Center, Iowa State University, Ames, IA.

Sayers, M., T. Gillespie, and C. Queiroz. 1986. The International Road Roughness Experiment: A Basis for Establishing a Standard Scale for Road Roughness Measurements. *Transportation Research Record*, Vol. 1084, pp. 76–85.

Shah, H., and J. Weiss. 2006. *Quantifying Shrinkage Cracking in Fiber-Reinforced Concrete Using the Ring Test*. *Materials and Structures*, Vol. 39, pp. 887–899.

Smith, K., and P. Ram. 2016. *Measuring and Specifying Pavement Smoothness*. Applied Pavement Technology, Champaign, IL.

Smith, K., J. Bruinsma, M. Wade, K. Chatti, J. Vandenbossche, and T. Yu. 2017. *Using Falling Weight Deflectometer Data with Mechanistic-Empirical Design and Analysis, Volume I: Final Report*. Applied Pavement Technology, Champaign, IL.

Tian, K., D. King, B. Yang, S. Kim, A. Alhasan, and H. Ceylan. 2023. *Impact of Curling and Warping on Concrete Pavement: Phase II*. Institute for Transportation, Iowa State University, Ames, IA.

Tran, Q., and J. Roesler. 2020. Rapid Detection of Concrete Joint Activation Using Normalized Shear Wave Transmission Energy. *International Journal of Pavement Engineering*, Vol. 23, No. 4, pp. 1025–1037.

Wei, Y., S. Liang, and X. Gao. 2017. Numerical Evaluation of Moisture Warping and Stress in Concrete Pavement Slabs with Different Water-to-Cement Ratio and Thickness. *Journal of Engineering Mechanics*, Vol. 143, No. 2.

Weiss, J., T. Ley, L. Sutter, D. Harrington, J. Gross, and S. Tritsch. 2016. Guide to the Prevention and Restoration of Early Joint Deterioration in Concrete Pavements. National Concrete Pavement Technology Center, Iowa State University, Ames, IA.

Westergaard, H. 1926. Computation of Stresses in Concrete Roads. *Proceedings of the 5th Annual Highway Research Board Meeting*, Vol. 5, No. 1, pp. 90–112.

Yang, B., K. Tian, D. King, H. Ceylan, and S. Kim. 2023. Assessment of the Effects of Temperature and Moisture Gradients on Curling and Warping Behavior of Jointed Plain Concrete Pavements. *Proceedings of the American Society of Civil Engineers, Airfield and Highway Pavements*, pp. 108-117. June 14–17, Austin, TX,

APPENDIX A. FULL PERFORMANCE PREDICTION RESULTS

Tables 42 through 76 list the full performance prediction results for cracked slabs, mean joint faulting, and IRI for each test site.

Table 41. Performance prediction results for Site 1

Site 1 - Worth County Highway 105, COA-U, 6 in., 12 ft x 12 ft, Fibers		
PMED - JPCP over AC (No Bond)		
Slabs Cracked (%)	Mean Joint Faulting (in.)	IRI (in./mi)
1.61	0.030	186
PMED - JPCP over AC (Bond)		
Slabs Cracked (%)	Mean Joint Faulting (in.)	IRI (in./mi)
1.14	0.030	186
BCOA-ME Design		
Slabs Cracked (%)	Mean Joint Faulting (in.)	
5.0	0.00	

Table 42. Performance prediction results for Site 2

Site 2 - Worth County Highway 105, COA-U (w/ Geotextile), 6 in., 12 ft x 12 ft, Fibers		
PMED - JPCP over AC (No Bond)		
Slabs Cracked (%)	Mean Joint Faulting (in.)	IRI (in./mi)
2.40	0.040	189
PMED - JPCP over JPCP (Unbonded)		
Slabs Cracked (%)	Mean Joint Faulting (in.)	IRI (in./mi)
1.55	0.050	172
UNOL Design		
Slabs Cracked (%)	Mean Joint Faulting (in.)	
20.8	0.0070	

Table 43. Performance prediction results for Site 4A

Site 4A - Mitchell County Highway 105, COA-B, 4 in., 6 ft x 6 ft, No Fibers	
PMED - SJPCP over AC	
Slabs Cracked (%)	
0.52	
BCOA-ME Design	
Slabs Cracked (%)	Mean Joint Faulting (in.)
17.0	0.00

Table 44. Performance prediction results for Site 4B

Site 4B - Mitchell County Highway 105, COA-B, 4 in., 12 ft x 12 ft, No Fibers	
BCOA-ME Design	
Slabs Cracked (%)	Mean Joint Faulting (in.)
63.0	0.00

Table 45. Performance prediction results for Site 4C

Site 4C - Mitchell County Highway 105, COA-B, 4 in., 15 ft x 12 ft, No Fibers	
BCOA-ME Design	
Slabs Cracked (%)	Mean Joint Faulting (in.)
85.0	0.035

Table 46. Performance prediction results for Site 4F

Site 4F - Mitchell County Highway 105, COA-B, 4 in., 15 ft x 12 ft, Fibers	
BCOA-ME Design	
Slabs Cracked (%)	Mean Joint Faulting (in.)
34.0	0.034

Table 47. Performance prediction results for Site 4H

Site 4G - Mitchell County Highway 105, COA-B, 4 in., 12 ft x 12 ft, Fibers	
BCOA-ME Design	
Slabs Cracked (%)	Mean Joint Faulting (in.)
18.0	0.00

Table 48. Performance prediction results for Site 4H

Site 4H - Mitchell County Highway 105, COA-B, 4 in., 6 ft x 6 ft, Fibers	
PMED - SJPCP over AC	
Slabs Cracked (%)	
0.52	
BCOA-ME Design	
Slabs Cracked (%)	Mean Joint Faulting (in.)
1.50	0.00

Table 49. Performance prediction results for Site 4I

Site 4I - Mitchell County Highway 105, COA-U, 6 in., 6 ft x 6 ft, Fibers	
PMED - SJPCP over AC	
Slabs Cracked (%)	
0.52	
BCOA-ME Design	
Slabs Cracked (%)	Mean Joint Faulting (in.)
0.05	0.00

Table 50. Performance prediction results for Site 4J

Site 4J - Mitchell County Highway 105, COA-U, 6 in., 12 ft x 12 ft, Fibers		
PMED - JPCP over AC (No Bond)		
Slabs Cracked (%)	Mean Joint Faulting (in.)	IRI (in./mi)
1.42	0.030	187
PMED - JPCP over AC (Bond)		
Slabs Cracked (%)	Mean Joint Faulting (in.)	IRI (in./mi)
0.10	0.030	187
BCOA-ME Design		
Slabs Cracked (%)	Mean Joint Faulting (in.)	
5.0	0.00	

Table 51. Performance prediction results for Site 4K

Site 4K - Mitchell County Highway 105, COA-U, 6 in., 15 ft x 12 ft, Fibers		
PMED - JPCP over AC (No Bond)		
Slabs Cracked (%)	Mean Joint Faulting (in.)	IRI (in./mi)
1.61	0.030	187
PMED - JPCP over AC (Bond)		
Slabs Cracked (%)	Mean Joint Faulting (in.)	IRI (in./mi)
1.14	0.030	187
BCOA-ME Design		
Slabs Cracked (%)	Mean Joint Faulting (in.)	
10.0	0.03	

Table 52. Performance prediction results for Site 4L

Site 4L - Mitchell County Highway 105, COA-U, 6 in., 20 ft x 12 ft, Fibers		
PMED - JPCP over AC (No Bond)		
Slabs Cracked (%)	Mean Joint Faulting (in.)	IRI (in./mi)
1.77	0.040	187
PMED - JPCP over AC (Bond)		
Slabs Cracked (%)	Mean Joint Faulting (in.)	IRI (in./mi)
1.14	0.040	186

Table 53. Performance prediction results for Site 4M

Site 4M - Mitchell County Highway 105, COA-U, 6 in., 20 ft x 12 ft, No Fibers		
PMED - JPCP over AC (No Bond)		
Slabs Cracked (%)	Mean Joint Faulting (in.)	IRI (in./mi)
5.26	0.040	187
PMED - JPCP over AC (Bond)		
Slabs Cracked (%)	Mean Joint Faulting (in.)	IRI (in./mi)
3.46	0.040	187

Table 54. Performance prediction results for Site 4N

Site 4N - Mitchell County Highway 105, COA-U, 6 in., 15 ft x 12 ft, No Fibers		
PMED - JPCP over AC (No Bond)		
Slabs Cracked (%)	Mean Joint Faulting (in.)	IRI (in./mi)
4.85	0.030	187
PMED - JPCP over AC (Bond)		
Slabs Cracked (%)	Mean Joint Faulting (in.)	IRI (in./mi)
3.22	0.030	187
BCOA-ME Design		
Slabs Cracked (%)	Mean Joint Faulting (in.)	
37.0	0.035	

Table 55. Performance prediction results for Site 4O

Site 4O - Mitchell County Highway 105, COA-U, 6 in., 12 ft x 12 ft, No Fibers		
PMED - JPCP over AC (No Bond)		
Slabs Cracked (%)	Mean Joint Faulting (in.)	IRI (in./mi)
3.85	0.030	187
PMED - JPCP over AC (Bond)		
Slabs Cracked (%)	Mean Joint Faulting (in.)	IRI (in./mi)
2.63	0.030	187
BCOA-ME Design		
Slabs Cracked (%)	Mean Joint Faulting (in.)	
20.0	0.00	

Table 56. Performance prediction results for Site 4P

Site 4P - Mitchell County Highway 105, COA-U, 6 in., 6 ft x 6 ft, Fibers	
PMED - SJPCP over AC	
Slabs Cracked (%)	
0.52	
BCOA-ME Design	
Slabs Cracked (%)	Mean Joint Faulting (in.)
0.8	0.00

Table 57. Performance prediction results for Site 5

Site 5 - Mitchell County Highway T26, COA-U, 6 in., 12 ft x 12 ft, Fibers		
PMED - JPCP over AC (No Bond)		
Slabs Cracked (%)	Mean Joint Faulting (in.)	IRI (in./mi)
2.02	0.040	188
PMED - JPCP over AC (Bond)		
Slabs Cracked (%)	Mean Joint Faulting (in.)	IRI (in./mi)
1.42	0.040	188
BCOA-ME Design		
Slabs Cracked (%)	Mean Joint Faulting (in.)	
2.0	0.00	

Table 58. Performance prediction results for Site 6A

Site 6A - Buchanan County Highway V62, COC-U, 6 in., 12 ft x 12 ft, No Fibers		
PMED - JPCP over JPCP (Unbonded)		
Slabs Cracked (%)	Mean Joint Faulting (in.)	IRI (in./mi)
3.40	0.070	171
UNOL Design		
Slabs Cracked (%)	Mean Joint Faulting (in.)	
23.72	0.0030	

Table 59. Performance prediction results for Site 6B

Site 6B - Buchanan County Highway V62, COC-U, 6 in., 6 ft x 6 ft, Fibers	
UNOL Design	
Slabs Cracked (%)	Mean Joint Faulting (in.)
0.79	0.0010

Table 60. Performance prediction results for Site 6C

Site 6C - Buchanan County Highway V62, COC-U, 6 in., 12 ft x 12 ft, Fibers		
PMED - JPCP over JPCP (Unbonded)		
Slabs Cracked (%)	Mean Joint Faulting (in.)	IRI (in./mi)
1.55	0.070	170
UNOL Design		
Slabs Cracked (%)	Mean Joint Faulting (in.)	
23.06	0.0040	

Table 61. Performance prediction results for Site 6D

Site 6D - Buchanan County Highway V62, COC-U, 6 in., 15 ft x 12 ft, Fibers		
PMED - JPCP over JPCP (Unbonded)		
Slabs Cracked (%)	Mean Joint Faulting (in.)	IRI (in./mi)
1.55	0.080	170
UNOL Design		
Slabs Cracked (%)	Mean Joint Faulting (in.)	
22.76	0.0070	

Table 62. Performance prediction results for Site 6E

Site 6E - Buchanan County Highway V62, COC-U, 6 in., 20 ft x 12 ft, Fibers		
PMED - JPCP over JPCP (Unbonded)		
Slabs Cracked (%)	Mean Joint Faulting (in.)	IRI (in./mi)
1.77	0.090	166

Table 63. Performance prediction results for Site 6F

Site 6F - Buchanan County Highway V62, COC-U, 6 in., 30 ft x 12 ft, Fibers		
PMED - JPCP over JPCP (Unbonded)		
Slabs Cracked (%)	Mean Joint Faulting (in.)	IRI (in./mi)
1.55	0.090	158

Table 64. Performance prediction results for Site 6G

Site 6G - Buchanan County Highway V62, COC-U, 6 in., 40 ft x 12 ft, Fibers		
PMED - JPCP over JPCP (Unbonded)		
Slabs Cracked (%)	Mean Joint Faulting (in.)	IRI (in./mi)
0.78	0.090	153

Table 65. Performance prediction results for Site 6H

Site 6H - Buchanan County Highway V62, COC-U, 6 in., 40 ft x 12 ft, No Fibers		
PMED - JPCP over JPCP (Unbonded)		
Slabs Cracked (%)	Mean Joint Faulting (in.)	IRI (in./mi)
0.78	0.090	154

Table 66. Performance prediction results for Site 6I

Site 6I - Buchanan County Highway V62, COC-U, 6 in., 30 ft x 12 ft, No Fibers		
PMED - JPCP over JPCP (Unbonded)		
Slabs Cracked (%)	Mean Joint Faulting (in.)	IRI (in./mi)
4.68	0.090	159

Table 67. Performance prediction results for Site 6J

Site 6J - Buchanan County Highway V62, COC-U, 6 in., 20 ft x 12 ft, No Fibers		
PMED - JPCP over JPCP (Unbonded)		
Slabs Cracked (%)	Mean Joint Faulting (in.)	IRI (in./mi)
4.96	0.090	167

Table 68. Performance prediction results for Site 6K

Site 6K - Buchanan County Highway V62, COC-U, 6 in., 15 ft x 12 ft, No Fibers		
PMED - JPCP over JPCP (Unbonded)		
Slabs Cracked (%)	Mean Joint Faulting (in.)	IRI (in./mi)
4.21	0.080	171
UNOL Design		
Slabs Cracked (%)	Mean Joint Faulting (in.)	
24.08	0.0070	

Table 69. Performance prediction results for Site 6L

Site 6L - Buchanan County Highway V62, COC-U, 6 in., 6 ft x 6 ft, No Fibers	
UNOL Design	
Slabs Cracked (%)	Mean Joint Faulting (in.)
6.39	0.0020

Table 70. Performance prediction results for Site 7A

Site 7A - Iowa Highway 31, COA-U, 6 in., 6 ft x 6 ft, No Fibers	
PMED - SJPCP over AC	
Slabs Cracked (%)	
0.52	
BCOA-ME Design	
Slabs Cracked (%)	Mean Joint Faulting (in.)
0.12	0.00

Table 71. Performance prediction results for Site 7B

Site 7B - Iowa Highway 31, COA-U, 6 in., 15 ft x 12 ft, Fibers		
PMED - JPCP over AC (No Bond)		
Slabs Cracked (%)	Mean Joint Faulting (in.)	IRI (in./mi)
4.60	0.060	160
PMED - JPCP over AC (Bond)		
Slabs Cracked (%)	Mean Joint Faulting (in.)	IRI (in./mi)
2.76	0.060	160
BCOA-ME Design		
Slabs Cracked (%)	Mean Joint Faulting (in.)	
1.70	0.11	

Table 72. Performance prediction results for Site 7C

Site 7C - Iowa Highway 31, COA-U, 6 in., 12 ft x 12 ft, Fibers		
PMED - JPCP over AC (No Bond)		
Slabs Cracked (%)	Mean Joint Faulting (in.)	IRI (in./mi)
3.51	0.050	160
PMED - JPCP over AC (Bond)		
Slabs Cracked (%)	Mean Joint Faulting (in.)	IRI (in./mi)
2.12	0.050	160
BCOA-ME Design		
Slabs Cracked (%)	Mean Joint Faulting (in.)	
0.80	0.00	

Table 73. Performance prediction results for Site 7D

Site 7D - Iowa Highway 31, COA-U, 6 in., 9 ft x 12 ft, Fibers		
PMED - JPCP over AC (No Bond)		
Slabs Cracked (%)	Mean Joint Faulting (in.)	IRI (in./mi)
2.63	0.050	162
PMED - JPCP over AC (Bond)		
Slabs Cracked (%)	Mean Joint Faulting (in.)	IRI (in./mi)
1.61	0.050	162
BCOA-ME Design		
Slabs Cracked (%)	Mean Joint Faulting (in.)	
0.50	0.00	

Table 74. Performance prediction results for Site 7E

Site 7E - Iowa Highway 31, COA-U, 6 in., 9 ft x 6 ft, Fibers
PMED - SJPCP over AC
Slabs Cracked (%)
0.52

Table 75. Performance prediction results for Site 7F

Site 7F - Iowa Highway 31, COA-U, 6 in., 6 ft x 6 ft, Fibers	
PMED - SJPCP over AC	
Slabs Cracked (%)	
0.52	
BCOA-ME Design	
Slabs Cracked (%)	Mean Joint Faulting (in.)
0.010	0.00

APPENDIX B. ADDITIONAL LOAD TRANSFER EFFICIENCY RESULTS

Figures 90 through 111 plot the slab-by-slab joint LTE results for each test site not included in Section 3.4.

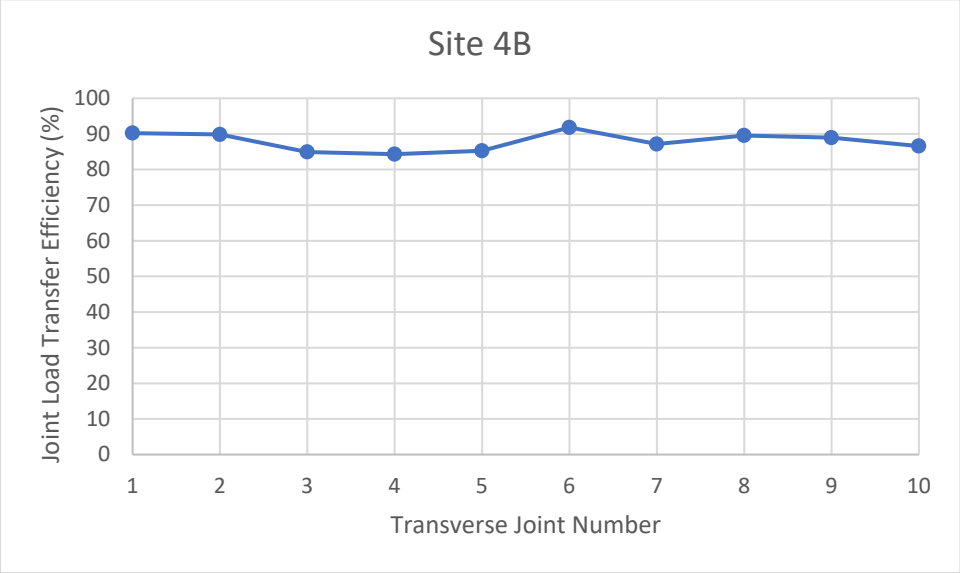

Figure 90. Joint-by-joint LTE results for Site 4B

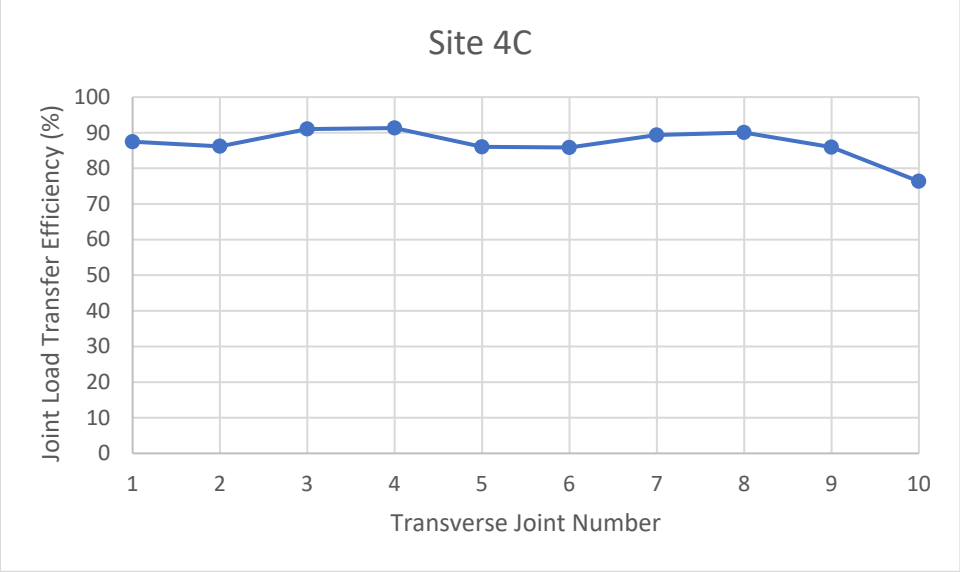

Figure 91. Joint-by-joint LTE results for Site 4C

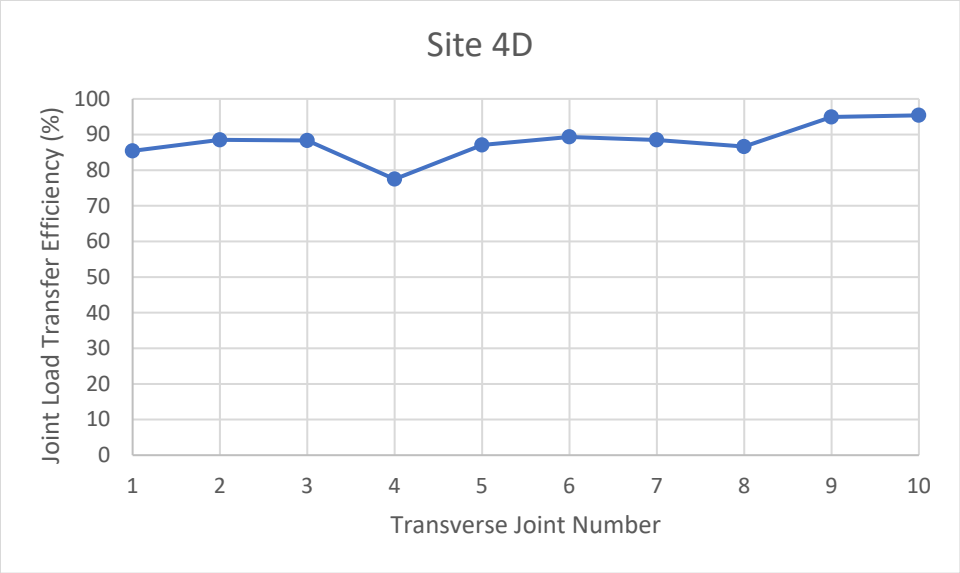

Figure 92. Joint-by-joint LTE results for Site 4D

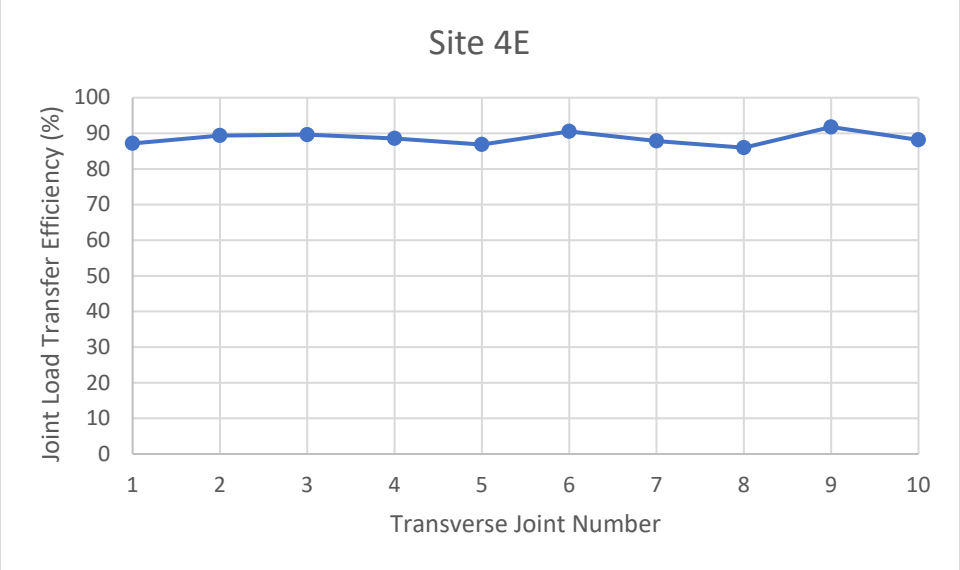

Figure 93. Joint-by-joint LTE results for Site 4E

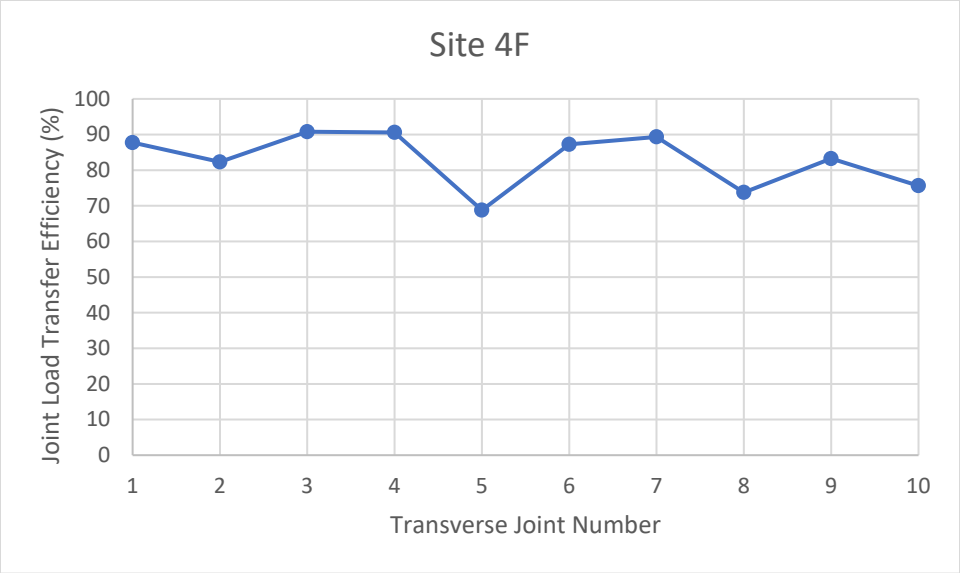

Figure 94. Joint-by-joint LTE results for Site 4F

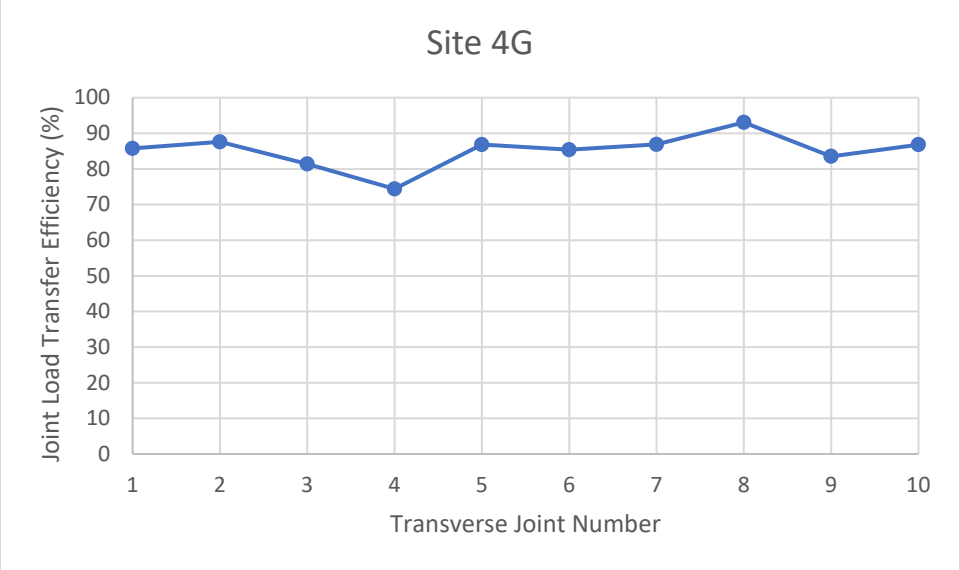

Figure 95. Joint-by-joint LTE results for Site 4G

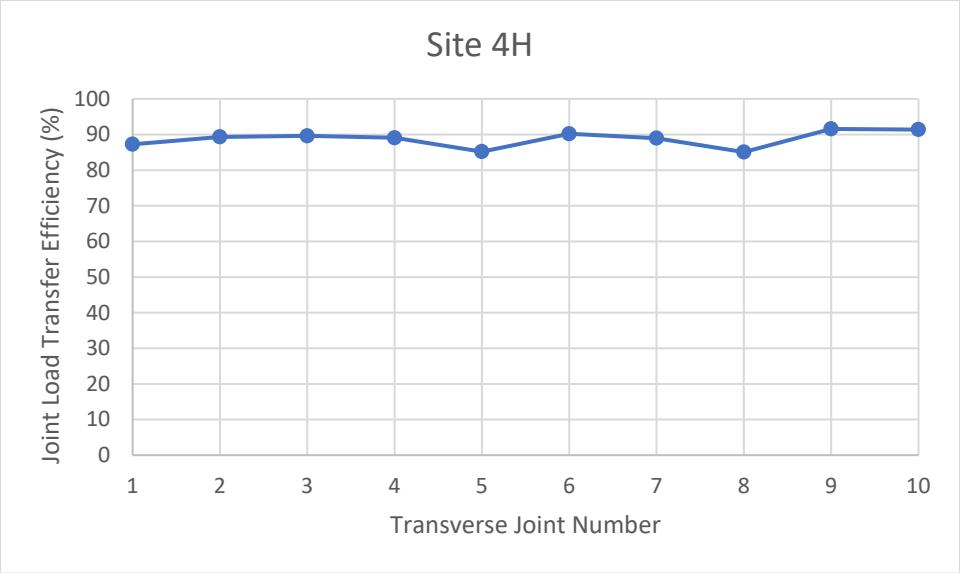

Figure 96. Joint-by-joint LTE results for Site 4H

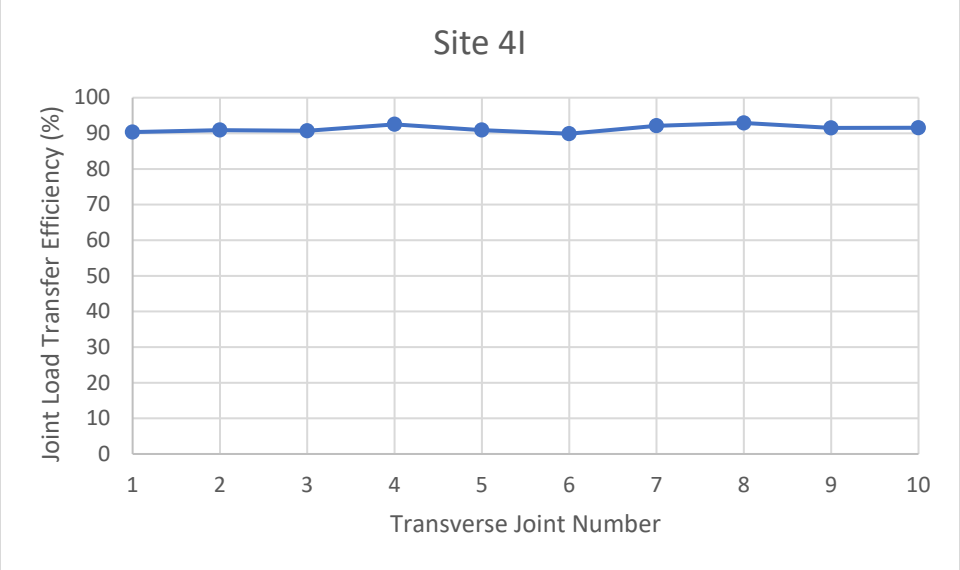

Figure 97. Joint-by-joint LTE results for Site 4I

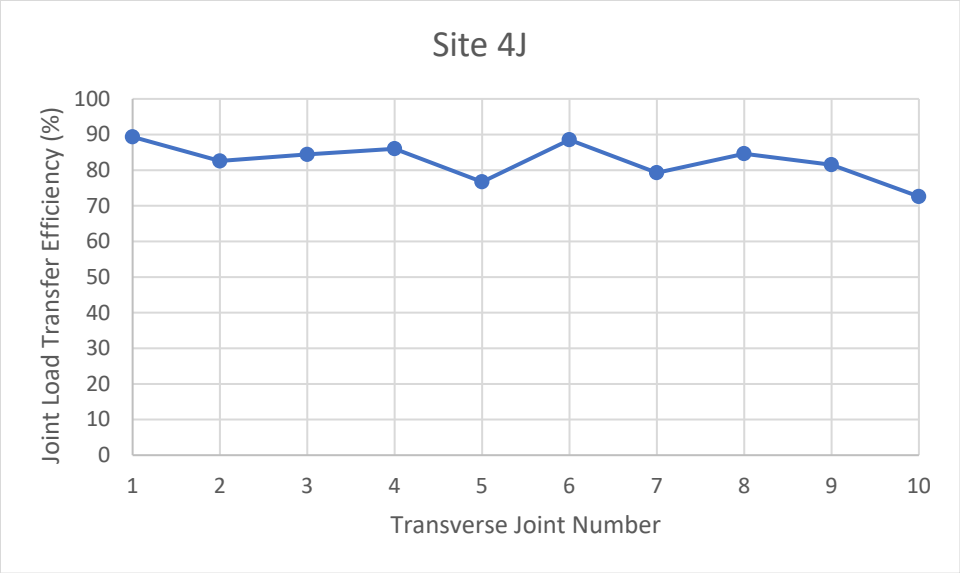

Figure 98. Joint-by-joint LTE results for Site 4J

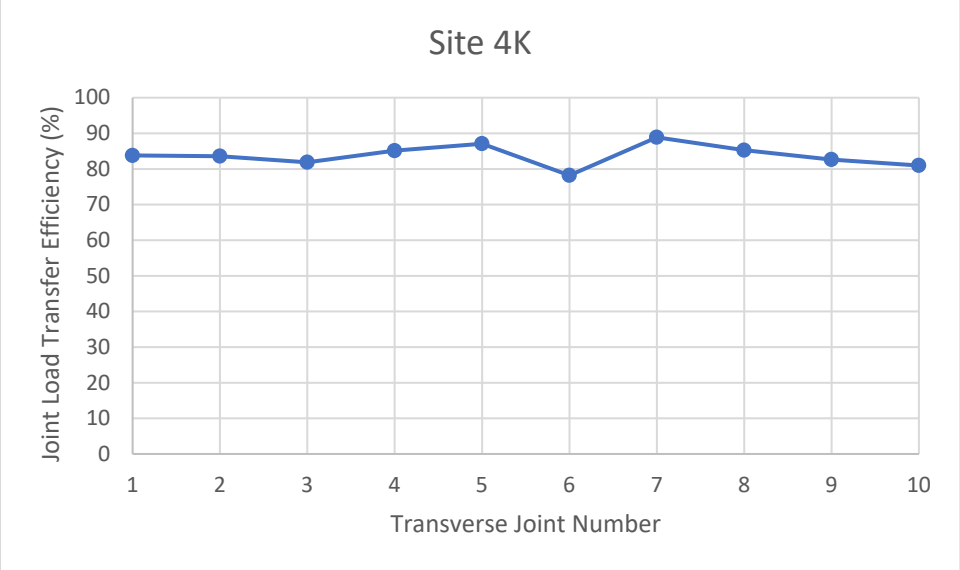

Figure 99. Joint-by-joint LTE results for Site 4K

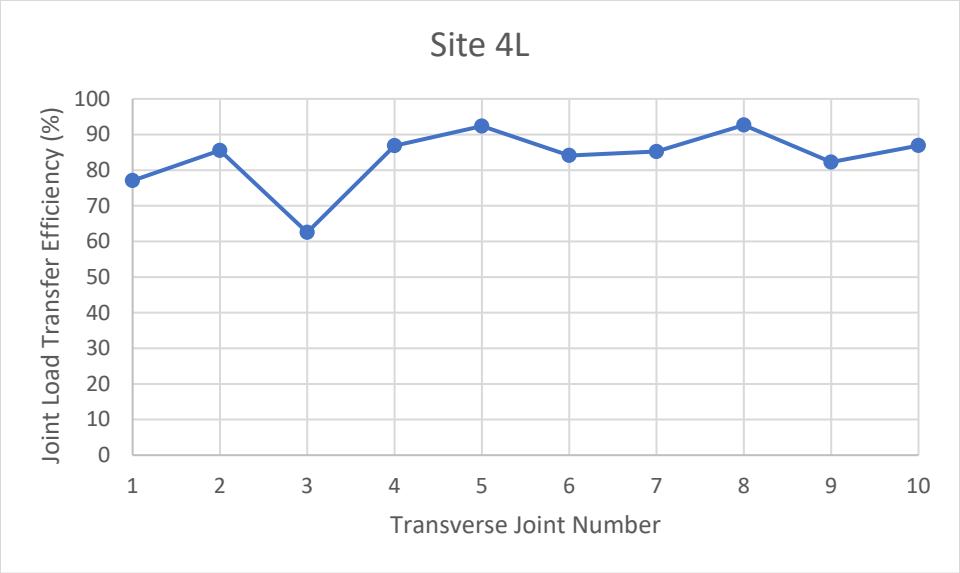

Figure 100. Joint-by-joint LTE results for Site 4L

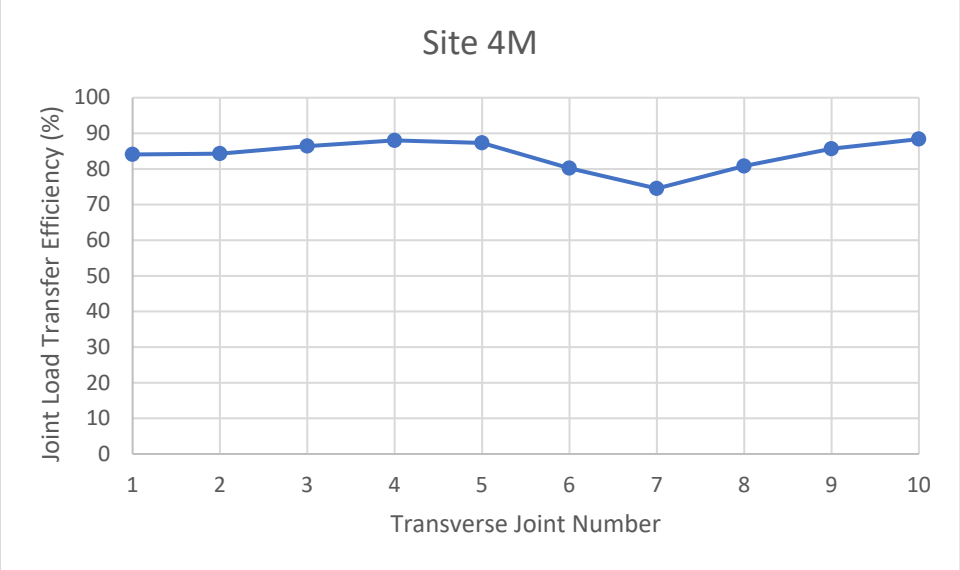

Figure 101. Joint-by-joint LTE results for Site 4M

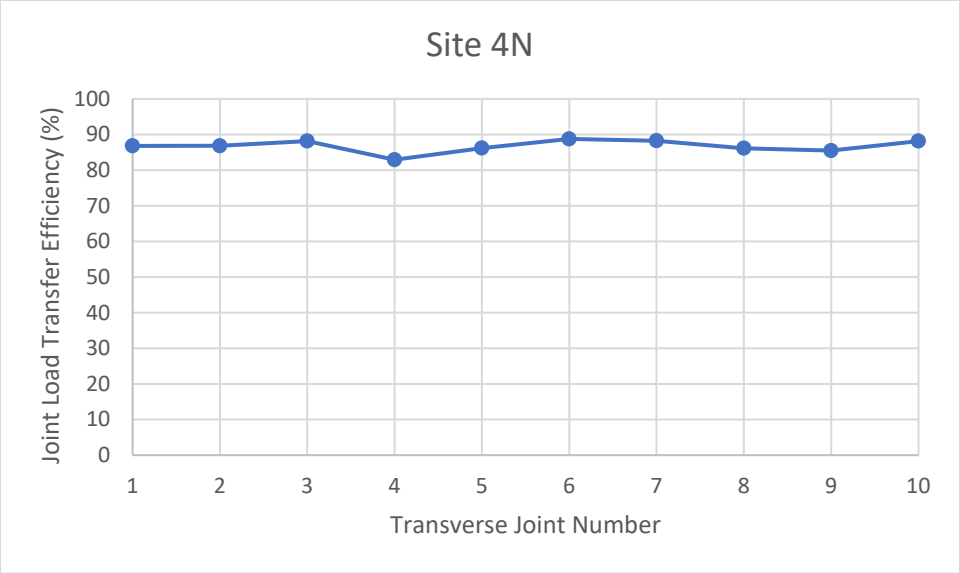

Figure 102. Joint-by-joint LTE results for Site 4N

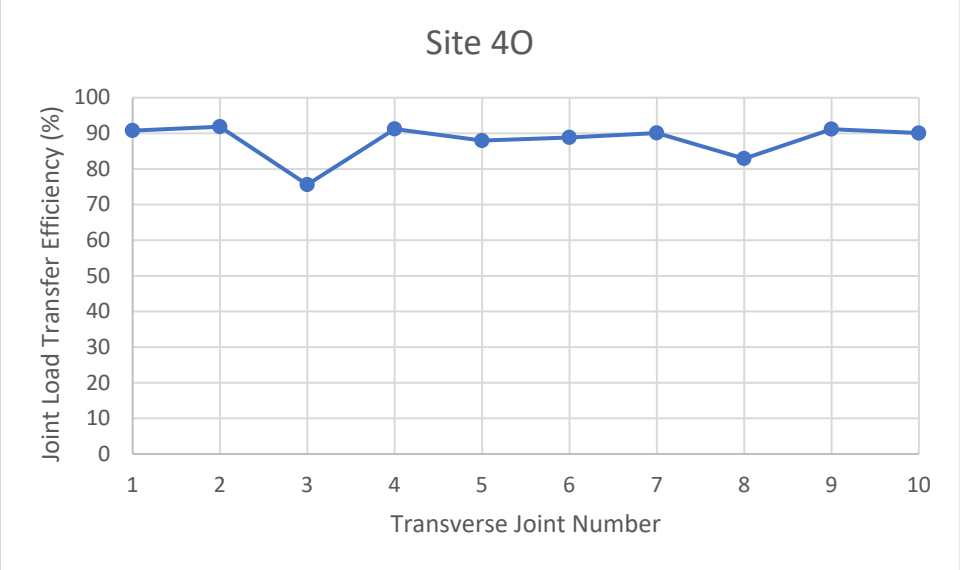

Figure 103. Joint-by-joint LTE results for Site 4O

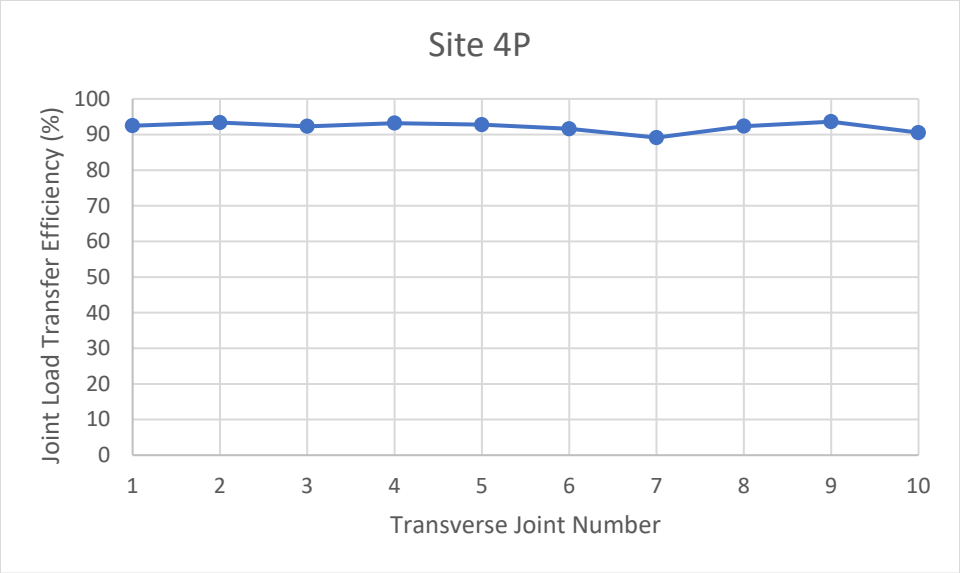

Figure 104. Joint-by-joint LTE results for Site 4P

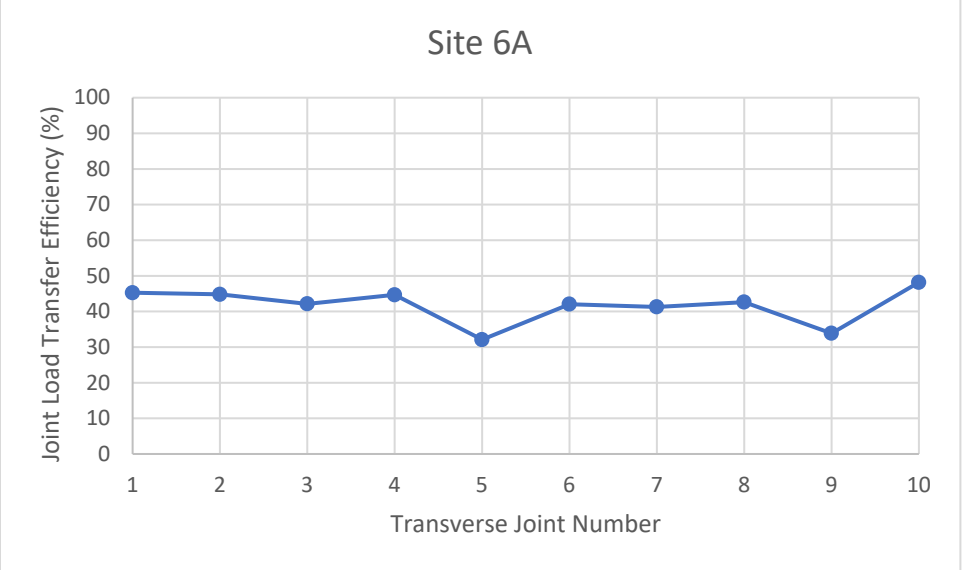

Figure 105. Joint-by-joint LTE results for Site 6A

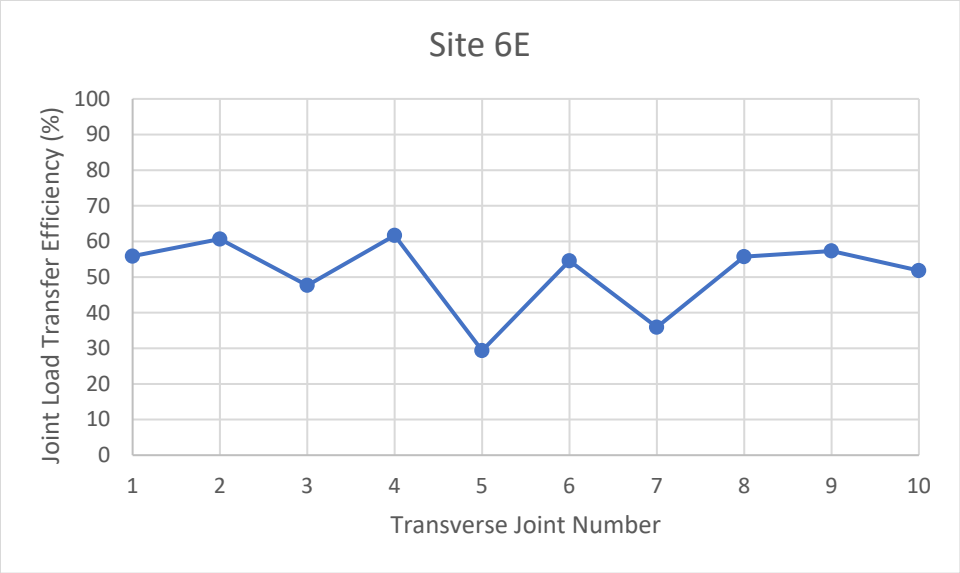

Figure 106. Joint-by-joint LTE results for Site 6E

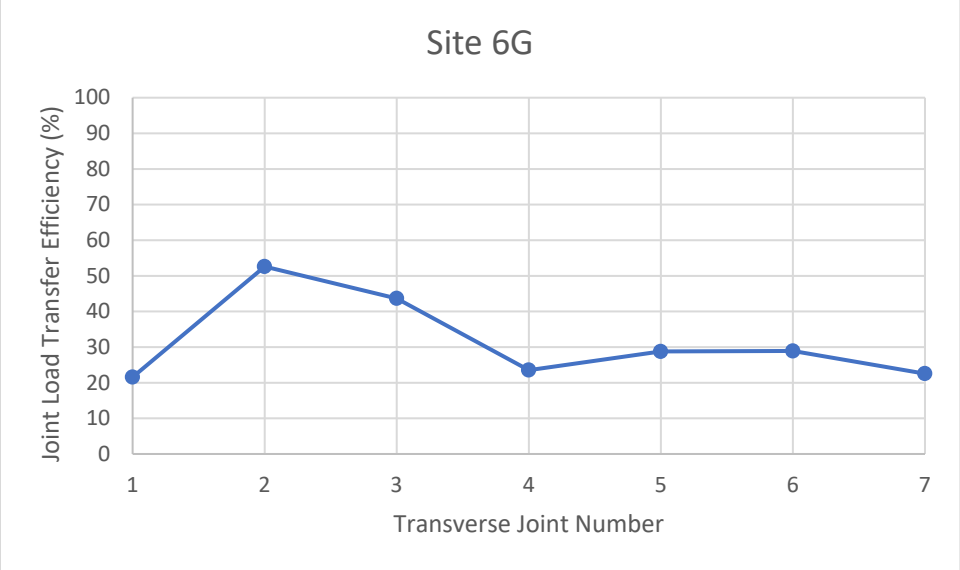

Figure 107. Joint-by-joint LTE results for Site 6G

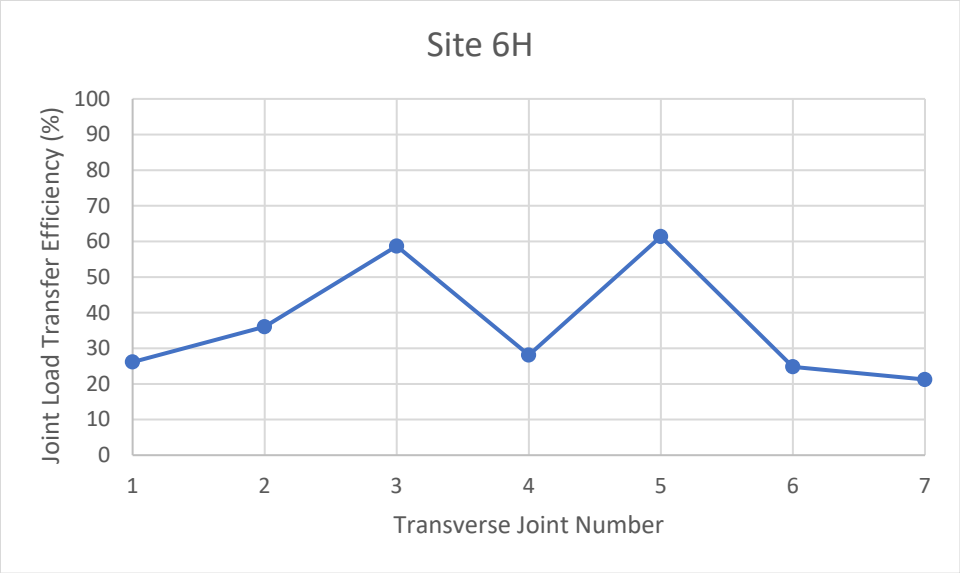

Figure 108. Joint-by-joint LTE results for Site 6H

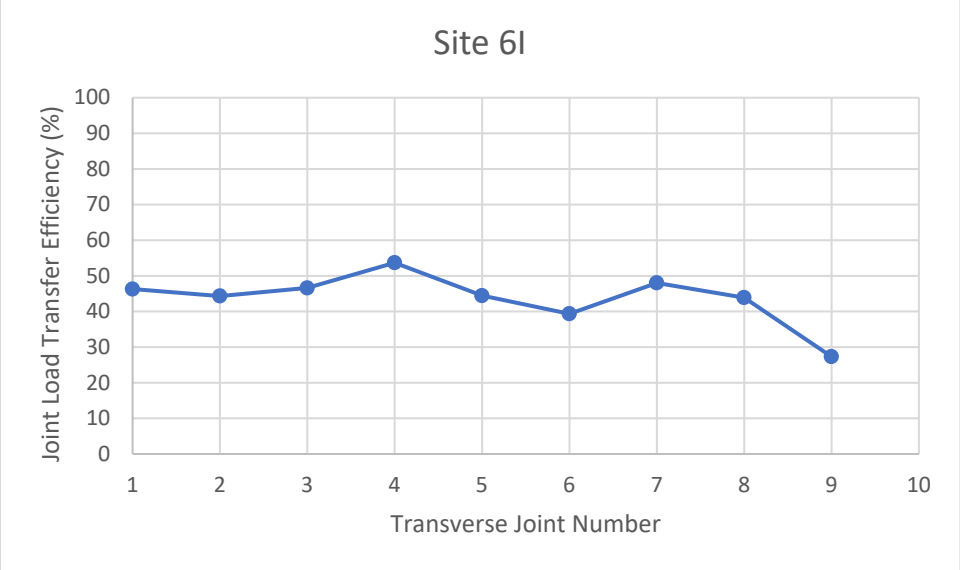

Figure 109. Joint-by-joint LTE results for Site 6I

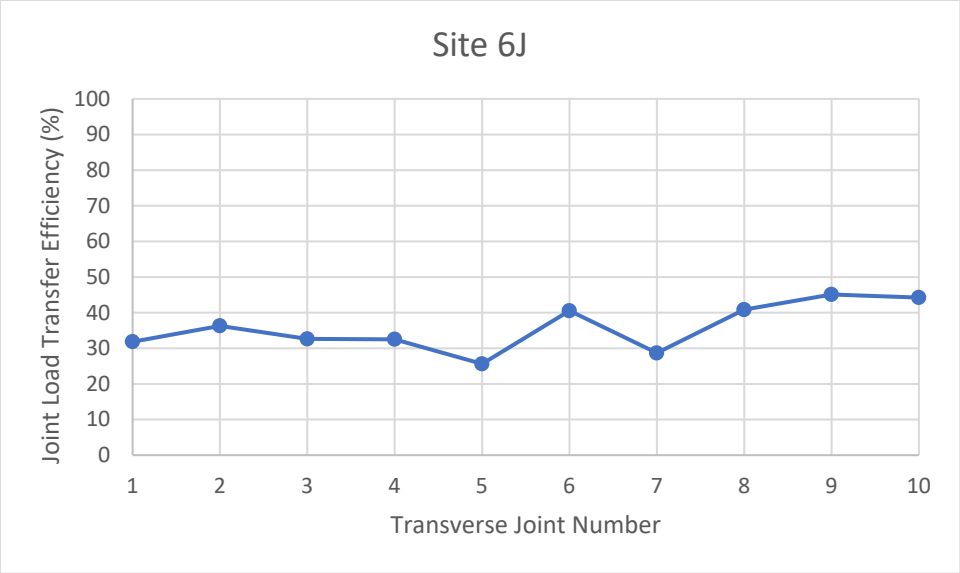

Figure 110. Joint-by-joint LTE results for Site 6J

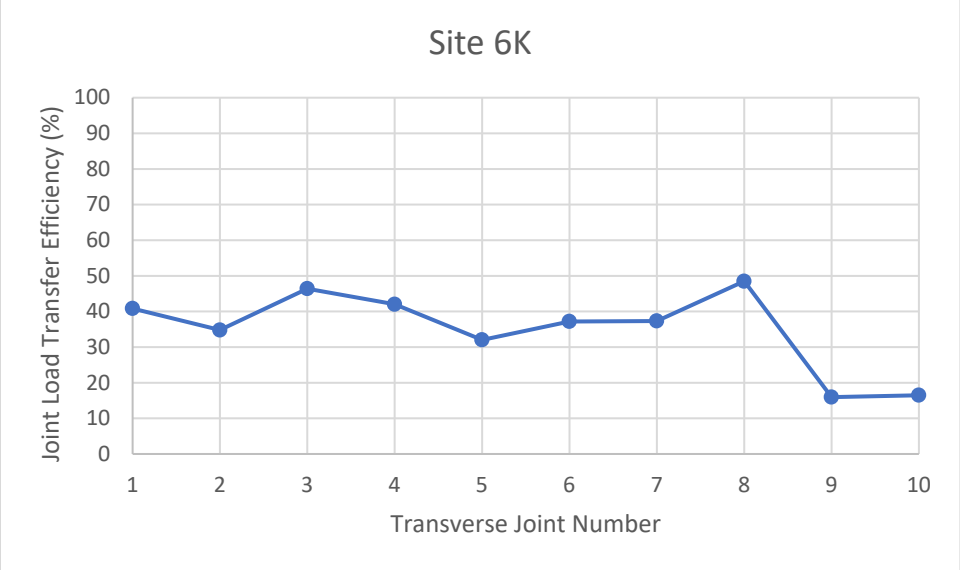

Figure 111. Joint-by-joint LTE results for Site 6K

APPENDIX C. ADDITIONAL HIGH-SPEED PROFILER RESULTS

Tables 77 through 110 contain summaries of the high-speed profiler results characterizing pavement smoothness and curling and warping for each individual test section at Site 4, Site 6, and Site 7.

Table 76. Summary of high-speed profiler results for Site 4A

Site 4A: COA-B, 4 in., 6 ft x 6 ft, No Fibers				
	IRI (in./mi)	Curvature IRI (in./mi)	Deflection (in.)	Deflection Ratio (in./ft)
Spring AM	87.6	81.9	0.0262	0.00436
Spring PM	93.0	85.8	0.0293	0.00489
Summer AM	99.0	93.2	0.0279	0.00464
Summer PM	97.5	91.4	0.0284	0.00473
Fall AM	86.0	81.5	0.0245	0.00409
Fall PM	88.6	83.2	0.0248	0.00413
Average	92.0	86.2	0.0268	0.00447

Table 77. Summary of high-speed profiler results for Site 4B

Site 4B: COA-B, 4 in., 12 ft x 12 ft, No Fibers				
	IRI (in./mi)	Curvature IRI (in./mi)	Deflection (in.)	Deflection Ratio (in./ft)
Spring AM	65.8	55.1	0.0328	0.00273
Spring PM	69.8	58.3	0.0393	0.00328
Summer AM	69.1	60.1	0.0422	0.00352
Summer PM	69.9	60.8	0.0426	0.00355
Fall AM	64.0	55.4	0.0365	0.00304
Fall PM	64.7	56.4	0.0369	0.00307
Average	67.2	57.7	0.0384	0.00320

Table 78. Summary of high-speed profiler results for Site 4C

Site 4C: COA-B, 4 in., 15 ft x 12 ft, No Fibers				
	IRI (in./mi)	Curvature IRI (in./mi)	Deflection (in.)	Deflection Ratio (in./ft)
Spring AM	67.9	51.7	0.0508	0.00339
Spring PM	71.1	56.5	0.0553	0.00368
Summer AM	71.2	58.8	0.0608	0.00406
Summer PM	68.5	56.4	0.0580	0.00387
Fall AM	71.7	57.7	0.0579	0.00386
Fall PM	70.4	55.4	0.0561	0.00374
Average	70.2	56.1	0.0565	0.00377

Table 79. Summary of high-speed profiler results for Site 4D

Site 4D: COA-B, 4 in., 20 ft x 12 ft, No Fibers				
	IRI (in./mi)	Curvature IRI (in./mi)	Deflection (in.)	Deflection Ratio (in./ft)
Spring AM	64.6	50.8	0.0598	0.00299
Spring PM	61.3	49.3	0.0597	0.00299
Summer AM	64.0	47.8	0.0615	0.00307
Summer PM	64.3	47.9	0.0608	0.00304
Fall AM	64.8	50.1	0.0622	0.00311
Fall PM	65.3	49.4	0.0617	0.00308
Average	64.0	49.2	0.0609	0.00305

Table 80. Summary of high-speed profiler results for Site 4E

Site 4E: COA-B, 4 in., 20 ft x 12 ft, Fibers				
	IRI (in./mi)	Curvature IRI (in./mi)	Deflection (in.)	Deflection Ratio (in./ft)
Spring AM	64.1	46.8	0.0532	0.00266
Spring PM	69.0	51.3	0.0694	0.00347
Summer AM	77.3	60.4	0.0880	0.00440
Summer PM	76.6	55.7	0.0803	0.00402
Fall AM	71.1	49.3	0.0614	0.00307
Fall PM	69.8	50.0	0.0596	0.00298
Average	71.3	52.2	0.0687	0.00343

Table 81. Summary of high-speed profiler results for Site 4F

Site 4F: COA-B, 4 in., 15 ft x 12 ft, Fibers				
	IRI (in./mi)	Curvature IRI (in./mi)	Deflection (in.)	Deflection Ratio (in./ft)
Spring AM	58.0	45.5	0.0406	0.00270
Spring PM	59.5	49.6	0.0420	0.00280
Summer AM	64.4	54.4	0.0489	0.00326
Summer PM	63.3	51.6	0.0482	0.00321
Fall AM	61.4	49.6	0.0447	0.00298
Fall PM	61.3	49.1	0.0429	0.00286
Average	61.3	50.0	0.0445	0.00297

Table 82. Summary of high-speed profiler results for Site 4G

Site 4G: COA-B, 4 in., 12 ft x 12 ft, No Fibers				
	IRI (in./mi)	Curvature IRI (in./mi)	Deflection (in.)	Deflection Ratio (in./ft)
Spring AM	59.6	52.0	0.0389	0.00324
Spring PM	63.2	53.3	0.0394	0.00329
Summer AM	59.2	53.4	0.0431	0.00359
Summer PM	57.7	51.1	0.0395	0.00329
Fall AM	60.0	54.6	0.0426	0.00355
Fall PM	60.9	55.7	0.0410	0.00342
Average	60.1	53.3	0.0408	0.00340

Table 83. Summary of high-speed profiler results for Site 4H

Site 4H: COA-B, 4 in., 6 ft x 6 ft, Fibers				
	IRI (in./mi)	Curvature IRI (in./mi)	Deflection (in.)	Deflection Ratio (in./ft)
Spring AM	61.1	57.2	0.0204	0.00340
Spring PM	63.7	60.8	0.0212	0.00353
Summer AM	64.9	60.6	0.0216	0.00361
Summer PM	66.2	61.9	0.0223	0.00371
Fall AM	59.5	56.3	0.0204	0.00340
Fall PM	58.6	54.8	0.0210	0.00349
Average	62.3	58.6	0.0211	0.00352

Table 84. Summary of high-speed profiler results for Site 4I

Site 4I: COA-B, 6 in., 6 ft x 6 ft, Fibers				
	IRI (in./mi)	Curvature IRI (in./mi)	Deflection (in.)	Deflection Ratio (in./ft)
Spring AM	81.8	76.4	0.0278	0.00463
Spring PM	80.6	76.3	0.0287	0.00479
Summer AM	83.1	79.1	0.0282	0.00470
Summer PM	82.7	78.0	0.0282	0.00470
Fall AM	84.9	81.5	0.0290	0.00483
Fall PM	84.4	79.5	0.0274	0.00456
Average	82.9	78.5	0.0282	0.00470

Table 85. Summary of high-speed profiler results for Site 4J

Site 4J: COA-B, 6 in., 12 ft x 12 ft, Fibers				
	IRI (in./mi)	Curvature IRI (in./mi)	Deflection (in.)	Deflection Ratio (in./ft)
Spring AM	57.5	45.6	0.0321	0.00236
Spring PM	60.5	48.7	0.0340	0.00283
Summer AM	56.8	46.0	0.0336	0.00280
Summer PM	58.3	47.0	0.0339	0.00283
Fall AM	54.7	43.8	0.0309	0.00258
Fall PM	55.2	44.7	0.0301	0.00251
Average	57.2	46.0	0.0325	0.00265

Table 86. Summary of high-speed profiler results for Site 4K

Site 4K: COA-B, 6 in., 15 ft x 12 ft, Fibers				
	IRI (in./mi)	Curvature IRI (in./mi)	Deflection (in.)	Deflection Ratio (in./ft)
Spring AM	55.5	40.7	0.0351	0.00234
Spring PM	57.9	41.5	0.0376	0.00250
Summer AM	54.8	40.2	0.0390	0.00260
Summer PM	55.4	40.2	0.0418	0.00279
Fall AM	57.5	42.8	0.0407	0.00272
Fall PM	56.5	41.7	0.0380	0.00253
Average	56.3	41.2	0.0387	0.00258

Table 87. Summary of high-speed profiler results for Site 4L

Site 4L: COA-B, 6 in., 20 ft x 12 ft, Fibers				
	IRI (in./mi)	Curvature IRI (in./mi)	Deflection (in.)	Deflection Ratio (in./ft)
Spring AM	77.0	60.5	0.0653	0.00326
Spring PM	70.5	54.7	0.0651	0.00325
Summer AM	69.3	51.9	0.0635	0.00318
Summer PM	69.3	54.3	0.0666	0.00333
Fall AM	76.5	60.4	0.0724	0.00362
Fall PM	76.6	61.8	0.0675	0.00338
Average	73.2	57.3	0.0667	0.00334

Table 88. Summary of high-speed profiler results for Site 4M

Site 4M: COA-B, 6 in., 20 ft x 12 ft, No Fibers				
	IRI (in./mi)	Curvature IRI (in./mi)	Deflection (in.)	Deflection Ratio (in./ft)
Spring AM	60.8	46.2	0.0489	0.00245
Spring PM	62.8	41.5	0.0484	0.00242
Summer AM	59.7	42.4	0.0511	0.00256
Summer PM	62.0	43.1	0.0525	0.00263
Fall AM	59.0	41.8	0.0474	0.00237
Fall PM	58.2	42.5	0.0468	0.00234
Average	60.4	42.9	0.0492	0.00246

Table 89. Summary of high-speed profiler results for Site 4N

Site 4N: COA-B, 6 in., 15 ft x 12 ft, No Fibers				
	IRI (in./mi)	Curvature IRI (in./mi)	Deflection (in.)	Deflection Ratio (in./ft)
Spring AM	57.2	46.4	0.0386	0.00258
Spring PM	64.2	49.2	0.0449	0.00300
Summer AM	62.7	50.4	0.0460	0.00307
Summer PM	64.7	50.9	0.0473	0.00316
Fall AM	55.8	44.6	0.0372	0.00248
Fall PM	55.7	46.2	0.0398	0.00265
Average	60.0	48.0	0.0423	0.00282

Table 90. Summary of high-speed profiler results for Site 4O

Site 4O: COA-B, 6 in., 12 ft x 12 ft, No Fibers				
	IRI (in./mi)	Curvature IRI (in./mi)	Deflection (in.)	Deflection Ratio (in./ft)
Spring AM	68.7	55.2	0.0366	0.00305
Spring PM	74.3	60.7	0.0427	0.00356
Summer AM	76.8	65.4	0.0465	0.00387
Summer PM	71.6	58.1	0.0431	0.00359
Fall AM	65.6	53.9	0.0366	0.00305
Fall PM	65.5	54.0	0.0360	0.00300
Average	70.4	57.9	0.0402	0.00335

Table 91. Summary of high-speed profiler results for Site 4P

Site 4P: COA-B, 6 in., 6 ft x 6 ft, No Fibers				
	IRI (in./mi)	Curvature IRI (in./mi)	Deflection (in.)	Deflection Ratio (in./ft)
Spring AM	70.7	64.3	0.0236	0.00394
Spring PM	72.1	66.5	0.0262	0.00436
Summer AM	70.2	63.5	0.0229	0.00382
Summer PM	70.9	63.6	0.0241	0.00402
Fall AM	63.5	58.8	0.0212	0.00354
Fall PM	65.2	58.8	0.0212	0.00353
Average	68.8	62.6	0.0232	0.00387

Table 92. Summary of high-speed profiler results for Site 6A

Site 6A: COC-U, 6 in., 11 ft x 11 ft, No Fibers				
	IRI (in./mi)	Curvature IRI (in./mi)	Deflection (in.)	Deflection Ratio (in./ft)
Spring AM	36.5	30.3	0.0204	0.00170
Spring PM	37.0	32.4	0.0215	0.00179
Summer AM	41.6	33.8	0.0205	0.00171
Summer PM	45.7	41.9	0.0279	0.00233
Fall AM	43.2	34.7	0.0225	0.00188
Fall PM	40.5	31.9	0.0178	0.00148
Average	40.8	34.2	0.0218	0.00181

Table 93. Summary of high-speed profiler results for Site 6B

Site 6B: COC-U, 6 in., 5.5 ft x 5.5 ft, Fibers				
	IRI (in./mi)	Curvature IRI (in./mi)	Deflection (in.)	Deflection Ratio (in./ft)
Spring AM	52.6	51.1	0.0173	0.00289
Spring PM	53.0	51.3	0.0186	0.00311
Summer AM	55.4	54.7	0.0170	0.00284
Summer PM	59.6	57.6	0.0220	0.00367
Fall AM	51.1	50.1	0.0151	0.00252
Fall PM	51.9	51.1	0.0161	0.00268
Average	53.9	52.6	0.0177	0.00295

Table 94. Summary of high-speed profiler results for Site 6C

Site 6C: COC-U, 6 in., 11 ft x 11 ft, Fibers				
	IRI (in./mi)	Curvature IRI (in./mi)	Deflection (in.)	Deflection Ratio (in./ft)
Spring AM	36.8	33.6	0.0187	0.00156
Spring PM	36.2	34.3	0.0167	0.00139
Summer AM	42.8	34.8	0.0204	0.00170
Summer PM	39.7	35.7	0.0240	0.00200
Fall AM	41.5	35.2	0.0209	0.00174
Fall PM	41.3	35.5	0.0187	0.00156
Average	39.7	34.9	0.0199	0.00166

Table 95. Summary of high-speed profiler results for Site 6D

Site 6D: COC-U, 6 in., 15 ft x 11 ft, Fibers				
	IRI (in./mi)	Curvature IRI (in./mi)	Deflection (in.)	Deflection Ratio (in./ft)
Spring AM	54.4	53.5	0.0428	0.00285
Spring PM	53.3	51.7	0.0347	0.00232
Summer AM	55.7	47.5	0.0313	0.00209
Summer PM	55.5	47.6	0.0469	0.00313
Fall AM	55.7	48.1	0.0321	0.00214
Fall PM	55.7	46.2	0.0318	0.00212
Average	55.1	49.1	0.0366	0.00244

Table 96. Summary of high-speed profiler results for Site 6E

Site 6E: COC-U, 6 in., 20 ft x 11 ft, Fibers				
	IRI (in./mi)	Curvature IRI (in./mi)	Deflection (in.)	Deflection Ratio (in./ft)
Spring AM	59.2	53.4	0.0687	0.00344
Spring PM	61.0	55.9	0.0603	0.00301
Summer AM	74.5	47.5	0.0464	0.00232
Summer PM	79.0	60.8	0.0780	0.00390
Fall AM	68.9	45.6	0.0406	0.00203
Fall PM	71.3	47.8	0.0516	0.00258
Average	69.0	51.8	0.0576	0.00288

Table 97. Summary of high-speed profiler results for Site 6F

Site 6F: COC-U, 6 in., 30 ft x 11 ft, Fibers				
	IRI (in./mi)	Curvature IRI (in./mi)	Deflection (in.)	Deflection Ratio (in./ft)
Spring AM	91.2	78.7	0.1010	0.00337
Spring PM	90.0	73.6	0.1046	0.00349
Summer AM	104.6	64.8	0.1133	0.00378
Summer PM	109.1	75.4	0.1651	0.00550
Fall AM	100.2	64.6	0.1160	0.00387
Fall PM	101.4	63.3	0.1089	0.00363
Average	99.4	70.1	0.1181	0.00394

Table 98. Summary of high-speed profiler results for Site 6G

Site 6G: COC-U, 6 in., 40 ft x 11 ft, Fibers				
	IRI (in./mi)	Curvature IRI (in./mi)	Deflection (in.)	Deflection Ratio (in./ft)
Spring AM	70.5	34.2	0.1164	0.00291
Spring PM	71.6	38.3	0.1311	0.00328
Summer AM	84.7	35.4	0.1147	0.00287
Summer PM	98.7	34.0	0.1191	0.00298
Fall AM	88.6	35.4	0.1296	0.00324
Fall PM	87.4	35.5	0.1253	0.00313
Average	83.6	35.5	0.1227	0.00307

Table 99. Summary of high-speed profiler results for Site 6H

Site 6H: COC-U, 6 in., 40 ft x 11 ft, No Fibers				
	IRI (in./mi)	Curvature IRI (in./mi)	Deflection (in.)	Deflection Ratio (in./ft)
Spring AM	46.4	23.1	0.0489	0.00122
Spring PM	43.4	24.5	0.0581	0.00145
Summer AM	47.1	20.7	0.0450	0.00075
Summer PM	48.3	21.0	0.0790	0.00198
Fall AM	43.0	17.8	0.0552	0.00138
Fall PM	44.9	19.3	0.0578	0.00144
Average	45.5	21.1	0.0573	0.00137

Table 100. Summary of high-speed profiler results for Site 6I

Site 6I: COC-U, 6 in., 30 ft x 11 ft, No Fibers				
	IRI (in./mi)	Curvature IRI (in./mi)	Deflection (in.)	Deflection Ratio (in./ft)
Spring AM	34.5	29.0	0.0526	0.00175
Spring PM	36.2	28.0	0.0543	0.00181
Summer AM	45.9	23.4	0.0602	0.00201
Summer PM	46.4	23.0	0.0655	0.00218
Fall AM	47.4	25.7	0.0602	0.00201
Fall PM	45.6	24.4	0.0526	0.00175
Average	42.7	25.6	0.0576	0.00192

Table 101. Summary of high-speed profiler results for Site 6J

Site 6J: COC-U, 6 in., 20 ft x 11 ft, No Fibers				
	IRI (in./mi)	Curvature IRI (in./mi)	Deflection (in.)	Deflection Ratio (in./ft)
Spring AM	40.0	36.2	0.0471	0.00235
Spring PM	41.3	32.6	0.0405	0.00203
Summer AM	48.8	25.4	0.0365	0.00182
Summer PM	55.5	37.6	0.0498	0.00249
Fall AM	47.8	29.8	0.0441	0.00220
Fall PM	46.3	28.5	0.0383	0.00192
Average	46.6	31.7	0.0427	0.00214

Table 102. Summary of high-speed profiler results for Site 6K

Site 6K: COC-U, 6 in., 15 ft x 11 ft, No Fibers				
	IRI (in./mi)	Curvature IRI (in./mi)	Deflection (in.)	Deflection Ratio (in./ft)
Spring AM	50.5	49.4	0.0460	0.00306
Spring PM	51.8	51.3	0.0472	0.00315
Summer AM	62.2	47.3	0.0415	0.00277
Summer PM	67.9	58.4	0.0587	0.00391
Fall AM	60.4	50.4	0.0478	0.00319
Fall PM	58.4	46.7	0.0456	0.00304
Average	58.5	50.6	0.0478	0.00319

Table 103. Summary of high-speed profiler results for Site 6L

Site 6L: COC-U, 6 in., 5.5 ft x 5.5 ft, No Fibers				
	IRI (in./mi)	Curvature IRI (in./mi)	Deflection (in.)	Deflection Ratio (in./ft)
Spring AM	53.1	52.5	0.0196	0.00327
Spring PM	57.1	54.8	0.0211	0.00351
Summer AM	63.5	61.3	0.0233	0.00389
Summer PM	69.2	67.3	0.0283	0.00472
Fall AM	61.5	59.4	0.0212	0.00353
Fall PM	65.1	63.2	0.0222	0.00370
Average	61.6	59.8	0.0226	0.00377

Table 104. Summary of high-speed profiler results for Site 7A

Site 7A: COA-U, 6 in., 6 ft x 6 ft, No Fibers				
	IRI (in./mi)	Curvature IRI (in./mi)	Deflection (in.)	Deflection Ratio (in./ft)
Spring AM	60.6	55.9	0.0217	0.00361
Spring PM	69.9	65.0	0.0259	0.00432
Summer AM	63.3	59.1	0.0226	0.00376
Summer PM	62.0	57.0	0.0220	0.00367
Fall AM	65.2	61.1	0.0232	0.00387
Fall PM	65.9	60.8	0.0226	0.00377
Average	64.5	59.8	0.0230	0.00383

Table 105. Summary of high-speed profiler results for Site 7B

Site 7B: COA-U, 6 in., 15 ft x 12 ft, Fibers				
	IRI (in./mi)	Curvature IRI (in./mi)	Deflection (in.)	Deflection Ratio (in./ft)
Spring AM	57.7	41.0	0.0386	0.00257
Spring PM	66.1	51.3	0.0494	0.00329
Summer AM	61.7	45.3	0.0413	0.00275
Summer PM	58.9	44.0	0.0381	0.00254
Fall AM	67.7	52.3	0.0483	0.00322
Fall PM	62.1	46.0	0.0386	0.00257
Average	62.4	46.6	0.0424	0.00283

Table 106. Summary of high-speed profiler results for Site 7C

Site 7C: COA-U, 6 in., 12 ft x 12 ft, Fibers				
	IRI (in./mi)	Curvature IRI (in./mi)	Deflection (in.)	Deflection Ratio (in./ft)
Spring AM	46.5	32.1	0.0254	0.00212
Spring PM	55.8	38.9	0.0320	0.00267
Summer AM	46.8	34.2	0.0263	0.00219
Summer PM	47.4	33.5	0.0261	0.00218
Fall AM	49.9	38.0	0.0291	0.00242
Fall PM	48.1	35.1	0.0270	0.00225
Average	49.1	35.3	0.0277	0.00230

Table 107. Summary of high-speed profiler results for Site 7D

Site 7D: COA-U, 6 in., 9 ft x 12 ft, Fibers				
	IRI (in./mi)	Curvature IRI (in./mi)	Deflection (in.)	Deflection Ratio (in./ft)
Spring AM	56.6	47.8	0.0275	0.00305
Spring PM	62.8	54.4	0.0315	0.00350
Summer AM	57.3	48.4	0.0277	0.00307
Summer PM	57.8	48.2	0.0280	0.00312
Fall AM	60.7	53.4	0.0288	0.00320
Fall PM	60.7	51.0	0.0282	0.00313
Average	59.3	50.5	0.0286	0.00318

Table 108. Summary of high-speed profiler results for Site 7E

Site 7E: COA-U, 6 in., 9 ft x 6 ft, Fibers				
	IRI (in./mi)	Curvature IRI (in./mi)	Deflection (in.)	Deflection Ratio (in./ft)
Spring AM	51.7	43.6	0.0248	0.00276
Spring PM	60.9	51.4	0.0303	0.00337
Summer AM	53.6	45.4	0.0254	0.00283
Summer PM	52.8	44.4	0.0253	0.00281
Fall AM	55.6	48.8	0.0279	0.00310
Fall PM	53.6	44.6	0.0235	0.00261
Average	54.7	46.4	0.0262	0.00291

Table 109. Summary of high-speed profiler results for Site 7F

Site 7F: COA-U, 6 in., 6 ft x 6 ft, Fibers				
	IRI (in./mi)	Curvature IRI (in./mi)	Deflection (in.)	Deflection Ratio (in./ft)
Spring AM	60.9	57.1	0.0211	0.00352
Spring PM	71.6	67.3	0.0258	0.00430
Summer AM	64.2	61.0	0.0211	0.00352
Summer PM	63.6	59.8	0.0214	0.00357
Fall AM	66.9	64.4	0.0225	0.00374
Fall PM	64.4	60.5	0.0207	0.00345
Average	65.3	61.7	0.0221	0.00368

APPENDIX D. BEHAVIOR OF FIBER-REINFORCED CONCRETE PAVEMENTS CONSTRUCTED WITHOUT TRANSVERSE JOINTS

D.1. Introduction

Over the past several decades, pavement designers in the United States have explored the use of fiber-reinforced concrete (FRC) to construct pavements, particularly thin concrete overlays (Roesler et al. 2019, Fick et al. 2021). Synthetic macrofibers have emerged as the most common type of fiber used in pavement applications, and they provide a number of benefits to concrete pavements. Thanks to their ability to resist microcracking and slow crack propagation, synthetic macrofibers provide pavements with residual strength that enhances long-term fatigue life (ACI 2018, Roesler et al. 2019). At typical dosage rates of 0.2% to 0.5% by volume, or about 2.5 to 7.5 lb/yd^3 (depending on the fiber), FRC provides concrete pavements with a residual strength that equates to approximately 20% to 30% of their design residual strength (Bordelon and Roesler 2012).

Besides improving fatigue life, another potential use case for synthetic macrofibers is to increase joint spacing and reduce the number of joints in the pavement. Fibers are very commonly used to extend joint spacing in concrete floor slabs, where they help prevent mid-slab cracking that may occur when the joint spacing design exceeds normal limits (ACI 2018). The ability of fibers to increase joint spacing in concrete overlays is of particular interest due to the fact that many thin concrete overlay designs require a shorter sawcut joint spacing, e.g., 6 ft x 6 ft.

While shorter joint spacing designs are intended to reduce stresses and mitigate the potential for mid-panel cracking in thin slabs, field studies have found that not all transverse joints activate in these types of overlay designs, i.e., cracks do not form beneath all of the sawcut contraction joints (Roesler and Wang 2009, Gross et al. 2019). Given that joints can be a source of durability-related distresses in concrete pavements (Weiss et al. 2016), if not all joints tend to activate in concrete overlays, it raises the question of whether the optimal joint spacing design might be greater than current guidance indicates. There is also concern that unactivated joints could lead to dominant joint behavior, which has been associated with poor joint load transfer (King and Roesler 2014).

Meanwhile, the construction of continuously reinforced concrete pavements (CRCP) with steel rebar and without transverse contraction joints has been a standard practice around the world for decades. Researchers have also been interested in the potential for macrofibers to serve as the primary reinforcement for a concrete pavement or overlay placed without contraction joints. Without high volumes of steel embedded in the pavement, a continuously fiber-reinforced pavement is likely to behave differently than a typical CRCP. That said, laboratory research has suggested that a continuously FRC pavement with synthetic macrofibers might be able to perform well in fatigue and hold cracks together tightly (Mulheron et al. 2015).

In recent years, two FRC pavement test sections have been built without transverse sawcut joints to study the field behavior of this type of design. One test section was a 6 in. concrete on asphalt–unbonded (COA–U) overlay, while the other section was a 7 in. full-depth concrete

roundabout. This investigation both evaluated the feasibility of the concept of an FRC pavement constructed without transverse contraction joints, as well as aspects of the behavior of these sections that could provide further insight into more conventional FRC pavement and FRC overlay designs.

D.2. Test Section Design, Construction, and Monitoring

D.2.1. Joint-Free FRC Overlay in Worth County, Iowa

As part of the FRC overlay project constructed on Highway 105 in Worth County, Iowa, in October 2019 (Site 2), a 636 ft section of the overlay was designed without transverse joints. (This test section was known as Site 3 during testing and analysis.) The pavement in this section was placed without sawing transverse joints, and it was allowed to crack on its own. Centerline and shoulder longitudinal joints were sawed and reinforced with tie bars as normal. This test section was placed with a higher macrofiber content, 7.5 lb/yd^3, about 0.5% by volume, than the rest of the project, where the dosage rate was 4 lb/yd^3, about 0.3% by volume. Table 111 lists full details for the project and test section.

Table 111. Worth County (Site 3) project details

Parameter	Value
Overlay Type	COA–U
Existing Pavement	3 in. HMA over 7 in. PCC
Separation Layer	Geotextile
Concrete Overlay Thickness	6 in.
Transverse Joint Spacing (Typical)	12 ft
Longitudinal Joint Spacing	12 ft
Shoulders	Integral tied shoulders 3 ft in width
Fiber Reinforcement (Typical)	4 lb/yd^3
Fiber Reinforcement (Test Section)	7.5 lb/yd^3

Because of the higher fiber content of the test section, there was some concern that the mix for the test section would not be as workable as the mix for the rest of the project. Therefore, the total cementitious content of the mix for the test section was raised from 570 lb/yd^3 to 640 lb/yd^3, while other mix parameters such as water-to-cement ratio and admixture dosage rates were left unchanged. The cementitious materials were Type I portland cement with 20% class C fly ash substitution.

The test section was paved using conventional slipform paving equipment with machine control in the same manner as the rest of the project. Mixing was performed at a central batch plant with no changes from the typical sections other than the additional 70 lb/yd^3 of cementitious material, and the concrete was delivered to the grade using dump trucks.

For approximately the last 50 ft of paving of the test section, the total cementitious content was reduced back to 570 lb/yd^3 to see if it would be possible to pave with the original mix at the higher fiber content. This last stretch of the test section was placed successfully without issue, although the contractor observed more voids in the slab as it was extruded from the profile pan and reported that it was more difficult to finish. Figure 112 includes pictures from construction of the test section.

Figure 112. Construction photos from joint-free FRC overlay test section

No transverse cracking appeared within the first 24 hours after construction. Over the course of the following three days, six transverse cracks formed in the test section, reaching across the entire pavement surface from shoulder to shoulder. The locations of these cracks are shown in Figure 113. (The previous composite pavement surface is shown in the satellite image.) One week later, a seventh transverse crack formed in the cracks labeled “Random 3” and “Random 4” in Figure 113. Photos of a typical crack two weeks after construction are contained in Figure 114.

Figure 113. Initial crack formation in joint-free overlay test section

Figure 114. View of typical transverse crack in joint-free FRC overlay two weeks post-construction

The section was monitored over the next three years with periodic visits to survey crack development and measure crack width at the surface. By February 2020, 6 new cracks formed to create 13 total transverse cracks in the test section, and by December 2020, 11 more cracks had formed for a total of 24 transverse cracks. Since that time, no new cracks have formed in the test section. Given a 636 ft test section length (and with transverse sawcut joints on each end), the average transverse crack spacing in the test section is 25.4 ft. A few short longitudinal cracks formed in the test section as branches off of transverse cracks, but they only ran for a few feet before turning in and terminating at the centerline longitudinal joint.

The progression of crack width over time is plotted in Figure 115. Cracks are grouped according to when they were first observed, with cracks #1 through #7 forming in the first two weeks after construction, cracks #8 through #13 first observed in February 2020, cracks #14 through #17 first observed in August 2020, and cracks #15 through #24 first observed in December 2020.

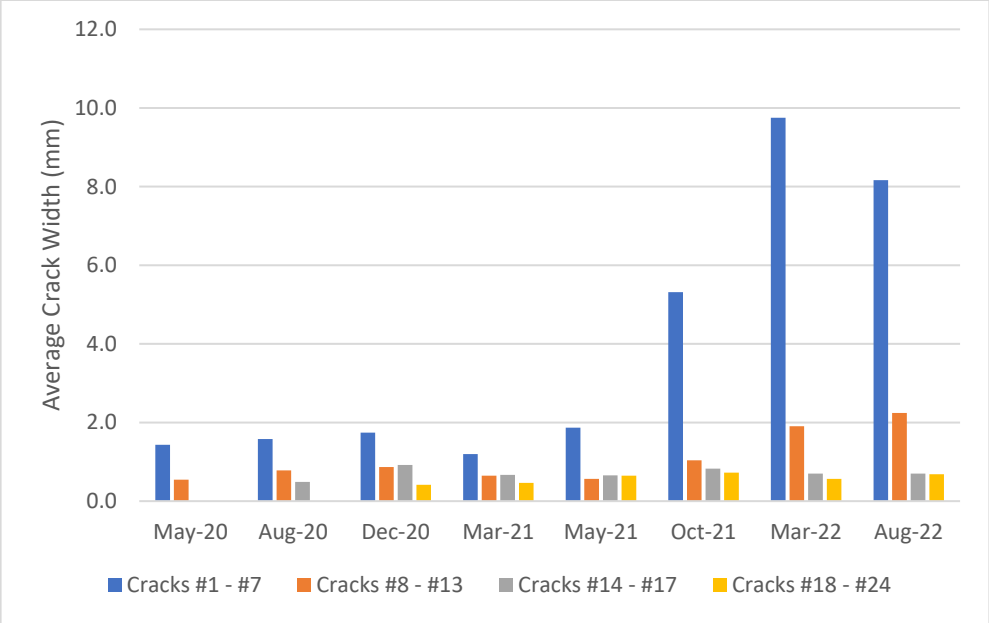

Figure 115. Crack width progression over time for the Worth County test section

As seen in Figure 115, there are two main trends related to crack width. First, cracks have grown wider over the three years since construction, subject to some shorter-term variation between visits. Second, cracks that formed earlier in the life of the test section have opened up to a greater extent than cracks that developed later. This trend is especially apparent when looking at cracks #1 through #7, which had an average width of 8.16 mm (0.32 in.) in August 2022, compared to an average width of 2.24 mm (0.088 in.) for cracks #8 through #17 and 0.69 mm (0.0027 in.) for the remaining cracks.

Falling weight deflectometer (FWD) testing was also performed after the October 2021 survey to measure the joint load transfer efficiency (LTE) across each transverse crack. In Figure 116, LTE measurements at each joint are plotted as a function of the crack width (as of October 2021). In Figure 117, the average joint LTE and average width are presented for each group of cracks. Cracks #1 through #7 had an average LTE of 27%, cracks #8 through #13 had an average LTE of 52%, and the remaining sets of cracks had an average LTE of 85%.

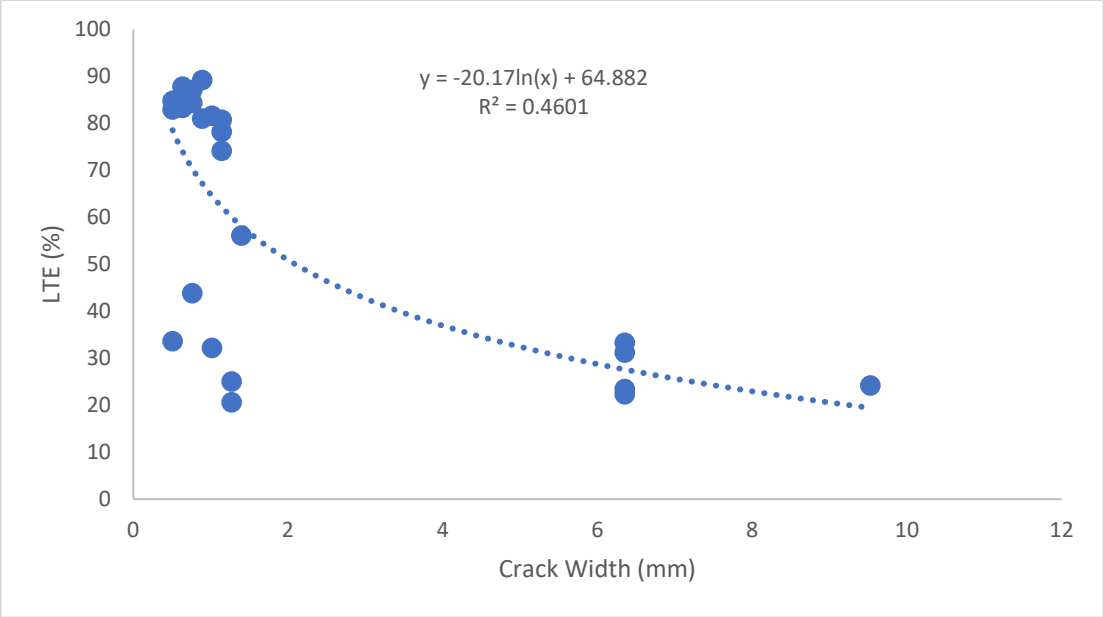

Figure 116. Crack width versus joint LTE for the Worth County test section, October 2022

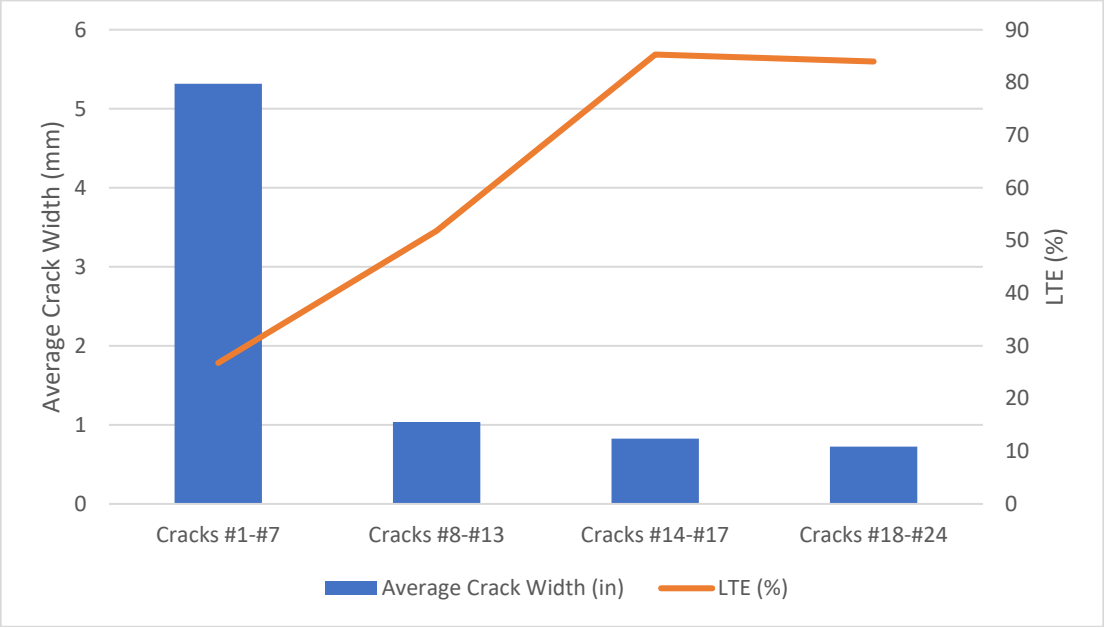

Figure 117. Average crack width and LTE for the Worth County test section, organized by group

As shown in Figures 116 and 117, LTE decreased with increasing crack width, and cracks that formed earlier had a lower average LTE than cracks that developed later. These findings make sense, as the aggregate interlock at a crack decreases as it widens. While the data in Figure 116 vary somewhat from the logarithmic trendline (R^2 = 0.46), this variation may result from the fact that crack width was measured at the surface and may not reflect the width of the crack through the depth of the overlay at the test location.

In spite of some of the wide cracks with low LTE values, as of August 2022 the joint-free FRC test section was performing well. The overall ride quality was good, no faulting had developed across any of the wider cracks (#1 through #13), and none of the other cracks (#14 through #24) had yet opened up to a width greater than 1 mm (0.04 in.) during any visit. As a precaution, cracks #1 through #13 were filled with a hot pour filler material to protect against spalling. The condition of the test section as of March 2022 is pictured in Figure 118.

Figure 118. Condition of the Worth County FRC test section, March 2022

D.2.2. Joint-Free FRC Roundabout in Sleepy Eye, Minnesota

In September 2018, an FRC roundabout was constructed in Sleepy Eye, Minnesota without sawcut transverse joints in the travel lane inside the ring. The primary motivation behind this project was to see if a fiber-reinforced roundabout without joints might be a viable alternative to jointed plain concrete roundabouts, which can have complicated joint patterns depending on the geometric design. The synthetic macrofibers were dosed at 6.0 lb/yd^3, about 0.4% by volume.

Although this roundabout was not a concrete overlay, the fiber reinforcement rate was similar to that of many FRC overlay projects, including the joint-free FRC overlay in Worth County, and the behavior of this project could provide useful insight into the behavior of both conventional FRC pavements and FRC overlays. One difference between the roundabout and overlay test section was that sawcut notches 4 ft apart were placed at the edge of the outer ring of the roundabout to see if they would direct crack formation. Project details are included in Table 112.

Table 112. Minnesota FRC roundabout project details

Parameter	Value
Concrete Thickness	7 in.
Pavement Width	16 ft
Subbase Layer/Thickness	6 in. granular subbase
Sawcut Notch Spacing	4 ft
Sawcut Notch Length	1.5 ft
Sawcut Notch Depth	1.5 in.
Fiber Reinforcement	6.0 lb/yd^3

No issues were reported with mixing or placement of the concrete, and the roundabout was paved using a roller screed. Like the Worth County FRC overlay, cracks began to form a few days after construction, with eight transverse cracks developing inside the ring within a week. The FRC roundabout was visited once each year after construction for three years to monitor crack development and perform testing. Through September 2021, 36 cracks developed within the ring, which is pictured in Figure 119(a). The cracks were mostly transverse across the pavement within the ring, but a few longitudinal cracks were also observed. The crack pattern is shown in Figure 119(b).

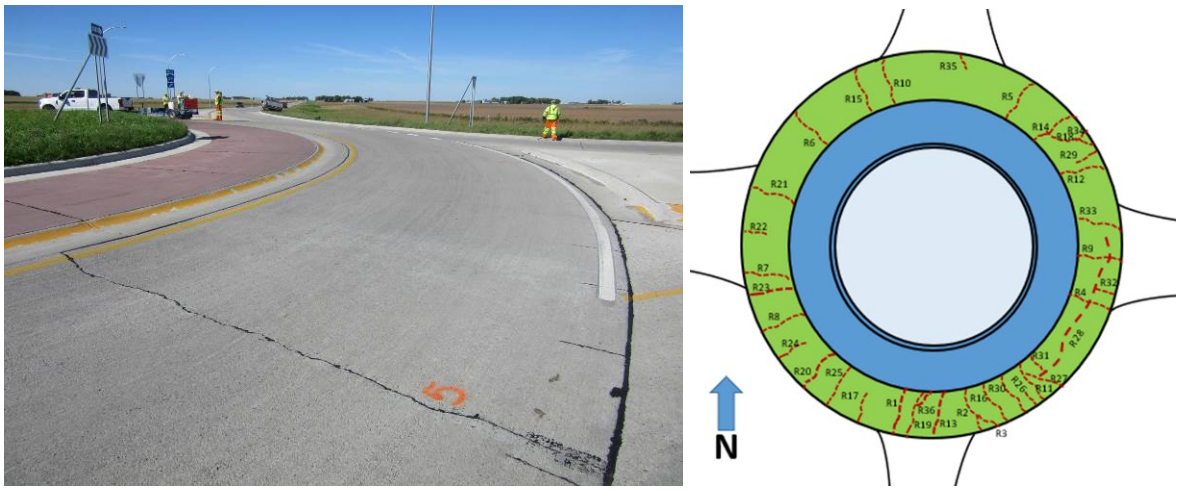

(a) (b)

Figure 119. The (a) condition and (b) observed crack pattern in the FRC roundabout

About 20 of the 36 total cracks initiated from the notch locations at the outer edge of the ring, while another 5 of the cracks were within about 6 in. of the notches. Given a middle radius of the ring of 492 ft, the approximate transverse crack spacing was approximately 13.8 ft, though spacing between cracks varied considerably between different areas of the ring.

As seen in Figure 119(b), a much greater number of cracks formed in the southern/eastern quadrants of the ring compared to the northern/western quadrants. One potential explanation for this disparity was that the roundabout was paved on a windy day with winds out of the southeast,

which could have driven differences in drying shrinkage between different areas of the roundabout.

The progression of crack opening behavior over time is shown in Figure 120. The cracks were divided into groups based on order of appearance. Cracks R1 through R8 appeared during the first week after construction, cracks R9 through R18 developed over the course of the rest of the first year through the fall of 2019, cracks R19 through R29 developed over the next year through the fall of 2020, and cracks R30 through R36 developed by September 2021.

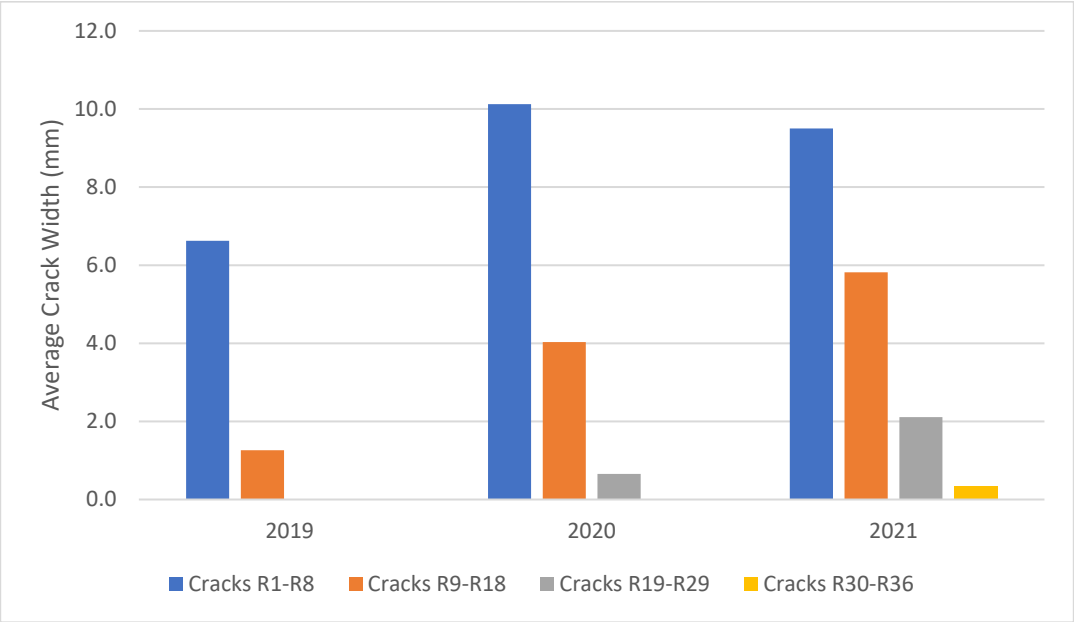

Figure 120. Crack width progression over time in the FRC roundabout

Like in Worth County, cracks tended to become wider in the time after they first appeared, and cracks that formed earlier opened up to a greater width than cracks that formed later. Through 2021, cracks R1 through R8 opened to an average width of 9.5 mm (0.37 in.), compared to 5.8 mm (0.23 in.) for cracks R9 through R18, 2.1 mm (0.083 in.) for R19 through R29, and 0.36 mm (0.014 in.) for R30 through R36. The wider cracks were filled with a hot-poured crumb rubber filler material.

FWD testing and faulting measurements were performed across a select number of the transverse cracks to characterize their performance. Results for crack width versus LTE are plotted in Figure 121, including measurements taken on both sides of the cracks. The observed trend was very similar to that of the FRC overlay test section in Worth County, with a clear decline in LTE with increasing crack width.

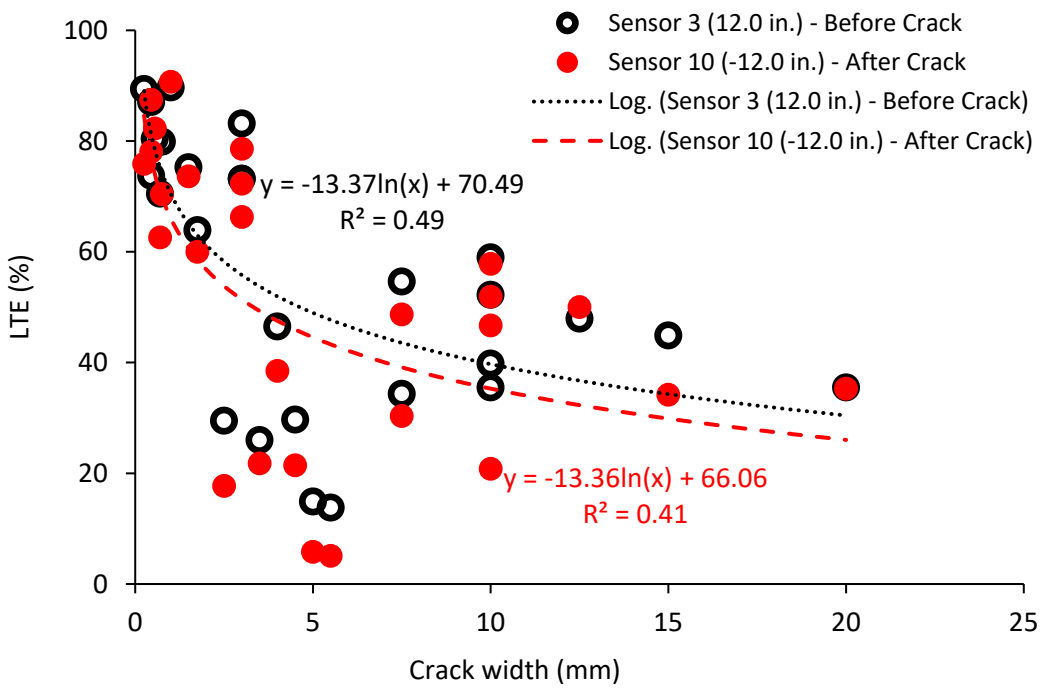

Figure 121. Crack width versus LTE for the FRC roundabout, September 2021

Unlike in Worth County, measurable faulting across the transverse cracks in the roundabout was detected using a digital faultmeter, with results plotted in Figure 122. Faulting as great as 12 mm (0.47 in.) was observed across the right wheel path (RWP) of crack R11, and a number of other cracks had faulting greater than 6 mm (0.24 in.) across both the RWP and left wheel path (LWP).

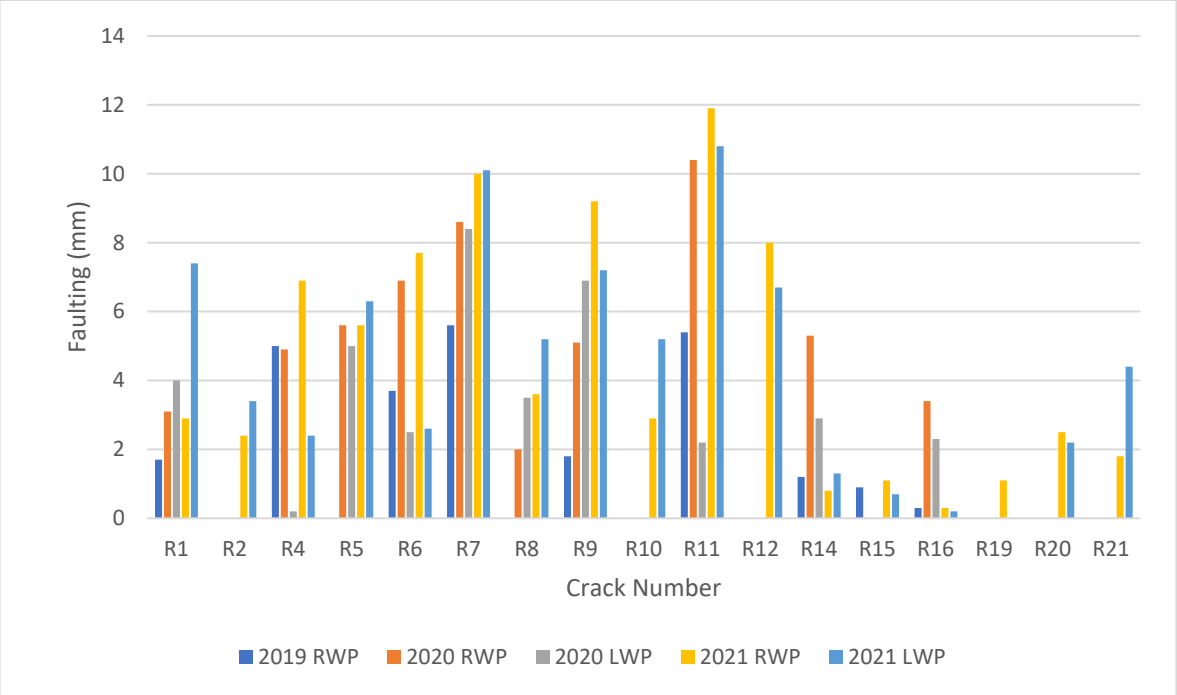

Figure 122. Faulting test results for the FRC roundabout

In spite of the faulting, through September 2021 the roundabout was generally in good condition. While a number of the cracks had opened up to a considerable degree with loss of load transfer and faulting, ride quality was reasonable, helped by the fact that vehicles must slow down to navigate the roundabout. There were no other signs of early distress or deterioration.

D.3. Analysis of Crack Opening and Test Section Behavior

Overall, both the joint-free FRC overlay section and the joint-free FRC roundabout have performed well through their first few years of service. Many of the later-forming cracks on these projects have remained tight and maintained good load transfer. However, most of the cracks that developed within about a year of construction at both sections have opened to a significantly greater degree, resembling the behavior of dominant joints in a jointed concrete pavement. These cracks have demonstrated faulting and a loss of load transfer, and they have been filled to protect them from spalling.

Adding to these performance concerns, the degree to which the dominant cracks have opened to appears to be greater than would be predicted from drying shrinkage and temperature-related volume change. Darter (1977) first proposed an empirical equation for predicting the mean joint opening in a jointed plain concrete pavement over a yearly time interval based on shrinkage, temperature, and slab-subbase friction. Kim et al. (2017) later updated that equation to account for the residual strength of FRC.

The equation to predict crack opening within an FRC pavement is shown in equation 7, where ΔL is the predicted crack opening, C is an adjustment factor for slab-subbase friction (typically

0.65 to 0.80), L is the design joint spacing, α_t is the coefficient of thermal expansion of concrete, ΔT is the difference between the temperature at concrete placement and the lowest mean minimum monthly temperature, ε is the drying shrinkage coefficient (typically 0.50×10^{-4} to 2.50×10^{-4} mm/mm), and $f_{residual}/f_{MOR}$ is the ratio of the residual flexural strength to the design flexural strength of FRC.

$$\Delta L = CL(\alpha_t \Delta T + \varepsilon)(1 - f_{residual}/f_{MOR}) \quad (7)$$

Equation (7) was used to predict the crack opening for both joint-free FRC test sections. Two cases were considered to calculate the predicted crack openings. First, the average spacing of the transverse cracks at each project was used as the input value for joint spacing, L, and the predicted crack width was compared to the average width of all transverse cracks. In the second case, only the larger working cracks were considered in the equation, which were cracks #1 through #13 in the overlay and cracks R1 through R18 in the roundabout. In this case, the average spacing of just these dominant cracks was used for the input value of L, and the predicted crack widths were compared just to the average widths of the dominant cracks. Finally, for both cases, the predicted crack widths were calculated both accounting for the residual strength benefits of fiber reinforcement as well as assuming no benefit from fiber reinforcement, i.e., $f_{residual} = 0$.

Table 113 contains the results for predicted crack width and comparison to actual field-measured values for both the joint-free FRC overlay and roundabout. In all cases, the actual average crack openings measured in the field were greater than predicted, even when assuming no benefits from the residual strength of the fibers. The discrepancy between predicted and actual crack openings was greater in the roundabout than in the overlay test section.

Table 113. Predicted and actual measured crack widths in the joint-free FRC test sections

All Cracks	Predicted Average Crack Opening (mm)		Actual Average Crack Opening (mm)
	Fibers	No Fibers	
Worth County Overlay	1.64	2.35	3.25
FRC Roundabout	1.28	1.71	4.45
Larger Working Cracks Only	**Predicted Average Crack Opening (mm)**		**Actual Average Crack Opening (mm)**
	Fibers	**No Fibers**	
Worth County Overlay	2.94	4.19	4.90
FRC Roundabout	2.48	3.31	7.47

Since the predicted values are based only on drying shrinkage and temperature changes, there are additional factors such as traffic impacts, spalling, or intrusion of incompressible materials that may contribute to the width of the cracks in the field. That said, the fact that the average widths

were so much higher than predicted suggests that the long-term performance of this system will not compare favorably to a typical jointed pavement with an equivalent joint spacing design. Additionally, since the crack widths were greater than predicted even when assuming no benefit from the fibers, the findings suggest that the fibers may not be effective across the dominant cracks.

In the end, these joint-free FRC test sections do not appear to be a successful application of fiber reinforcement for concrete overlays. This type of design could be revisited using a higher dosage rate of synthetic macrofibers or with another type of fiber, such as steel.

One area where these findings may provide insight for conventional jointed FRC overlays is the importance of uniform joint behavior. As mentioned previously, one concern associated with unactivated joints in concrete overlays is the potential for the development of dominant joint behavior. The performance of these joint-free sections demonstrates the poor performance outcomes of dominant joints when they occur.

D.4. Conclusions

There has been significant interest in recent years in using fibers to increase the joint spacing design of concrete pavements and concrete overlays and in potentially eliminating transverse joints altogether. This study investigated the performance of two FRC test sections that have been constructed in recent years to test the concept of designing an FRC pavement without transverse sawcut contraction joints. Two pavements were constructed, an FRC overlay test section on a roadway in Worth County, Iowa, and an FRC roundabout near Sleepy Eye, Minnesota.

Both test sections were paved successfully and are performing well to date. However, both pavements have experienced dominant crack behavior, as earlier-developing cracks opened to a greater extent than later-forming cracks. These dominant cracks have experienced a significant loss of load transfer, demonstrating the limitations of fiber reinforcement to be able to provide positive load transfer. Although these sections did not appear to be an entirely successful demonstration of the concept, they may still provide useful insight into the behavior of conventional jointed FRC overlays, including the importance of avoiding dominant joint behavior.

D.5. References

ACI. 2018. *Guide to Design with Fiber-Reinforced Concrete*. American Concrete Institute, Farmington Hills, MI.

Bordelon, A., and J. Roesler. 2012. Design with Fiber Reinforcement for Thin Concrete Overlays Bonded to Asphalt. *Journal of Transportation Engineering*, Vol. 138, No. 4.

Darter, M. 1977. *Design of Zero-Maintenance Plain Jointed Concrete Pavement, Vol 1 – Development of Design Procedures*. Federal Highway Administration, Washington, DC.

Fick, G., J. Gross, M. Snyder, and T. Cackler. 2021. *Guide to Concrete Overlays*. Fourth Edition. National Concrete Pavement Technology Center, Institute for Transportation, Iowa State University, Ames, IA.

Gross, J., D. King, H. Ceylan, Y. Chen, and P. Taylor. 2019. *Optimizing Joint Spacing for Concrete Overlays with and without Structural Fiber Reinforcement*. National Concrete Pavement Technology Center, Institute for Transportation, Iowa State University, Ames, IA.

Kim, M., A. Bordelon, and N. Lee. 2017. Early-Age Crack Widths of Thin Fiber-Reinforced Concrete Overlays Subjected to Temperature Gradients. *Construction and Building Materials*, Vol. 148, pp 492–503.

King, D., and J. Roesler. 2014. *Structural Performance of Ultra-Thin Whitetopping on Illinois Roadways and Parking Lots*. University of Illinois at Urbana-Champaign, IL.

Mulheron, M., J. Kevern, and T. Rupnow. 2015. Laboratory Fatigue and Toughness Evaluation of Fiber-Reinforced Concrete. *Transportation Research Record*, Vol. 2508, No. 1.

Roesler, J., and D. Wang. 2009. Thermal Stress Analysis in Ultra-Thin Whitetopping Pavement. *Proceedings of the 8th International Conference on the Bearing Capacity of Roads, Railways, and Airfields*, pp. 1079–1090. June 29–July 2, Champaign, IL.

Roesler, J., A. Bordelon, A. Brand, and A. Amirkhanian. 2019. *Fiber-Reinforced Concrete for Pavement Overlays: Technical Overview*. National Concrete Pavement Technology Center, Institute for Transportation, Iowa State University, Ames, IA.

Weiss, J., T. Ley, L. Sutter, D. Harrington, J. Gross, and S. Tritsch. 2016. *Guide to the Prevention and Restoration of Early Joint Deterioration in Concrete Pavements*. National Concrete Pavement Technology Center, Institute for Transportation, Iowa State University, Ames, IA.

2711 South Loop Drive, Suite 4700 | Ames, IA 50010-8664 | Phone: 515-294-5798 | cptechcenter.org